

**UNIVERSITY
OF OSLO**

Steffen M. Brask

**Numerical Study of Langmuir
Probes: Improving Accuracy Using
PIC Simulations**

Thesis submitted for the degree of Philosophiae Doctor

Department of Physics
Faculty of Mathematics and Natural Sciences



2024

© **Steffen M. Brask, 2024**

*Series of dissertations submitted to the
Faculty of Mathematics and Natural Sciences, University of Oslo
No. 2737*

ISSN 1501-7710

All rights reserved. No part of this publication may be
reproduced or transmitted, in any form or by any means, without permission.

Cover: UiO.
Print production: Graphic center, University of Oslo.

To Jie

Preface

This thesis is submitted in partial fulfillment of the requirements for the degree of *Philosophiae Doctor* at the University of Oslo. The research presented here was conducted at the University of Oslo, under the supervision of Professor Wojciech J. Miloch with co-supervisors from Kobe University professor Hideyuki Usui and associate Professor Yohei Miyake. Although formally this work was financially supported by my research position at UiO, this work was in large part supported by the 4DSpace - Strategic Research Initiative, and contracts with ESA 4000127346/19/NL/IA and 4000130688/20/NL/FF/gp. Support was also given by the Norwegian Directorate for Higher Education and Skills, project number: UTF-2016-long-term/10054. Support was also given indirectly from Swarm DISC—Data, Innovation, and Science Cluster, funded through the European Space Agency, through ESA contract 4000109587/13/I-NB.

The thesis is a collection of three papers, presented in chronological order of writing. The common theme to them is improving Langmuir Probe accuracy through means of kinetic Particle-in-Cell simulations. The papers are preceded by three chapters. An introductory chapter that relates them to the field of plasma and space physics and provides background information and motivation for the work. Next is a chapter with background theory that is important for understanding the results. Last is a chapter explaining the main simulation method with a focus on the most relevant parts of the method, and the implementations done as a part of this PhD.

Acknowledgements

First, I would like to thank my main supervisor Professor Wojciech J. Miloch, whose tireless efforts drive the research at the space and plasma physics group at UiO. Wojciech is always available, and always puts in an extraordinary effort beyond what I would expect from any supervisor. Many discussions have led to great insights; in many ways, he is responsible for making much of this work possible. All three supervisors were also my supervisors on my project for my master's degree. We have known each other for many years now, and all of you have been responsible for forming me as a researcher.

Although I am the primary contributor to all three articles, the work would not have been possible without colleagues and research partners. In particular, S. Marholm has been a major contributor to most of the work done in developing the simulation code PINC, in addition to providing insights to many discussions. He is also a co-author of the first two papers. In addition, contributions from F. Di Mare S. Adhikari, A. Spicher T. Takahashi made paper I possible. Paper II was made possible by the contributions of Professor R. Marchand who also

cindly provided the simulation code PTetra to use for this project. In paper III the main idea was my own, however, the quality of this project was improved through discussions with co-authors R. Mishra and G. Holen, in addition to my supervisors. I am grateful for the opportunity to draw from the knowledge of all of my co-authors.

Since this PhD was done in large as an extra to other research responsibilities it would not be possible without the understanding and support of my soon-to-be wife Jie Hou. Many late hours should have taken a toll on our relationship, but you have given me nothing but support.

I would also like to thank my fellow PhD students Florine Enengl, Lisa Buschmann, and Pascal Sado for their support. I am going to miss our Tuesday lunch discussions.

Lastly, I want to thank the rest of the plasma and space physics research group for creating an intellectually engaging environment. It has been a great place to work.

• **Steffen M. Brask**

Oslo, January 2024

Summary

English

A common approach to probing a plasma is with Langmuir probes. Langmuir probes collect electric currents from the surrounding plasma and infer plasma parameters using theoretical considerations usually based on the orbital motion limited (OML) theory. The OML theory uses assumptions that need to be met for it to be accurate. Under certain conditions in the ionosphere, these assumptions are not strictly met, leading to uncertainty in the measurements.

In this thesis, the aim is to improve Langmuir probe measurements using particle-in-cell (PIC) simulations to test the limits of common assumptions in the OML theory, and where possible build models to correct for the errors. In particular, three assumptions are studied: the assumption of collisionless conditions, the assumption of a perfect geometry, and the assumption of an unmagnetized plasma.

The assumption on collisionless conditions is tested by simulating a spherical Langmuir probe in a plasma with typical lower ionospheric plasma parameters. The simulations are run in a range of collision frequencies where it is found that an increase in the electron current is present when the mean free path of the electrons approaches the Debye length. A model that is valid down to 100 kilometers in height is built, and corrections are applied to data gathered on the Investigation of Cusp Irregularities-4 sounding rocket.

The OML theory is based on ideal geometries such as planar, cylindrical, and spherical. In practice, such geometries are not possible, however, they can often be used to a good approximation. A Langmuir probe is mounted to a guard and the guard is mounted to a spacecraft surface or boom. Since the OML theory uses ideal geometries it is assumed that the guard and boom do not impact the current collection significantly. An in-depth evaluation of the limits of the validity of this assumption is done using PIC simulations. It is found that the common guard length of ~ 2 Debye lengths is not sufficient, and at least 6 – 8 Debye lengths should be used for a minimal impact. In addition, it is found that the guard radius should follow the same assumption as the probe radius of being smaller than the Debye length.

Since the ionosphere is inside the Earth's magnetosphere the plasma is not unmagnetized. In regions of the ionosphere where the plasma temperature is low and the Debye length is long, the magnetization of the plasma is stronger. It is therefore studied how magnetization impacts the current collection of a spherical Langmuir probe using PIC simulations. It is found that magnetization can impact the currents to a great degree, lowering them by as much as 90%. A model is built to correct for the magnetization effect for a wide range of parameters,

making it applicable to many of the conditions found in the ionosphere.

Norwegian

En vanlig tilnærming for å undersøke et plasma er med Langmuir prober. Langmuir prober samler elektriske strømmer fra det omkringliggende plasmaet og beregner plasmaparametere ved hjelp av teoretiske betraktninger, vanligvis basert på teorien kalt "orbital motion limited" (OML). OML teorien bruker antakelser som må oppfylles for at den skal være nøyaktig. Under visse forhold i ionosfæren oppfylles ikke disse antakelsene strengt, noe som fører til usikkerhet i målingene.

I denne avhandlingen er målet å forbedre målingene med Langmuir prober ved å bruke såkalte "Particle-in-cell" (PIC) simuleringer for å teste grensene for vanlige antakelser i OML teorien, og der det er mulig, bygge modeller for å korrigere feilene. Spesielt studeres tre antakelser: antakelsen om kollisjonsfrie forhold, antakelsen om en perfekt geometri, og antakelsen om et umagnetisert plasma.

Antakelsen om kollisjonsfrie forhold testes ved å simulere en sfærisk Langmuir probe i et plasma med typiske plasma parametere for den lavere ionosfæren. Simuleringene kjøres i et spekter av kollisjonsfrekvenser der det viser seg at det er en økning i elektronstrømmen når middelfrivi for elektronene nærmer seg Debye lengden. En modell som er gyldig ned til 100 kilometer i høyde bygges, og korreksjoner påføres data samlet inn av Investigation of Cusp Irregularities-4 sonderaketten.

OML teorien er basert på ideelle geometrier som planar, sylindrisk og sfærisk. I praksis er slike geometrier ikke alltid mulige, men de kan ofte brukes som en god tilnærming. En Langmuir probe er montert på en beskytter, og beskytteren er montert på en overflate eller stag på et romfartøy. Siden OML bruker ideelle geometrier, antas det at beskytteren og staget ikke påvirker strømsamlingen betydelig. En grundig evaluering av gyldighetsgrensene for denne antakelsen gjøres ved hjelp av PIC simuleringer. Det viser seg at den vanlige beskytterlengden på ~ 2 Debye lengder ikke er tilstrekkelig, og minst 6 – 8 Debye lengder bør brukes for minimal påvirkning. I tillegg viser det seg at beskytterens radius bør følge den samme antakelsen som probens radius om å være mindre enn Debye lengden.

Siden ionosfæren er innenfor jordens magnetosfære, er plasmaet ikke umagnetisert. I områder av ionosfæren der plasmaets temperatur er lav og Debye lengden er lang, er magnetiseringen av plasmaet sterkere. Det studeres derfor hvordan magnetisering påvirker strømsamlingen til en sfærisk Langmuir probe ved hjelp av PIC simuleringer. Det viser seg at magnetisering kan påvirke strømmene i stor grad, og redusere dem med så mye som 90%. En modell bygges for å korrigere for magnetiseringseffekten for et bredt spekter av parametere, noe som gjør den anvendelig for mange forhold som finnes i ionosfæren.

List of Papers

Paper I

S. M. Brask, S. Marholm, F. Di Mare, S. Adhikari, A. Spicher, T. Takahashi, W. J. Miloch “Electron–neutral collisions effects on Langmuir probe in the lower E-region ionosphere”. In: *Physics of Plasmas*. Vol. 29, no. 3 (2022), DOI: 10.1063/5.0079761.

Paper II

S. M. Brask, S. Marholm, W.J. Miloch, R. Marchand “Effects of Guard and Boom on Needle Langmuir Probes Studied with Particle in Cell Simulations”. Accepted for publication in *Journal of Plasma Physics*, 24-Nov-2023

Paper III

S. M. Brask, R. Mishra, G. Holen, Y. Miyake, H. Usui, W.J. Miloch “Spherical Langmuir probes in magnetized plasma. A model based on Particle-in-Cell simulations”. Accepted for publication in *Physics of Plasmas*, 16-Jan-2024.

Contents

Preface	iii
Summary	v
List of Papers	vii
Contents	ix
List of Figures	xi
1 Introduction	1
1.1 Objectives and Scope	3
2 Background	5
2.1 Single Particle Motion and Particle Description of Plasma	6
2.2 Kinetic Description of Plasma	7
2.3 Fluid Description of Plasma	8
2.4 Objects in Plasma	9
2.5 Current Collection	9
2.6 OML Theory	10
2.7 Langmuir Probes and Design Considerations	11
3 PINC-simulator	15
3.1 Particle-in-Cell method	15
3.2 Stability Criteria	20
3.3 Object-Plasma interactions	21
3.4 Parallelization in PINC	23
3.5 Open boundaries	24
3.6 Charged-neutral collisions	25
3.7 Testing and Verification	27
3.8 Status of PINC	28
4 Summary of Papers	31
4.1 Paper I (Electron-neutral collisions effects on Langmuir probe in the lower E-region ionosphere)	31
4.2 Paper II (Effects of Guard and Boom on Needle Langmuir Probes Studied with Particle in Cell Simulations)	32
4.3 Paper III (Spherical Langmuir probes in magnetized plasma. A model based on Particle-in-Cell simulations)	33

Contents

5	Discussion	35
5.1	Future work	36
	Bibliography	39
	Papers	44
I	Electron–neutral collisions effects on Langmuir probe in the lower E-region ionosphere	45
II	Effects of Guard and Boom on Needle Langmuir Probes Studied with Particle in Cell Simulations	59
III	Spherical Langmuir probes in magnetized plasma. A model based on Particle-in-Cell simulations	77

List of Figures

1.1	Aurora australis as seen from the ISS	1
1.2	Plasma zoo	2
1.3	Illustration of NASA-ESA Cassini spacecraft close to Saturn. Credits: NASA.	3
2.1	Illustration of a Debye sphere	5
2.2	I-V curve	12
3.1	PIC cycle flow chart.	16
3.2	Schematic diagram of a superparticle moving in the grid.	17
3.3	Diagram of the parallelization employed in PINC	23
3.4	null-collision schematic.	26

Chapter 1

Introduction

It is often stated by plasma physicists that 99% of the observable universe (i.e., visible matter) is in a plasma state [3, 36]. This statement is therefore one of the most popular and efficient ways for plasma physicists to create "enemies" in other fields of physics. The statement is of course true, however, it is misleading since it is also a question of the scales involved. In a galaxy, all the stars are in a plasma state, and the dynamics of the star's core, layers, and corona are best described as a plasma. The macroscopic picture of the galaxy on the other hand is best described through gravitational effects. Astrophysics and space physics is therefore not purely plasma physics, although the fact remains that matter is mainly in a plasma state, and the field of space physics is in large part plasma physics.

Plasma is sometimes called the fourth state of matter [9, 13]. Consider a solid matter. If we continuously add heat to the matter it will at some point transition into a liquid. Further increasing the temperature turns the liquid into a gas. Sufficiently heating the gas will lead to ionization, where the electron bonds to the nucleus in the atoms are broken such that the gas consists of free charges, and the gas is then in a plasma state. This is a simplification, and there is not a point at which all the particles get ionized. In a gas, there is always a part of the gas that is ionized, and the transition to a plasma happens when the gas is sufficiently ionized such that the collective behavior is dominated by electromagnetic effects.

At the surface of the Earth, natural occurrences of plasmas are seldom. This is because the gas temperature is low and the density is high, such that ionized particles quickly recombine back to neutral particles [9]. However, natural occurrences of plasmas exist in the form of discharges such as lightning or in the upper atmosphere, where in the polar regions charged particles can lead to aurora borealis or aurora australis, shown in figure 1.1. Plasma physics is also applied in many man-made devices, such as light tubes, neon lights, and the

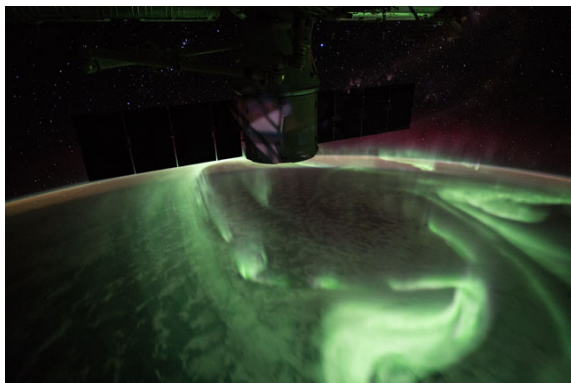


Figure 1.1: Aurora australis as seen from the ISS on 19.08.2017 19:20:05 GMT. Credits: NASA.

1. Introduction

pixels of a plasma TV. Plasma can even be made at home by placing two grapes under an upside-down glass in a microwave oven and turning it on.

It is common to differentiate plasma regimes by their typical temperatures and densities. Figure 1.2 shows an overview of such regimes. In classical plasmas, we often differentiate between cold plasma where slow-moving particles interact seldom with each other, examples of such plasmas include the ionosphere or the solar wind. These are in contrast to hot plasma where more frequent interactions make, in addition to the electromagnetic forces, conventional pressure forces important, for example in the solar core.

It is also common to differentiate between relativistic and non-relativistic plasma. In relativistic plasma, the particles' movements need to take into account relativistic effects, and in the highest density quantum plasma where quantum effects are important due to short distances on the quantum scale between particles.

Since naturally occurring plasma is sparse, to study plasma we are generally restricted to laboratory experiments, direct measurements via sounding rockets or spacecraft, indirect measurements with ground-based instruments, or computational simulations. On Earth, plasma for space physics can also be studied experimentally in plasma chambers [27]. There is also interest in plasma fusion with large experiments such as the ITER tokamak and the Wendelstein 7-X stellarator [12, 38]. The promise of plasma fusion is abundant clean and cheap energy, and it is therefore easy to see the appeal. Indirect measurements of space plasma are done with ground-based radars such as ionosondes, SuperDARN, and EISCAT, as well as with optical and other instruments [33, 46]. In space, measurements are done mostly through in-situ observations where instruments are flown on sub-orbital and orbital spacecraft, and also on spacecraft flown to other celestial bodies [4, 39, 45].

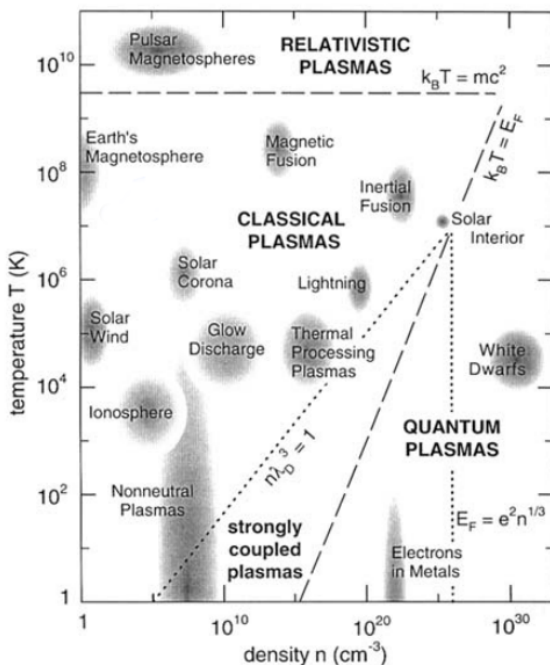


Figure 1.2: Examples of naturally occurring and artificially made plasmas shown as a function of their temperature T and density n (per cubic cm). Figure adapted from [10].

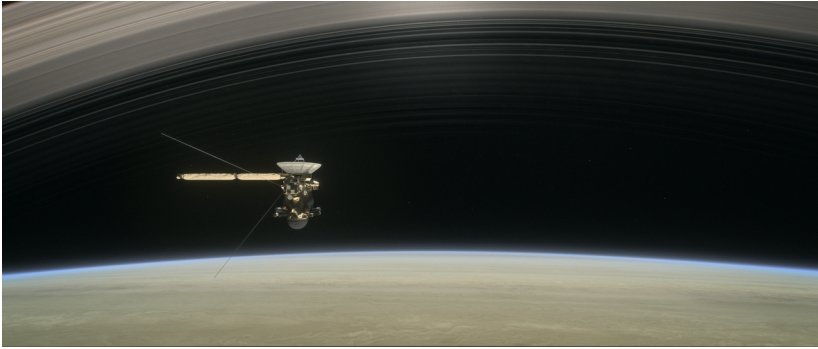


Figure 1.3: Illustration of NASA-ESA Cassini spacecraft close to Saturn. Credits: NASA.

In this thesis, we are mainly interested in the ionospheric plasmas which are space plasmas that are closest to Earth and therefore the ones we study most frequently with probes. The results in this thesis have applications also for magnetospheric plasma which we find in Earth's magnetosphere, but also in the magnetosphere of other celestial bodies such as Saturn that was investigated by the Cassini spacecraft, see figure 1.3.

One standard way to probe a plasma is with a Langmuir probe. Langmuir probes are widely applied in space physics research, where most space missions that have instruments for plasma measurements include a Langmuir probe. A Langmuir probe is in simple terms a conductive surface with a known geometry. Currents to conducting surfaces immersed in plasma were described by [31]. From these currents plasma parameters such as density and temperature can be inferred, however, the theory on which the parameters are calculated is based on an ideal case where several assumptions are made.

1.1 Objectives and Scope

The main goal of this thesis is to study the real-environment impact on some of the assumptions made in the Orbital-Motion-Limited (OML) theory for Langmuir probes. We wish to increase the accuracy and reliability of Langmuir probes by minimizing the error in the measurements that stem from specific assumptions. The study is done mainly through plasma-probe simulations, designed to measure the difference in the currents from an ideal case to a more realistic case. We will also focus on practical aspects, such that the results can be applied to ongoing and upcoming space experiments.

The common assumptions we aim to test are as follows:

- In the lower E-region ionosphere the assumption of a collisionless plasma breaks down. This region is of growing interest since it is shown to be of importance for scintillation of trans ionospheric radio signals such as from

Global Navigation Satellite Systems (GPS, Galileo, etc.) [24]. However, although particle collisions are often stated as a possible culprit of errors in the measurements, a study quantifying the errors has not been done. We therefore wish to measure the impact of collisions between charged and neutral particles in the context of the E-region ionosphere.

- Data analyses from Langmuir probes are based on theories that consider ideal geometries where these geometrical objects are free-floating. In reality, such ideal geometries are not possible since the probe needs to be mounted to a surface, and practical considerations play a role. Since an ideal probe is practically impossible the violation of this assumption is often neglected, and arguments are made on a general basis. We will study the applicability of this assumption in detail, and give an accurate limit of the geometric assumptions.
- One well-known problem with the Langmuir probe theories is that they assume non-magnetized plasma, but they are frequently used for measurements in magnetized plasma. Theories including magnetized effects have been developed [22], however, they are known to be inaccurate. It is therefore often assumed that magnetic effects are negligible, and theory for a non-magnetized plasma is used instead. We will therefore employ empirical modeling based on simulations such that the effects of magnetization can be taken into account and corrected for both in previous, present, and upcoming experiments.

In addition to the aforementioned problems, in this thesis, there is a goal of further developing the particle-in-cell simulation code PINC. At the start of this PhD, PINC was a functioning code capable of large-scale multi-species plasma simulations. However, the appropriate boundary conditions and plasma-object calculations were not finalized. Therefore PINC code needs to be extended, and tested for the new additions.

All the simulations included in the papers (except for verification/comparison) for this thesis were performed by the author of this thesis. The simulation code was initially a concept developed by Dr. Sigvald Marholm, after which it was handed over to the author. The code was at various times co-developed with several developers (Dr. Jan Deca, Gullik Killie, Vigdis Holta, Steffen Brask, Trym Nielsen) [8, 17, 20, 25] Over the course of the project, for the papers included in this thesis, PINC was run on several computer clusters (Abel, Saga, Fram) on 16-256 CPU's, where the total amount of time used is in the range of 500.000-1.000.000 CPU hours.

Chapter 2

Background

A plasma is a collection of charged particles where all the particles interact with each other through electromagnetic forces. Particles of opposite charge will attract each other and particles of the same charge will be pushed apart. When there are many particles, a collection of the same charge particles will attract opposite charge particles in the vicinity 2.1. These attracted particles will therefore form a "cloud" of opposite charge around the collection of particles. This cloud is called the Debye sphere, with its radius being the characteristic plasma length, or Debye length λ_D [9, 36]:

$$\lambda_{Ds} = \sqrt{\frac{\epsilon_0 k T_s}{q_s^2 n_s}}, \quad (2.1)$$

where s denotes a particle species. k, T_s are respectively the Boltzmann constant and temperature, q_s is the particle charge, n_s is the number density of particles, and ϵ_0 is the vacuum permittivity.

The attracted particles will shield the forces from particles outside the Debye sphere, such that the collection of charges at the center effectively only feels the forces from the contributions inside the Debye sphere.

On scales similar to the Debye length there will be areas of positive and negative charge, however, on scales much larger than the Debye length the plasma can be considered charge-neutral. This condition is commonly referred to as quasi-neutrality. The positive and negatively charged areas will pull and push particles in adjacent areas, which leads to a natural frequency of oscillation called the plasma frequency ω_{ps} :

$$\omega_{ps} = \sqrt{\frac{q_s^2 n_s}{\epsilon_0 m_s}} \quad (2.2)$$

where m_s is the species particle mass. There are several other natural, or resonant, frequencies in a plasma, depending on the conditions.

For a gas to be considered a plasma it needs to be sufficiently ionized, such that the particles' mean free path is long with respect to the Debye length in space

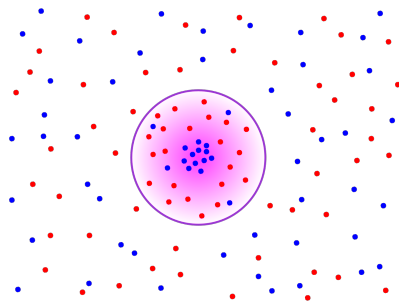


Figure 2.1: Illustration of a Debye sphere. Two species (red and blue) with opposite charge signs form fluctuations on the scale of the Debye length. On larger scales, the plasma is charge-neutral.

2. Background

and the collision frequency is low as compared to the plasma frequency in the temporal domain. One way to understand this is that a charged particle needs to interact with the fields from the bulk for several plasma periods and travel several Debye lengths before colliding with a neutral particle. This is also the case for the Coloumb scattering, which can be considered a collision between two charged particles. A more precise way to describe this criterion is with the plasma parameter Λ :

$$\Lambda = \frac{4}{3}\pi n_s \lambda_{D_s}^3. \quad (2.3)$$

The plasma criteria are then $\Lambda \gg 1$ [9]. Thus, the number of charged particles within a Debye sphere must be large.

2.1 Single Particle Motion and Particle Description of Plasma

In the microscopic description, plasma dynamics can be described through the motion of a collection of single particles. For a single non-relativistic particle, the equations of motion are given by [6]:

$$\frac{d\vec{x}_p}{dt} = \vec{v}_p, \quad m_p \frac{d\vec{v}_p}{dt} = \vec{F}_p, \quad (2.4)$$

where \vec{x}_p , \vec{v}_p is the position and velocity of particle p and m_p is its mass. The force F_p acting on the particle is given by the Lorentz force:

$$\vec{F}_p = q_p(\vec{E}_p + \vec{v}_p \times \vec{B}_p), \quad (2.5)$$

where q_p is the particle's charge. For the Lorentz force the electric and magnetic fields \vec{E}_p and \vec{B}_p are evaluated at the particle position. The evolution of the electric and magnetic field is governed by Maxwell's equations [3, 9]

$$\text{Gauss' law:} \quad \nabla \cdot \vec{E} = \frac{\rho}{\epsilon_0} \quad (2.6)$$

$$\text{Gauss' law for magnetism:} \quad \nabla \cdot \vec{B} = 0 \quad (2.7)$$

$$\text{Maxwell - Faraday law:} \quad \nabla \times \vec{E} = -\frac{\partial \vec{B}}{\partial t} \quad (2.8)$$

$$\text{Ampere's law:} \quad \nabla \times \vec{B} = \mu_0(\vec{J} + \epsilon_0 \frac{\partial \vec{E}}{\partial t}) \quad (2.9)$$

In Gauss' Law, equation 2.6, ρ is the electric charge density, and ϵ_0 is the vacuum permittivity. In Ampere's law, equation 2.9, μ_0 is the vacuum magnetic permeability, and \vec{J} is the surface electric current density. ρ and \vec{J} act as source terms for the electric and magnetic fields in equations 2.6 and 2.9, and the fields are coupled through equation 2.8.

The source terms ρ and \vec{J} are generated by the particles, and can therefore be written as sums over the particle ensemble [3]

$$\rho = \sum_p q_p \delta(\vec{x} - \vec{x}_p), \quad \vec{J} = \sum_p q_p \vec{v}_p \delta(\vec{x} - \vec{x}_p) \quad (2.10)$$

where δ is the Dirac-delta function. Equations 2.10 close the set of Maxwell's equations and together with equations 2.4 and 2.5 give a complete description of the plasma. However, the set of equations is highly nonlinear since the source terms, equations 2.10, are calculated from the particle ensemble, which eventually dictates the particles' movement. A solution is also quite involved in realistic cases due to many particles involved in the system.

A common simplification made in many space physics applications is that of the electrostatic plasma approximation [16]. For slowly varying magnetic fields, the right-hand side of equation 2.8 can be neglected, such that $\nabla \times \vec{E} = 0$. Using Helmholtz theorem, \vec{E} can thus be described in terms of an electric potential ϕ

$$\vec{E} = -\nabla\phi. \quad (2.11)$$

Inserting equation 2.11 into Gauss' law 2.6 reveals Poissons' equation for electric potentials

$$\nabla^2\phi = -\frac{\rho}{\epsilon_0}. \quad (2.12)$$

In the electrostatic approximation equation 2.11 and 2.12 can be used instead of the full set of Maxwell's equations. The implications of doing so are that physical properties like energy and momentum can not propagate through the magnetic field, and any physical process where such propagation is important will be neglected. A static magnetic field and the effects of a static magnetic field can still be included in the formalism, as long as the assumption $\frac{\partial \vec{B}}{\partial t} = 0$ holds.

2.2 Kinetic Description of Plasma

The kinetic description of a plasma is that of the evolution of the $6D$ phase space particle distribution function. It is generally accepted for space plasmas that the evolution is governed by the collisionless Boltzmann equation, called the Vlasov equation [44]:

$$\left(\frac{\partial}{\partial t} + \vec{v} \cdot \nabla + \frac{q_s}{m_s} (\vec{E} + \vec{v} \times \vec{B}) \cdot \frac{\partial}{\partial \vec{v}} \right) f_s(\vec{x}, \vec{v}, t) = 0 \quad (2.13)$$

where $f_s(\vec{x}, \vec{v}, t)$ is a distribution function for an ensemble of particles. $f_s(\vec{x}, \vec{v}, t)$ can be described by a sum of each particle's probability distribution function (Liouville's theorem).

From the distribution, macroscopic quantities for the bulk density and bulk velocity can be derived by taking the zeroth and first-order moments of f_s :

$$n_s = \int f_s(\vec{x}, \vec{v}, t) d\vec{v} \quad (2.14)$$

2. Background

$$n_s \vec{v} = \int \vec{v} f_s(\vec{x}, \vec{v}, t) d\vec{v} \quad (2.15)$$

where n_s is the particle number density for species s . In combination with the Maxwell equations, and using a macroscopic description of charge density and current density

$$\rho = \sum_s q_s n_s \quad (2.16)$$

$$\vec{J} = \sum_s q_s n_s \vec{v}_d \quad (2.17)$$

this closes the Vlasov-Maxwell set of equations.

When the particles in a plasma exchange energy and momentum often the particles' velocity distribution will be Maxwellian. In three dimensions the Maxwellian distribution is [9]

$$f_{0,s}(\vec{v}, t) = \left(\frac{1}{\sqrt{2\pi} v_{th,s}} \right)^3 \exp\left(-\frac{1}{2} \frac{\|\vec{v} - \vec{v}_d\|^2}{v_{th,s}^2}\right), \quad (2.18)$$

where v_d is the bulk plasma drift velocity. The thermal speed $v_{th,s}$ is the root-mean-squared value of the particles' velocities, which is also the standard deviation of the distribution:

$$v_{th,s} = \sqrt{\frac{kT_s}{m_s}}. \quad (2.19)$$

Here the plasma temperature is T_s .

2.3 Fluid Description of Plasma

It is common to model a plasma using a fluid model. Several abbreviations of such models are commonly employed, however, loosely speaking they use the zeroth and first moments of the Boltzmann equation to get the conservation of continuity and momentum (Navier-Stokes) equations [3]:

$$\frac{\partial n_s}{\partial t} + \nabla \cdot (n_s \vec{v}_s \vec{v}_s) = 0 \quad (2.20)$$

$$\frac{\partial n_s \vec{v}_s}{\partial t} + \nabla \cdot (n_s \vec{v}_s \vec{v}_s) = n_s \frac{q_s}{m_s} (\vec{E} + \vec{v}_s \times \vec{B}) - \frac{1}{m_s} \nabla p_s \quad (2.21)$$

where p_s is the fluid pressure, which was assumed to be isotropic.

Along with these two conservation equations, one or more equations to close the system are needed. It is quite common to use an equation of state for the pressure, which relies on assuming the particle distribution to be Maxwellian. In addition, another assumption commonly made for the electromagnetic force is the electrostatic assumption, such that the electromagnetic part of the equations can be closed using Poisson's equation, equation 2.12, instead of the full set of Maxwell's equations.

2.4 Objects in Plasma

When an object is immersed in a plasma it will collect charged particles. The charged particle collection can be determined by a current balance. The process of particle collection will differ for conducting and non-conducting surfaces, where we are mainly interested in conducting surfaces since both spacecraft and probes usually have conducting surfaces. The current balance equations are valid for the whole spacecraft body if it is conducting, and only valid in the limit of a point for a non-conducting surface which complicates the charging dynamics [14].

Charging of an object can also be complicated by involving many charging sources, such as thermal ions and electrons, photo-electrons, secondary electrons, high-energy particles etc. We will mainly focus in this thesis on a two-species plasma with a single electron and ion species. For an object at the plasma potential V_p , i.e., when an object has no net charge, the current flux to the object will be determined by the species thermal velocity [14]. Since ions are much heavier than electrons, more electrons will be collected over time leading to an overall negative charge. This charge will set up an electric potential on the object called the floating potential, at which the net current to the object is zero. Thus, the value of the potential on the object with respect to plasma is determined by the current balance.

2.5 Current Collection

At floating potential, the current balance equation can be formulated as a sum of all possible currents to a conducting surface in a plasma as

$$\frac{dQ}{dt} = \sum_s I_s(V) = 0, \quad (2.22)$$

where Q is the total charge, V is the potential of the object, and s denotes the species.

For an object that is large with respect to the Debye length, the sheath will be small with respect to the object size. This is called the thin sheath approximation, and the object charging can be described by the sheath-limited theory, where the sheath size can be neglected. This is typically done for spacecraft, and for calculating the floating potential of spacecraft. The simplest calculation of floating potential is that of a non-drifting collisionless, non-magnetized Maxwellian plasma where the current balance 2.22 is a sum of thermal currents for each species[47]. We will consider in this thesis a more realistic and slightly more complicated scenario by including a super-sonic drift. A commonly used derivation for the floating potential of a spacecraft is given by [1].

A spacecraft in orbit is typically moving at supersonic speeds. At such speeds, the ions can be considered stationary in their frame of reference, however, for the electrons the spacecraft can be considered stationary since they are moving

2. Background

orders of magnitude faster. Therefore all of the surface is accessible to the electrons. However, for the ions only the surface area facing the ram direction is accessible. This can be formulated in terms of current flux as

$$J_i = qn_i v_{sc} \quad (2.23)$$

where v_{sc} is the spacecraft speed. Particle attraction and repulsion have been neglected here due to the slow ion thermal movement such that the spacecraft potential is ignored. This can not be done for the electrons where the current flux, assuming a spherical geometry is

$$J_e = q_e n_e \sqrt{\frac{2kT_e}{\pi m_e}} \exp\left(\frac{qV}{kT_e}\right) \quad (2.24)$$

where V is the spacecraft potential. For other geometries than spherical, the constant stemming from integration will be different. Inserting these fluxes into equation 2.22, and using $I = AJ$ for a surface area A we get the floating potential, ϕ_{sp} :

$$\phi_{sp} = -\frac{kT_e}{q} \ln \frac{A_e}{A_i} \left(\frac{kT_e}{2\pi m_e v_{sc}^2}\right)^{\frac{1}{2}} \quad (2.25)$$

For spherical geometry the ratio of accessible surfaces is $A_e/A_i = 4$, and using $T_e = 1500K$, we get $\phi_{sp} = -0.458V$. Typically, it is seldom that spacecraft in low Earth orbit experience potential differences of more than a few volts negative [1].

2.6 OML Theory

For a current collector with a thick sheath in a collisionless non-magnetized Maxwellian plasma, we can use the Orbital-Motion-Limited (OML) theory to link current to voltage. In the OML theory current is calculated by considering particles far away from the probe, having energies related to their thermal motion. It is determined by the conservation of energy, and conservation of angular momentum whether such a particle approaching the probe on a ballistic trajectory will be collected, and contribute to the current. It is also assumed that the mean free paths of particles are much longer than the probe size and thus the Debye length, such that the effects of collisions are negligible. In addition, it is assumed that forces from the probe dominate, such that long-range forces from other particles are negligible.

The probe currents are divided into collected species current and repelled species current, where a collected species has $q_s V < 0$ with V being the probe bias potential. Collected species current expressions for simple geometries are given by integrating over the part of the species distribution accessible to the probe [31]:

$$\text{plane: } I_s(\eta_s) = I_{th,s} \quad (2.26)$$

$$\text{cylinder: } I_s(\eta_s) = I_{th,s} \left(\frac{2}{\sqrt{\pi}} \sqrt{\eta_s} + \exp(\eta_s) \operatorname{erfc}(\sqrt{\eta_s}) \right) \quad (2.27)$$

$$\approx I_{th,s} \frac{2}{\sqrt{\pi}} \sqrt{1 + \eta_s} \quad (2.28)$$

$$\text{sphere: } I_s(\eta_s) = I_{th,s}(1 + \eta_s) \quad (2.29)$$

$$(2.30)$$

where $I_{th,s}$ is the thermal current corresponding to the situation where the probe had zero bias. The thermal current is given by the particle thermal flux and the surface area S as $I_{th,s} = n_s q_s S \sqrt{\frac{kT_s}{2\pi m_s}}$. To simplify the notation we used dimensionless potential $\eta_s = -q_s V / kT_s$. The approximation given in equation 2.28 is generally accepted to be valid for $\eta > 2$.

For a repelled species $q_s V > 0$ the current to the probe is

$$I_s(\eta_s) = I_{th,s} \exp(\eta_s) \quad (2.31)$$

and is independent of probe shape, but proportional to the surface area. Equations 2.26 to 2.29 were summarized in a single equation by [21]

$$I_s(\eta) = I_{th,s} K (1 + \eta)^\beta \quad (2.32)$$

where K and β are geometric parameters determined by equations 2.26 to 2.29. For a cylinder $K = 2/\sqrt{\pi}$ and $\beta = 0.5$, for a sphere $K = 1$ and $\beta = 1$, and for a plane $K = 1$ and $\beta = 0$.

2.7 Langmuir Probes and Design Considerations

Langmuir probes is a collective term for probes based on current collection theories for conductors in plasmas. Most designs are based on the OML theory and use cylindrical or spherical geometries. It is also possible to use a probe that is large with respect to the Debye length and assume it then behaves as a plane, using equation 2.26 for the currents. This is the same as a thin sheath or sheath-limited approximation. However, of most interest to this thesis are the cylindrical and spherical OML-based probes.

Plasma parameters can be calculated based on a probe I-V characteristics. A typical I-V curve for both cylindrical and spherical probes is shown in figure 2.2. In the figure, the probe bias voltage is on the x-axis, and the probe current is on the y-axis. The current is the sum of currents for both electrons and ions. The I-V curve is split into regions of current collection, according to what current is dominating. In the Ion saturation region, the potential is negative enough that most electrons are repelled, and the ion current dominates. The current can therefore to a good approximation be calculated as an ion current given by equation 2.28 or 2.29 with $s = i$. On the opposite end is the Electron saturation region where the probe bias is positive enough that most ions are repelled and corresponding equations can be used for an electron current with $s = e$. The region in between is called the electron retardation region. Since the ion current

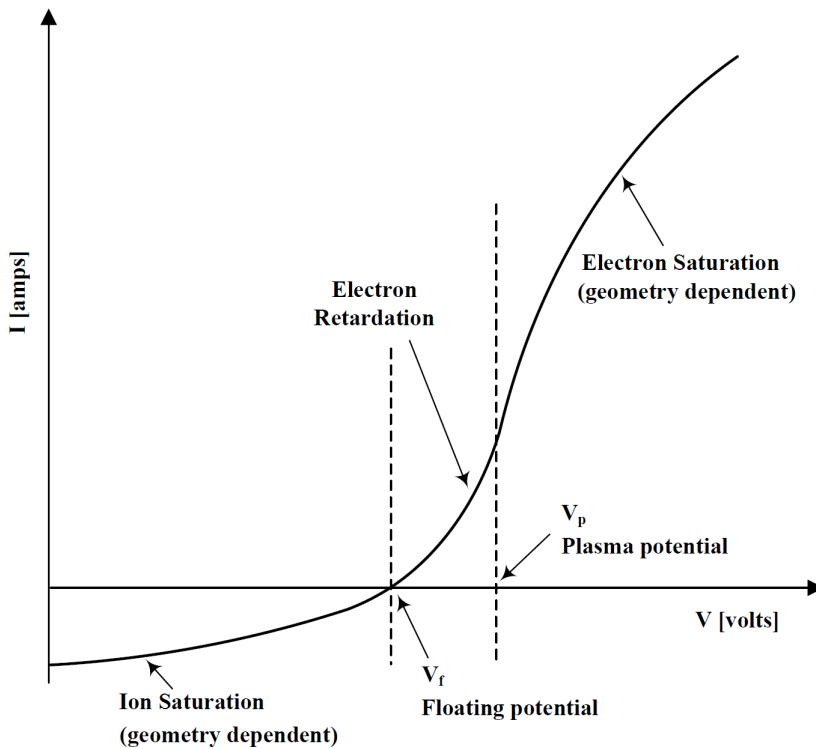


Figure 2.2: typical I-V curve for Langmuir probes. Figure taken from http://tid.uio.no/plasma/norsat/mnlp_instrument.html

is typically much smaller than the electron current due to the slow ion motion, this region can be approximated as a repelled electron current. The current can then be calculated with equation 2.31 where $s = e$. The ion saturation and electron regions are separated by the floating potential V_f , which is the point where all currents sum to zero and also determines the potential of the probe if it is free-floating and un-biased. The plasma potential V_p determines the point between the electron retardation and saturation regions.

Taking the logarithm of equation 2.31 temperature can be expressed as

$$T_e = \frac{q_e V}{k S} \tag{2.33}$$

where S is the slope of the curve in the electron retardation region. Density can be expressed by setting $V = V_p = 0$ in equation 2.31 to get

$$N_e = \frac{I_e}{q_e A} \sqrt{\frac{m_e}{2kT_e}}, \tag{2.34}$$

where A is the probe surface area. Since Langmuir probes are grounded to a spacecraft that has a floating potential, the point of V_f is not readily available, and the slope is therefore also challenging to determine. A common way to solve this problem is by operating the probe in a swept bias mode. Sampling is done in a large range of probe potentials from which the plasma potential can be determined along with the slope by graphical methods [2]. However, since a sweep typically takes seconds to complete, the spacecraft typically moves kilometers within one sweep. A solution to this problem is to use multiple probes like the rapid m-NLP system [4, 15, 19]. In equation 2.32 the probe potential is a sum of the potential V_b given with respect to spacecraft and the spacecraft floating potential $V = V_b + V_f$, where the floating potential is unknown. To get an expression for the density that is independent of V_f we can take the difference of two cylindrical probes at different potentials to get [4]

$$N_e = \frac{1}{CA} \sqrt{\frac{\Delta I^2}{\Delta V}}, \quad (2.35)$$

where $\Delta I^2 = I_1^2 + I_2^2$ for the two probes 1 and 2. ΔV is the difference in probe bias potentials.

The accuracy of any of the density and temperature measurements is dependent on the accuracy of the current measurements, which is the main focus of this thesis. Note also that for some of the calculations, e.g., equation 2.35 we have a squared current, I^2 . In such cases, otherwise insignificant errors will also get squared and may become significant.

In deriving equations 2.33-2.35 the underlying OML theory with its assumptions dictates the accuracy. Whenever one of these assumptions is sufficiently violated this therefore leads to non-trivial effects in the currents. It is important to understand how these effects materialize and may impact the different methods at different scales. For example, if two probes at different potentials have different impacts leading to different errors in the currents this may give a significant error in equation 2.35. However, even with a higher or lower current collection value, if the slope is the same, equation 2.33 may still be accurate.

Chapter 3

PINC-simulator

3.1 Particle-in-Cell method

There are two main methods of particle simulations for plasma. The most basic are the particle-particle type methods, where each particle contributes to each other particles' force term through the Lorentz force 2.5. These contributions are through the field quantities \vec{E} and \vec{B} , thus the fields at the position of a particle are determined by the sum of field contributions from all other particles. The scalability in particle-particle simulations is their main draw-back, where the number of computational operations and their complexity scale as $O(n_p) \propto n_p^2$ [16] with n_p being the number of simulated particles. For an increasing amount of particles, this scalability quickly hits limits on computation, and simulating large systems with many particles is thus not practical. Another type of particle simulations is called particle-mesh (PM) methods, where the most common particle-mesh method is the Particle-in-Cell (PIC) method. In the PIC method the fields \vec{E} and \vec{B} are defined on a grid, also called a mesh, at discrete points in the domain. The grid acts as an intermediary between the particles, where each particle's contribution to the fields only needs to be calculated on the grid once, and the field quantities are then solved separately. Therefore well optimized PIC simulators can achieve a complexity of $O(n_p, n_g) \simeq n_g \log(n_g) + n_p$ [16] or $O(n_p, n_g) \simeq n_g + n_p$ using multigrid solvers [41] and are thus capable of simulating much larger systems.

3.1.1 PIC Main Cycle

The main PIC cycle is illustrated in figure 3.1. The operations in the PIC cycle can be split into four plus two optional operations making six in total. The four standard operations are as follows: The integration of equations of motion that move the particles based on the forces F_p acting on each particle. Each particle's microscopic properties position and velocity, x_p, \vec{v}_p , are then interpolated to the grid to construct particle-related macroscopic quantities: charge density and current density ρ_g, \vec{J}_g . Next, these macroscopic quantities are used to solve for the electric and magnetic fields \vec{E}, \vec{B} . The last step is to interpolate the field quantities from the grid back to the particle positions where the forces on each particle are defined by the Lorentz force equation 2.5. The standard elements of the PIC main cycle with closed boundaries form a self-consistent system where either momentum or energy is conserved [6, 43].

In addition, it is common to initialize the system with a Maxwellian distribution of the particles and update the velocities of the particles by half a step in time to start a leapfrog scheme before entering the main loop. To

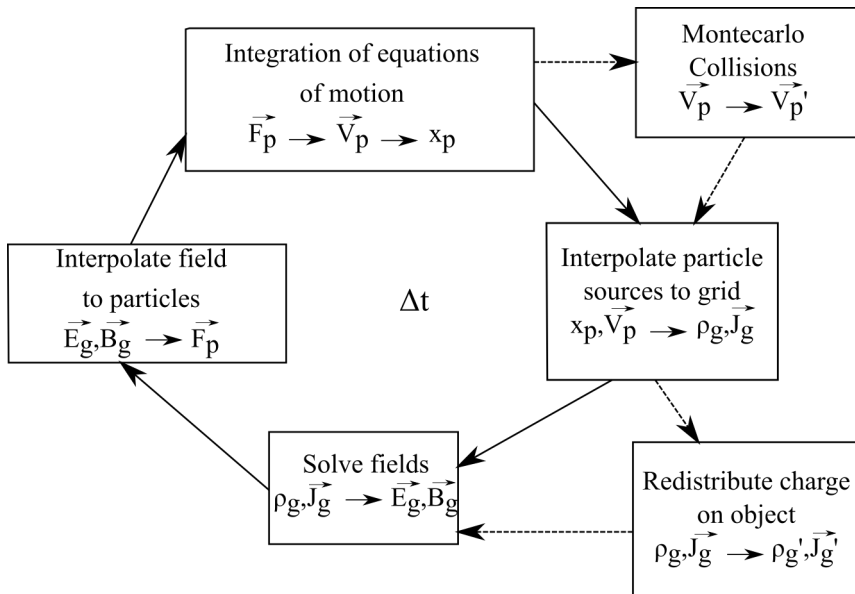


Figure 3.1: PIC cycle flow chart. The chart shows one iteration of the standard PIC cycle with the optional inclusion of Monte-Carlo collisions and plasma-object interaction modules.

make sure that potential energy is not artificially added to the system and that particles are not correlated which could trigger collective phenomena, the initial distribution of particles in space should be randomized within a Debye sphere such that random fluctuations in charge density are of the order of a Debye length or shorter.

The optional operation of Monte-Carlo collisions (MCC) are usually statistical considerations of collisions between charged and neutral particles [43]. They can also include statistical considerations between collisions of charged particles. The collisions change the particles' velocity vectors in direction and magnitude, which also changes the energy of the system according to the statistics. The last additional step that can be included is that of object-plasma interactions. If an object's surface is defined, particles that move through the surface of the object are collected and redistributed on the surface, or throughout the object if the surface has resistance [16]. Several objects can be defined and circuits deciding current flow between them are possible.

3.1.2 Common algorithms

In the new PIC code Particle-IN-Cell (PINC) we use an electrostatic solver for the electric field. For electrostatic solutions, it is common to use a centered grid, where all the field quantities are defined on the same points in space, called nodes or vertices. For electromagnetic field solutions, it is common to use the

Yee lattice, where the electric and magnetic field nodes are offset by a half spatial step [43].

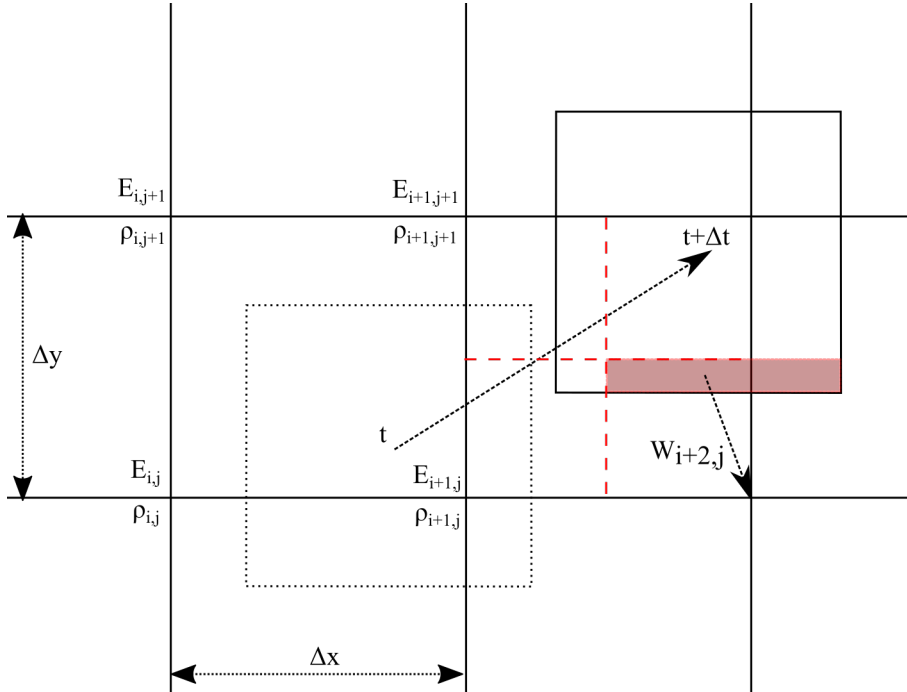


Figure 3.2: Schematic diagram of a superparticle moving in the grid from time t to $t + \Delta t$. The grid nodes g are denoted by the indices i, j for the dimensions x and y . The weighting of the particle to grid node $i + 2, j$ is shown as the red area of the particle.

In the PIC method, it is necessary to use so-called superparticles. A superparticle is a collection of particles that follow the same trajectory in phase-space [23]. Solving the Vlasov equation 2.13 for two sets of particles where one is the physical particles, and the other is a collection of physical particles, each carrying several physical particles gives the same solution given that the two sets have the same distribution in phase space [23, 25]. A PIC simulation is thus a kinetic solution, which updates the distribution function for each timestep. Thus, a PIC method can be considered as a way of solving the Vlasov equation (or Boltzmann equation if collisions are included). Using a first-order weighting scheme between the particle positions and grid nodes gives the superparticles a size equal to the grid cell size. The discretization therefore has a smoothing effect on particle positions [6].

A schematic diagram in 2-D of the uniform grid used in PINC is shown in figure 3.2. The field quantities are defined at the point where the grid lines intersect. The distance between the grid points is given by the spatial step

3. PINC-simulator

lengths $\Delta X, \Delta y$. In the schematic the grid nodes g are denoted by their indices i, j in the dimensions x and y . A particle moves from one position at time t to a different position in the next cell to the right at time $t + \Delta t$.

In addition to the statistical weight of the particle (i.e., the measure of how many physical particles form a superparticle), a weighting function is used to weight the particle quantities to the grid quantities and vice versa. Thus, the interpolation between particles and fields is done using a weighting function, which in PINC is based on B-splines [23]:

$$W(\vec{x}_g - \vec{x}_p) = b_n\left(\frac{x_g - x_p}{\Delta x}\right)b_n\left(\frac{y_g - y_p}{\Delta y}\right) \quad (3.1)$$

where x_g, y_g are the positions of the grid in x and y , and x_p, y_p are the positions of the particle in x and y . b_n is a B-spline of order n .

The shape of superparticles can then be defined through the weighting function as the shape function

$$S(\vec{x}_g - \vec{x}_p) = w_p \frac{W(\vec{x}_g - \vec{x}_p)}{\Delta x \Delta y}. \quad (3.2)$$

The shape function S defines the shape of the particles. In PINC, for the weighting function 3.1, we use the $n = 1$ B-spline, i.e., the first-order (linear) interpolation for the particle positions and Dirac-delta functions for their velocities. This choice of interpolation is commonly referred to as cloud in cell (CIC) since the particle's shape is the same as the shape of a computational cell. In figure 3.2 we see how this shape is interpolated to the grid. In simple terms, a particle within a cell is weighted by "how much" of the particle is close to each of the nodes that make up the cell.

The grid quantities can be computed as a sum of the particle shape functions:

$$\begin{aligned} \rho_g &= \sum_p q_p S(\vec{x}_g - \vec{x}_p), \\ \vec{J}_g &= \sum_p q_p \vec{v}_p S(\vec{x}_g - \vec{x}_p). \end{aligned} \quad (3.3)$$

Similarly, the field quantities at the particle can be computed from the grid using the weighting function:

$$\begin{aligned} \vec{E}_p &= \sum_g E_g W(\vec{x}_g - \vec{x}_p), \\ \vec{B}_p &= \sum_g B_g W(\vec{x}_g - \vec{x}_p). \end{aligned} \quad (3.4)$$

The most common method for updating particle positions and velocities is the Leapfrog algorithm [6, 43]. It is called the Leapfrog algorithm because it uses a staggered temporal scheme for the positions and velocities, such that positions

are defined at Δt and velocities are defined at $\Delta t/2$ for a timestep Δt . The finite difference scheme is first-order accurate, however, the addition of the velocities offset in time by $\Delta t/2$ in the Leapfrog algorithm makes the scheme second-order accurate in time. The particle positions and velocities are determined by the non-relativistic Newton–Lorentz equations of motion 2.4 and 2.5.

The equations can be discretized using finite differences and the staggered temporal scheme. Let time be defined at discrete points $t = n\Delta t$, where the timestep is Δt long. The discrete Newton–Lorentz equations at time t can be written as:

$$\begin{aligned} \frac{\vec{x}_p^{t+\Delta t} - \vec{x}_p^t}{\Delta t} &= \vec{v}_p^{t+\frac{\Delta t}{2}}, \\ \frac{\vec{v}_p^{t+\frac{\Delta t}{2}} - \vec{v}_p^{t-\frac{\Delta t}{2}}}{\Delta t} &= \frac{q_s}{m_s} (\vec{E}_p + \frac{\vec{v}_p^{t+\frac{\Delta t}{2}} - \vec{v}_p^{t-\frac{\Delta t}{2}}}{2} \times \vec{B}_p) \end{aligned} \quad (3.5)$$

A common way to avoid doing the full cross product of velocity and magnetic field is given by the Boris algorithm [7]:

$$\begin{aligned} \vec{v}_p^- &= \vec{v}_p^{t-\frac{\Delta t}{2}} + \frac{q_s}{m_s} \vec{E}_p \frac{\Delta t}{2}, \\ \vec{v}_p' &= \vec{v}_p^- + \vec{v}_p^- \times \vec{T}, \\ \vec{v}_p^+ &= \vec{v}_p^- + \vec{v}_p' \times \vec{S}, \\ \vec{v}_p^{t+\frac{\Delta t}{2}} &= \vec{v}_p^+ + \frac{q_s}{m_s} \vec{E}_p \frac{\Delta t}{2}, \end{aligned} \quad (3.6)$$

where we have used the same notation as in ref. [6]. The rotational parameters \vec{S}, \vec{T} are given by

$$\begin{aligned} \vec{T} &= \hat{\mathbf{B}}_p \cdot \tan\left(\frac{q_s \Delta t}{2m} B_p\right), \\ \vec{S} &= \frac{2\vec{T}}{1 + \vec{T}^2} \end{aligned} \quad (3.7)$$

The drawback of the Boris algorithm is understood by observing that the magnetic field does not enter the equations in a way such that the magnetic field can change the magnitude of the velocity, only the direction. Thus using the Boris algorithm implies that there is no transport of energy or momentum between the particles and the magnetic field [37]. However, this implication is well suited for use with a static magnetic field, such as within the electrostatic approximation (equation 2.12).

In the formulations thus far we have included both ρ and \vec{J} . However, for an electrostatic simulator only ρ is needed, due to the electrostatic approximation described in section 2.1. A solution for the electric field can be obtained by

3. PINC-simulator

discretizing equations 2.11, and 2.12. For the formulations of the field solver, we will for simplicity consider the one-dimensional equations, as extending them to several dimensions is trivial. Given an electric potential ϕ , the electric field can be computed with a centralized-space discretization

$$\vec{E}_i = -\frac{\phi_{i+1} - \phi_{i-1}}{2\Delta x}. \quad (3.8)$$

If the potentials are known the electric field is trivial to compute. However, what is known at a timestep is the charge density ρ , calculated from particle positions. The electric potentials can then be obtained by solving Poisson's equation 2.12 in a second-order centralized-space discretization

$$\frac{\phi_{i+1} - 2\phi_i + \phi_{i-1}}{\Delta x^2} = -\frac{\rho_i}{\epsilon_0} \quad (3.9)$$

Equation 3.9 can not be solved directly in the PIC method since ϕ_i depends on both ϕ_{i+1} and ϕ_{i-1} , which are unknowns. The most common approach is to use rapid spectral solvers, however, the spectral solvers are not well suited for parallel computations. Therefore, in PINC an iterative multigrid solver has been implemented. The solver is based on the multigrid method detailed in [20, 41], which uses the Gauss-Seidel even-odd scheme. In an iterative solver, the solution is iteratively moved towards the true solution by minimizing the residual.

3.2 Stability Criteria

In simulations, the topic of numerical stability is most important. Failing to meet the stability criteria of the simulated system will at least lead to large inaccuracies, and at worst catastrophic failure. It is therefore important to know the stability criteria, and make sure that they are met in all simulations.

3.2.1 Finite Grid

Due to the discretization of the field quantities on the grid, numerical instability can occur when the grid spatial step is too large. The mathematics of the finite grid instability are quite involved so we omit them here. However, this topic is discussed in depth in literature [6, 16, 23]. The criteria can be summarized as an inequality

$$\Delta x < C\lambda_D, \quad (3.10)$$

where the parameter C depends on the choice of interpolation scheme. For the CIC scheme used in PINC, it is generally accepted that $C \simeq \pi$. If the finite grid stability criteria are not met the simulated plasma will be artificially heated until the criteria are satisfied, or the simulation overflows and fails.

3.2.2 Finite Time

The forward integration in time of the positions and velocities of the particles has stability criteria associated with it. A straightforward von Neuman analysis of the time discretization leads to the relation [6, 16]:

$$\sin\left(\frac{\omega_N \Delta t}{2}\right) = \pm \frac{\omega \Delta t}{2} \quad (3.11)$$

where ω_N is the simulated frequency, and ω is the real frequency we wish to simulate. Since the sine function can only have values in the interval $[-1, 1]$ any real frequency where $\omega \Delta t / 2 > 1$ will be represented as a complex solution for ω_N . Such a solution will lead to a numerical instability that unboundedly grows. In practice, one should ensure that any simulation is nowhere close to this criteria, and it is common to use $\omega \Delta t = 0.1$ for any known frequency simulated.

3.2.3 The CFL Condition

First formulated by [11], the CFL condition states that no particle or phenomenon at a characteristic speed can travel past one grid cell in a single timestep. This can be formulated as an inequality [40]

$$\frac{\Delta x}{\Delta t} > C \quad (3.12)$$

There are several implications of the CFL condition. First, it must hold for any wave propagation. That is any electrostatic, magnetic, or electromagnetic wave can not travel past one cell per timestep. In the case of an electromagnetic wave that means we need to resolve the speed of light. Second, it also means that particles can not travel more than one cell per timestep, and it is generally accepted that the mean velocity in the bulk plasma should meet the CFL criteria. Lastly, the CFL condition can be interpreted as a constraint on the flow of information, where information can not travel more than one cell per timestep.

3.2.4 Additional Constraints

Recently it was shown that there is an additional constraint when including a magnetic field in the PIC scheme. If all the above constraints are met, but the magnetic field is strong enough that the gyroradius is smaller than the spatial step length, an instability will arise that is quite similar to the finite grid instability, and the heating of particles will lead to a larger gyroradius [18].

3.3 Object-Plasma interactions

The plasma-object (probe) calculations are performed in PINC with the standard capacitance matrix method [6, 30]. At present the object is assumed to be a perfect conductor, thus the charge is redistributed instantaneously (i.e., within

3. PINC-simulator

one timestep in the context of numerical simulation), on the object surface. To explain this process in some detail, we can begin with equation 4 from [30]

The difference between [30] and the implementation in PINC is that we use an electrostatic solver. In PINC we do not keep track of the current densities, thus we need to explicitly count the charges collected. The total charge of the object can be expressed as

$$Q_s^t = Q_s^{t-\Delta t} + \Delta q_s, \quad (3.13)$$

where Q_s^t is the total surface charge of the object at time t , and Δq_s is the collected charge from $t - \Delta t$ to t . To obtain Δq_s at each timestep we check each particle's position. If the particle is inside the boundary of the conductive object surface the particle is removed and its charge is added to Δq_s . For each grid node i on the object surface, the change in charge is related to the change in potential in the following way

$$\delta \rho_{s,i} = \sum_{j=1}^{N_s} C_{ij} \delta \phi_{sj}, \quad (i = 1, \dots, N_s) \quad (3.14)$$

Expanding equation 3.14 to include an equipotential value ϕ_c , we can write $\delta \phi_{sj} = \phi_c - \phi_{sj}$, giving

$$\delta \rho_{s,i} = \sum_{j=1}^{N_s} C_{ij} (\phi_c - \phi_{sj}), \quad (i = 1, \dots, N_s) \quad (3.15)$$

In PINC we obtain the values of ϕ_{sj} by equally distributing the total surface charge Q_s on the object surface nodes, and then solving the Poisson equation 2.12. Inserting equation 3.15 into a discrete equation for charge conservation [30] we obtain

$$\phi_c = \frac{\sum_i \sum_j C_{ij} \phi_{sj}}{\sum_i \sum_j C_{ij}} \quad (3.16)$$

where all variables are now known. Inserting this value for ϕ_c back into equation 3.15 gives us corrections to the charge on each surface node. Lastly, we solve for the potential on the whole grid (equation 2.12) again using the multigrid solver. During the charge redistribution, which is based on the capacitance matrix method, we thus always conserve charge and obtain an equipotential value inside the conductive surface.

The values of C are computed once during initialization and are found by using a known solution. The usual way to do this is to set a unitary charge on a grid node and then solve for the potential. The potential values obtained on the surface nodes are then one column of C^{-1} .

To bias the object, as a probe with a fixed potential value, we can set a value for the equipotential in equation 3.16. When we do this, the charge is no longer conserved. It is assumed that the object is connected to a source like a battery that can deliver the necessary current to give the values of charge in equation 3.15.

3.4 Parallelization in PINC

The parallelization scheme used in PINC was first devised by Sigvald Marholm as a part of his PhD work [25]. Many PIC codes have some sort of parallelization. However, the common way to parallelize a PIC simulator is to split the particles evenly onto several processors but solve the entire grid on one node. There are several reasons to do this. For older codes it is often that the method used to solve the grid has a low degree of parallelization, meaning that it will mostly add overhead to the computations, and slow down the solver. Secondly, many codes use spectral solvers, which are highly serial, because the implementations are simpler and thus quicker to implement and test. Solving the grid on one processor sets an upper limit on the possible size of a simulation. Both computational and memory limits for that node can be met when the grid size increases.

The main novelty and motivation for PINC's development was that of a fully parallelized simulator. Here both particles and the grid are split into several processors, such that simulations can in theory be scaled up indefinitely as long as we add the appropriate amount of processors.

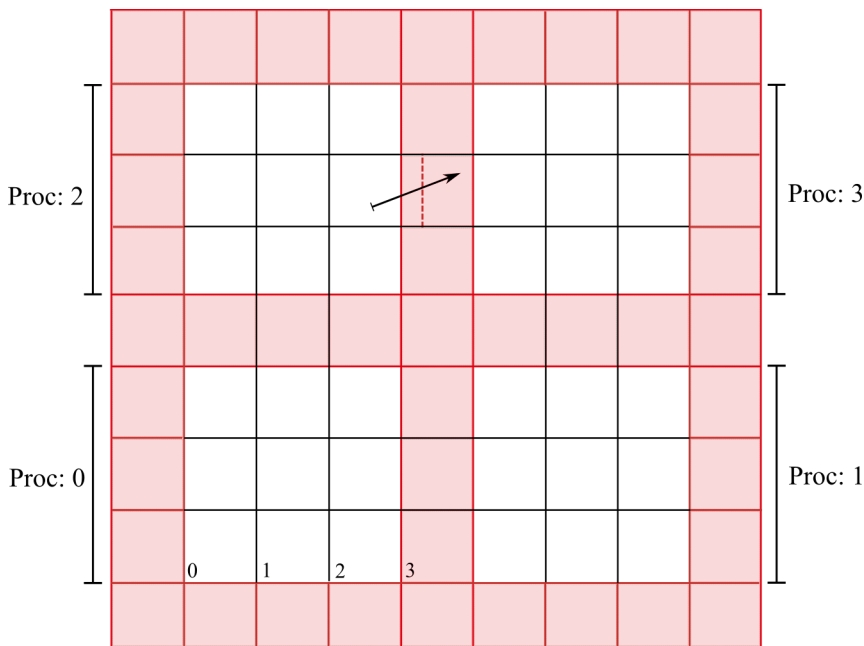


Figure 3.3: Schematic diagram of the parallelization employed in PINC. In the schematic, we use a 2-D grid with four processors.

A schematic diagram to help explain the parallelization in PINC is given in figure 3.3. For simplicity, we used a 2-D grid with four processors in this example. Each processor has its core space in white, which is surrounded by the so-called ghost cells in red. Each processor is responsible for computing all field

quantities on all of the vertices that are inside, or adjacent to the core space. For quantities that are dependent on the "next-over" grid value, e.g., $i + 1$ or $i - 1$, the ghost node value needs to be communicated to its neighbor. This is done with MPI communication operations. Since particles can exist in the ghost cell that is owned by two different processors, charge density needs to be added up in its MPI operation. The electric potential is solved iteratively, and each iteration solution on the outermost vertex of the core space is given as a ghost node to the neighbor. This generally happens hundreds to thousands of times per neighbor and per timestep.

Each processor holds a local array of particle positions and velocities where the particle positions are inside its own core space. For example, a particle whose position is inside one of the cells marked 0,1,2 will be owned by processor 0. A threshold is set that needs to be traversed before a particle's ownership is given to a neighboring processor. This threshold is indicated by the dotted red line in figure 3.3. If a particle moves across this threshold, its position and velocity vectors are sent via MPI send and receive operations from the current processor to the appropriate neighboring processor, and the particle is removed from the own local array of particles of the current processor. In the example in figure 3.3, a particle moves across the threshold, and ownership is given from processor 2 to 3. The reason for setting a threshold, and not simply using the edge of the ghost cell is that a particle that has a position exactly at the ghost cell edge would be sent back and forth indefinitely.

In the above description the boundary between the processors, called the ghost cells, is periodic. If all boundaries are periodic, the simulation is closed, and all information needed is transferred between two opposing outer boundaries as if they were inner boundaries.

3.5 Open boundaries

In PINC we set the boundary type on each boundary for each processor. If the boundary is connected to a different processor we call it an inner boundary, and it is always treated as a periodic boundary. If it is connected to the outside of the simulation we call it an outer boundary. We wish the outer boundaries to be open, where plasma can flow freely in and out. In the absence of a bulk plasma flow, this is achieved by setting a Dirichlet-type boundary on the whole ghost cell and filling the cell with a fresh Maxwellian plasma each timestep. The Dirichlet-type boundary can have any value, although changing the value on the whole outer boundary effectively shifts the null point of the electric potential, and the solution is the same except shifted by the boundary value. We therefore always set it to zero.

If we wish to include a bulk plasma drift, special handling of the boundary needs to be done. In this case, the simulation frame of reference is not the same as the particle's frame of reference. However, we know that the forces acting in the two frames must be the same due to Newton's first law of motion. Considering a single particle, the force \vec{F} in the simulation frame of reference

acting on it must then obey

$$\vec{F} = \vec{F}', \quad (3.17)$$

where \vec{F}' is the force in the frame co-moving with the bulk plasma. The two forces can be defined by the Lorentz force, and using that in the plasma frame of reference the plasma drift is zero $V'_d = 0$, the two forces are

$$\begin{aligned} \vec{F} &= q(\vec{V} \times \vec{B}) + q\vec{E} = 0, \\ \vec{F}' &= q\vec{E}' = 0, \end{aligned} \quad (3.18)$$

where also $\vec{F}' = 0$ since we set a Dirichlet boundary, so $\vec{E}' = 0$. Using a centered finite difference, equation 3.8 for \vec{E} can then be written

$$E_x = -\nabla\phi = \frac{\phi_{i+1} - \phi_{i-1}}{2\Delta x} = -\vec{V}_d \times \vec{B}. \quad (3.19)$$

Here we only show the equation for one of the dimensions x , since it is the same for the others. Note that this equation only has non-zero values in the direction perpendicular to both \vec{V}_d and \vec{B} . This can be rewritten into an equation for the electric potential at

$$\phi_{i+1} = 2\Delta x \vec{V}_d \times \vec{B} + \phi_{i-1} \quad (3.20)$$

which gives the more general equation:

$$\phi_i = i\Delta x \vec{V}_d \times \vec{B} + \phi_0, \quad i = [0, 1, 2 \dots n_x], \quad (3.21)$$

where $\phi_0 = 0$ can again be used because of the Dirichlet boundary set to zero, or it can be set to any value since this would only shift the zero point and thus solve an equivalent system. In PINC it is set to $\frac{n_x \Delta x \vec{V}_d \times \vec{B}}{2}$ such that the $\phi_i = 0$ point is in the center of the simulated domain.

3.6 Charged-neutral collisions

The collision module is implemented using the Monte-Carlo null-collision (MCC) [43] method described earlier by [42], with the exception of a linear approximation to the collision frequencies. It is a similar method as in [35]. For additional context see [5]. A more in-depth explanation of the implementation in PINC is given in [8].

The probability of a particle colliding within a timestep is given by

$$P_i = 1 - \exp(-\nu_i \Delta t) \quad (3.22)$$

Where ν_i is the collision frequency for collision type i . The null-collision method is based on the idea of introducing a constant maximum possible collision frequency. The maximum collision frequency will be the maximum of the sum of added collision types. This is shown schematically in figure 3.4.

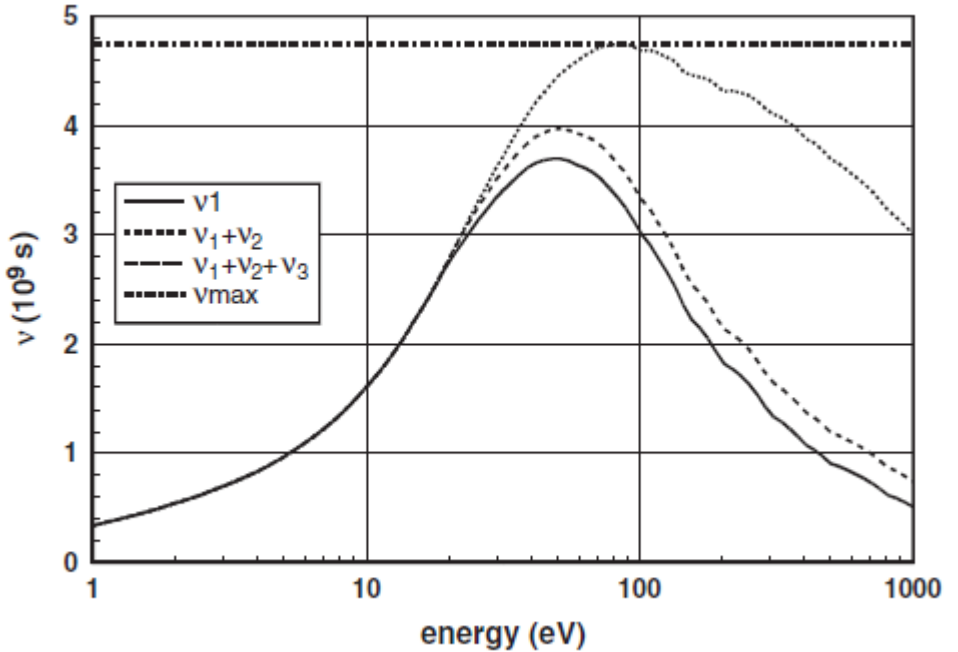


Figure 3.4: Schematic of different collision types and their frequencies as functions of energy. Diagram taken from [43].

Inserting ν_{max} into equation 3.22 gives the maximum collision probability P_{max} from which we can define the maximum possible number of particles to collide within a timestep

$$N_C = P_{max} N_T \quad (3.23)$$

where N_T is the total number of particles in the simulation. Different collision types will have different collision cross-sections σ_i , and scattering angles. In PINC we have implemented charge-exchange and elastic collisions for ions, and elastic for electrons. The scattering angles are calculated as in [42].

In PINC there are three methods for obtaining collision cross-sections: zeroth ($\nu = constant$), constant, and functional. In papers I and III we used the constant type collision cross-section. At low energies, collisional cross-sections are calculated using the definition of collision frequency:

$$\nu_i = n_g(x) \sigma_i(\epsilon) v(\epsilon), \quad (3.24)$$

where i denotes the collision type and x is the position. ϵ is the particle energy. n_g is the neutral density, and v is the relative particle velocity. In equation 3.24 the collision frequency can be either the collision frequency of one particle if

using the neutral density at the particle position and the particle's velocity, or it can be the average collision frequency of the whole system if using average values.

To maintain the collision frequency in the system we solve eq. (3.24) for the cross-section, and use the average values:

$$\sigma_i(\epsilon) = \frac{\nu_i}{n_{g,avg}v_{avg}} \quad (3.25)$$

where $n_{g,avg}$ is the constant average neutral density, and v_{avg} is the average velocity of the particles. This gives us a model with a linear collision frequency in velocity i.e., $\nu \propto v$.

Due to discretization in time, there is a probability that a particle undergoes more than one collision per time step. The number of missed particle collisions can be calculated [42, 43]

$$r_i \approx \sum_{k=2}^{\infty} P_i^k = \frac{P_i^2}{1 - P_i} \quad (3.26)$$

This leads to an additional simulation constraint, $\nu_{T,max}\Delta t \ll 1$. This constraint can significantly increase the number of time steps needed for moderate to high collision frequencies.

3.7 Testing and Verification

We will present here some of the tests done for verification of PINC. The following is a non-exhaustive list of verification tests performed:

- Multigrid solver was run on Heaviside and sinus rho test. Any function that has known second derivatives can be used to measure the error in equation 2.12. For example, distributing the particles in the domain according to a sine function such that $\rho(\vec{x})$ is a sine function, the double derivative will also be a sine function. For details see [20].
- The first test of the full PIC cycle performed was the Landau damping test, one of the hallmarks of the PIC simulator. In this test, one species is offset such that an electric potential is added between the species. This leads to Langmuir oscillations where plasma period and Landau damping and energy conservation can be calculated theoretically. All values were within a few percent, although the error depends on discretization, and a finer step in time and space leads to a lower error.
- The Boris algorithm was tested. The tests were performed on single particles where the field contributions from particles were nullified. With static electric and magnetic fields, one can test that correct gyroradius, gyrofrequency, and $\vec{E} \times \vec{B}$ drift velocity and direction.

3. PINC-simulator

- For *closed/periodic boundaries*, it was verified that there is a constant number of particles in a fully distributed simulation. When particles (and total energy) move between subdomains it is important that the total number of particles is conserved.
- For *open boundaries*, where the simulation edge is connected to a Maxwellian plasma, the total simulated number of particles averaged over several ion plasma periods should be constant. This was tested with several drift velocities and a few very long simulations. The same tests were done for energy conservation, although this will be stabilized by the boundary and hence testing energy is not precise in this case. However, large changes initially should not occur.
- Object-plasma interactions were tested against theoretical expressions of the OML-charging of a floating spherical probe, and the biased spherical probe both in a stationary, non-magnetized, Maxwellian plasma. Some version of this test is detailed in all papers included in this thesis. In addition, large objects' floating potential in a non-drifting plasma will be decided by the thermal currents. (equation 2.26).
- The collisional module was rigorously tested in [8]. The tests included the correct number of collisions throughout the domain. Averaging over many collisions should not have a preferred direction in space. Particle distributions and average energy for ions converge towards neutral species characteristics.

In addition, several reproductions of earlier papers have been done. There are too many of these to list all, so we list here a few the author was involved in.

- Reproduced simulation results done by Oppenheim et al. on the Farley-Buneman instability. In particular, we get the same phase diagram ω/k as in [34], and similar temperature changes. A discussion on these results from PINC is done in [8]. A comparison is also made with [34, 35].
- Reproduced ion focusing results from [28, 29]. In the reproduction in PINC, it was observed that the Mach angle, charging, and peak ion densities are the same, and the wake geometry overall is similar.

3.8 Status of PINC

PINC has been developed to a point now where it can be considered a state-of-the-art 3D kinetic particle-in-cell electrostatic simulator capable of simulating large-scale plasma simulations and object-plasma interactions. While several similar simulators exist, to the best of our knowledge none of them have the full feature set of PINC in addition to the high degree of parallelization and efficiency.

In addition to the features highlighted, several new features are under development in PINC. Of note is the PIC neutral module, where neutral particles

can be simulated in the PIC framework. In the future, this can be used to simulate collisional shocks for objects in super- and hypersonic drifts. A method for energy transport between neutrals and charged particles needs to be devised, such that energy conservation is maintained. In the standard PIC-MCC method energy is not conserved. The method is tested for neutral-only simulations in a shock tube test where the correct sound speed was observed.

Object-plasma interactions for single objects are well-tested. Multiple objects have recently been implemented by Jan Deca as a part of a new project. The implementation includes circuit calculations between objects, such that they can be biased with respect to each other.

An off-the-shelf MG solver (hypre C library) has been implemented, however, the work stalled when it was found that it was not significantly faster than the PINC MG solver. The hypre-based solver is likely more efficient for very large simulations, and the implementation and testing should therefore be completed.

Photoemission was implemented by Trym Nielsen [32] as a part of his master's thesis. This needs a review and some more testing, although it showed promising and accurate results in selected cases.

Chapter 4

Summary of Papers

We turn our focus to the new results we found in this PhD project. In this PhD work we use numerical methods (PIC), which we have just introduced, to improve instrumentation (LP), which are used to extend our knowledge of plasma and ionospheric physics. The aims of the papers included were all chosen through a balance of being impactful, possible, and simple enough to be explainable. There is a problem in modeling and the current widely employed methods of machine learning in physics that they are often poorly explained, and used as a black box. This severely limits such models, or the applicability and adoption of results based on such models. In this PhD project, there has therefore been a focus on explaining the results and having a clear path to adopting the results in other projects.

Idealized probe theory (OML) is a perfect theory under perfect conditions. In reality, conditions are never perfect. It is well known that realistic conditions will have several sources of errors due to the non-ideal conditions, however, it is not clear to what degree these sources will impact probe measurements. Often the ideal theory assumptions are listed and then neglected. For most conditions in space, ideal theory will be a good approximation, however, the neglect is problematic since we lose control over how much we know. There is an error present, whose magnitude is unknown. In particular, the OML theory is based on simple geometries and assumes among others collisionless non-magnetized conditions. The conditions are non-trivial in different regions of the ionosphere and many other parts of space. We have therefore papers focusing on each of these conditions: collisional plasma, non-ideal probe geometry, and magnetized plasma.

4.1 Paper I (Electron–neutral collisions effects on Langmuir probe in the lower E-region ionosphere)

In this paper, we investigate the effects of charged-neutral collisions on needle-type Langmuir probes. It is found that the probe currents are increased as the electron mean free path approaches the Debye length. Summary of Paper I:

1. A set of simulated data for two probe biases was made using the Particle-in-Cell simulation code PINC.
2. The set uses simulation input parameters based on EISCAT Svalbard Radar (ESR) data collected at 120 km altitude at the launch of the Investigation of Cusp Irregularities-4 (ICI-4) sounding rocket. The probe biases have the same values as two of the four probes on the m-NLP system flown

4. Summary of Papers

on the ICI-4 rocket. In addition to the two probe voltages, six collision frequencies are simulated along with a collision-free simulation.

3. A model was built to correct the currents to two probes with different probe biases for a specific use case.
4. In the case of the ICI-4 sounding rocket, the model function is shown to be accurate down to 100km height in the context of the simulations.
5. It is discussed how multi-probe measurements can be accurate even in the collisional regime if the impact on the currents is independent of probe voltage. However, this is not the case for the simulations in this paper, although the differences are small enough to be within the simulation error.
6. It is discussed how the method employed to build models for specific use cases can be deployed in other scientific missions focusing on the collisional regime of the ionosphere.

4.2 Paper II (Effects of Guard and Boom on Needle Langmuir Probes Studied with Particle in Cell Simulations)

Several assumptions are made explicitly, or often implicitly when designing and deploying needle Langmuir probes. In this paper two assumptions on the probe geometry are investigated in detail. This paper was motivated by the results of Marholm and Marchand [26], where it was shown that end effects have an impact on the current at relatively long probe lengths.

1. The two assumptions tested are: (i) that the guard length needs to be a few Debye lengths, and (ii) that the guard radius does not impact the currents.
2. A guard is designed to isolate the probe electrically from the mounting point. Since the mounting point and the biased probe have a potential difference, unwanted currents will flow between them if they are not sufficiently isolated.
3. It is found that the common 1-2 Debye lengths for the guard length are not sufficient, and at least 6-8 Debye lengths should be used.
4. Since the guard is biased at the same potential as the probe it is commonly assumed that its geometry will not impact the currents, as long as it is far enough from the mounting point. We see that this is not the case for large radii, where the large guard acts as a current sink, such that the probe currents get lower. However, this effect is negligible when the guard is small with respect to the Debye length.
5. For a small guard radius there are other complex effects at play, that in this case do not impact the total currents greatly. However, it is discussed

how these effects may become important at specific probe geometries and probe potentials.

We concluded that simulating the large number of simulations needed to build a general model that corrects for these effects will need further justification since most of these effects can be avoided with proper care taken in designing and deploying the probe. More work on the effects seen in the small guard radius regime should be done to find the limits of the particle "funneling" effect discussed in sections 3.2 and 3.3 of Paper II.

4.3 Paper III (Spherical Langmuir probes in magnetized plasma. A model based on Particle-in-Cell simulations)

In this paper, a new model for magnetized spherical Langmuir probes, based on PIC simulations is built. The simulated parameters are loosely based on simulated ionospheric input parameters, however, the analysis and modeling are done in dimensionless parameters spanning most ionospheric conditions.

1. The simulations show that even moderate magnetization can lead to a significant impact on the currents of up to an 80 – 90% reduction. This means that this is one of the most significant sources of error to Langmuir probes in the ionosphere that use non-magnetized theories.
2. A dimensional analysis to determine parameters that the simulations need to describe is performed using Buckingham's π theorem.
3. It is determined that under the same assumptions as the OML theory, we need simulated data points for the parameters probe potential V_p , and magnetic field β to fully describe the dimensionless set of parameters given in equation 5.
4. The assumptions used in agreement with the OML theory are that the probe radius is small with respect to the Debye length and that the plasma parameter approaches infinity (is sufficiently large).
5. The main set of simulations simulates a spherical Langmuir probe in a range of probe potentials and magnetic field values.
6. As an initial step a simplified model was built on a single probe bias value. This model is accurate for probe biases close to the dimensionless probe potential $\eta \approx 52$, however, due to the large change in currents the error from using this simplified model is still much smaller than using non-magnetized theory.
7. A model spanning the full set of dimensionless parameters was built using a multivariate least squares regression. The model is valid for the simulated range of parameters $\eta \in [15 - 98]$, and $\beta \in [0 - 3.2]$.

4. Summary of Papers

8. Both models have a good fit to the simulated data shown with the 'goodness of fit' R^2 , Mean Absolute Error, and Mean Squared Error parameters.
9. It is discussed how the models can be considered a modification to the probe effective surface area, or the available surface area with respect to I_0 , where I_0 is the current given from the OML theory.
10. In the ionosphere, one area where magnetization likely has a large impact is in the lower altitude, namely the E-region ionosphere. In this region, charged-neutral collisions also come into effect. Therefore an example of collisional effects is also included. It is shown that moderate magnetization is important also in the collisional regime and that collisions behave similarly to earlier work [48] and paper I. However, the combination of magnetization and collisions makes the problem highly complex, and many more simulations would be needed to describe it through simulations.

The final model presented here is straightforward to deploy in space missions. It is a model for spherical Langmuir probes, which are flown on many missions (see introduction of paper). However, in the lower regions of the ionosphere needle type Langmuir probes are often used since the Debye length gets shorter closer to Earth, and they are easier to miniaturize. This is typically also the region where magnetization would be most impactful. Therefore more simulations and modeling for cylindrical probes would be beneficial.

Chapter 5

Discussion

In this section, I will expand on the discussions given in papers I-III. The discussion will be given in the context of the overall PhD project.

In the papers included as a part of this thesis, we build functions to correct some known current I_0 , which is in these cases the OML current. We can consider a spherical probe and for this example also assume that the results in paper I are applicable to a sphere. A general function including several effects needs in general to be a function of all parameters. For example, if we combine the collisional effects seen in paper I with the magnetic effects seen in paper III the general function will need to depend on both the collisional parameter λ and the magnetic parameter β

$$\frac{I}{I_{OML}} = f(\lambda, \beta, \eta), \quad (5.1)$$

and we know from paper III that it needs to depend on the probe potential η . In this case, there are three dimensions we need to expand and the number of simulations needed is $n^d = 10^3 = 1000$ for ten simulations in each dimension. However, for the collisional effects, the η dependence is weak, and therefore it is reasonable to assume that the collisional parameter is linearly independent of the magnetic and potential, such that

$$\frac{I}{I_{OML}} = f_1(\lambda) + f_2(\beta, \eta). \quad (5.2)$$

f_1 and f_2 can therefore be expanded separately and the number of simulations needed is $10 + 100 = 110$. This assumption is not trivial since the η dependence is not completely absent, and we do not know if it holds for all λ and η . However, this is an approach that can yield satisfactory results with far fewer simulations needed. When adding even more parameters, carefully evaluating the dependence and whether they can be considered independent might be a necessity for building a general function.

When considering a cylindrical probe the problem is further complicated by the end-effects [26] and magnetic field angle. In addition, plasma flow should be included. A function expanded on all parameters will then need 10^6 simulations, and these are only the parameters we know to be impactful. If we assume linear independence on the magnetic field angle in addition to the end effects being linearly independent of all other parameters we can write the correction function as

$$\frac{I}{I_{OML}} = f_1(\lambda, \Theta) + f_2(\beta, \eta) + f_3(l_p, \eta), \quad (5.3)$$

where f_3 is the function from [26] and is already known. We then need $100 + 100 + 100$ simulations for a general function, however, we only need 200 new simulations. f_2 and f_3 both depend on η and are therefore clearly not independent. However, it is still possible that the assumption holds to a good approximation. In any case, a general function including several corrections would be useful, and 200 additional simulations are possible to do, 10^6 is infeasible.

In paper II it is left as future work to study the focusing effect observed at certain values of r_g/r_p . It is also mentioned that the probe length might play a role. The effect is accompanied by a sheath with an unusual shape, which we called a funnel shape. Since the sheath shape changes greatly it is reasonable that this shape will also impact current collection in a magnetized case. If this is so, the limits given in the paper may need to be accompanied by a limit on magnetization. It is also possible that the guard radius will need to be included in a general function if such effects exist.

Large changes in the sheath were observed in the collisional plasma, with changing the guard geometry, and in magnetized cases. The sheath shape is important for the probe current, and it is difficult to predict what all of these changes combined would mean for the probe currents. It is therefore possible that a general function is not usable without expanding all parameters in one function. The complexity of the problem, and the possibility of a solution being infeasible, is not a reason to leave this question without further investigation, it is rather the opposite.

5.1 Future work

Papers I-III have discussions of future work. In this section, we will highlight some of the future work discussed in the papers as bullet points, and add one new point in the end.

- A study of the effects of magnetization on a cylindrical probe should be performed, and if possible a correction function should be constructed. Such a function will need the magnetic field angle in addition to the probe length along with the two parameters from the spherical case as parameters. This makes the problem difficult, however, as discussed above, it may be possible to do some simplifications.
- The funnel shape on the sheath in paper II with an increase in the current was an unexpected result. The effect is small in the cases simulated in the paper, however, we do not know if there exists a specific configuration where this effect becomes significant. This should be investigated.
- Work towards a general empirical function correcting for all effects would be beneficial. The feasibility of building such a function is discussed above, and further details are discussed in papers II-III.

An overview study where different corrections are evaluated for the m-NLP system where different corrections impact at different times during a flight

should be highlighted. This can be done without a general function, if it is understood that the corrections are a measure of the impact of an effect and the actual currents are still unknown. In areas where all corrections are small, we will know that the data has a high quality. The corrections we can evaluate are the collisional effects from paper I, the magnetic effect if this is expanded to the cylindrical case, and the finite length (end effect) modeled in [26]. We can also flag areas if the criteria of paper II are violated.

Bibliography

- [1] Anderson, P. C. “Characteristics of spacecraft charging in low Earth orbit”. en. In: *Journal of Geophysical Research: Space Physics* vol. 117, no. A7 (2012).
- [2] Barjatya, A. et al. “Invited article: data analysis of the floating potential measurement unit aboard the international space station”. eng. In: *The Review of Scientific Instruments* vol. 80, no. 4 (Apr. 2009), p. 041301.
- [3] Baumjohann, W. and Treumann, R. A. *Basic Space Plasma Physics*. en. World Scientific, 1997.
- [4] Bekkeng, T. A. et al. “Design of a multi-needle Langmuir probe system”. In: *Measurement Science and Technology* vol. 21, no. 8 (July 2010). Publisher: IOP Publishing, p. 085903.
- [5] Birdsall, C. “Particle-in-cell charged-particle simulations, plus Monte Carlo collisions with neutral atoms, PIC-MCC”. In: *IEEE Transactions on Plasma Science* vol. 19, no. 2 (Apr. 1991). Conference Name: IEEE Transactions on Plasma Science, pp. 65–85.
- [6] Birdsall, C. K. and Langdon, A. B. *Plasma physics via computer simulation*. en. McGraw-Hill, 1985.
- [7] Boris, J. “Relativistic plasma simulation-optimization of a hybrid code”. In: *Proceeding of Fourth Conference on Numerical Simulations of Plasmas*. 1970.
- [8] Brask, S. M. “Instabilities in Collisional Plasmas Studied by means of 3-D Kinetic Particle-in-Cell Simulations”. MA thesis. University of Oslo, 2018.
- [9] Chen, F. F. *Introduction to Plasma Physics and Controlled Fusion*. en. 3rd ed. Springer International Publishing, 2016.
- [10] Committee, P. S. *Plasma science : from fundamental research to technological applications*. eng. ISBN: 0309052319 Place: Washington, D.C. 1995.
- [11] Courant, R., Friedrichs, K., and Lewy, H. “On the Partial Difference Equations of Mathematical Physics”. In: *IBM J. Res. Dev.* vol. 11, no. 2 (Mar. 1967), pp. 215–234.
- [12] Dinklage, A. et al. “Magnetic configuration effects on the Wendelstein 7-X stellarator”. en. In: *Nature Physics* vol. 14, no. 8 (Aug. 2018). Number: 8 Publisher: Nature Publishing Group, pp. 855–860.
- [13] Fitzpatrick, R. *Plasma Physics: An Introduction*. en. Google-Books-ID: 0RwbBAAAQBAJ. CRC Press, Aug. 2014.

- [14] Garrett, H. B. “The charging of spacecraft surfaces”. en. In: *Reviews of Geophysics* vol. 19, no. 4 (1981), pp. 577–616.
- [15] Hoang, H. et al. “A study of data analysis techniques for the multi-needle Langmuir probe”. en. In: *Measurement Science and Technology* vol. 29, no. 6 (May 2018). Publisher: IOP Publishing, p. 065906.
- [16] Hockney, R. W. and Eastwood, J. W. *Computer Simulation Using Particles*. en. CRC Press, Jan. 1988.
- [17] Holta, V. “Dynamics of a Plasma Blob Studied With Particle-In-Cell Simulations”. MA thesis. University of Oslo, 2018.
- [18] Horký, M., Miloch, W. J., and Delong, V. A. “Numerical heating of electrons in particle-in-cell simulations of fully magnetized plasmas”. In: *Physical Review E* vol. 95, no. 4 (Apr. 2017), p. 043302.
- [19] Jacobsen, K. S. et al. “A new Langmuir probe concept for rapid sampling of space plasma electron density”. en. In: *Measurement Science and Technology* vol. 21, no. 8 (July 2010), p. 085902.
- [20] Killie, G. V. “A Parallel Multigrid Poisson Solver for PINC, a new Particle-in-Cell Model”. MA thesis. University of Oslo, 2016.
- [21] Laframboise, J. G. “Theory of spherical and cylindrical langmuir probes in a collisionless, maxwellian plasma at rest”. PhD thesis. University of Toronto, June 1966.
- [22] Laframboise, J. G. and Sonmor, L. J. “Current collection by probes and electrodes in space magnetoplasmas: A review”. en. In: *Journal of Geophysical Research: Space Physics* vol. 98, no. A1 (1993), pp. 337–357.
- [23] Lapenta, G. “Particle simulatipenns of space weather”. In: *Journal of Computational Physics*. Special Issue: Computational Plasma Physics Special Issue: Computational Plasma Physics vol. 231, no. 3 (Feb. 2012), pp. 795–821.
- [24] Makarevich, R. A. et al. “Auroral E-Region as a Source Region for Ionospheric Scintillation”. en. In: *Journal of Geophysical Research: Space Physics* vol. 126, no. 5 (2021), e2021JA029212.
- [25] Marholm, S. “The Unstructured Particle-In-Cell Method with Applications for Objects in Ionospheric Plasmas”. en. Accepted: 2020-02-12T11:52:26Z. Doctoral thesis. 2020.
- [26] Marholm, S. and Marchand, R. “Finite-length effects on cylindrical Langmuir probes”. In: *Physical Review Research* vol. 2, no. 2 (Apr. 2020). Publisher: American Physical Society, p. 023016.
- [27] Metel, A. S. et al. “Filling the vacuum chamber of a technological system with homogeneous plasma using a stationary glow discharge”. en. In: *Plasma Physics Reports* vol. 35, no. 12 (Dec. 2009), pp. 1058–1067.
- [28] Miloch, W. J. “Numerical simulations of dust charging and wakefield effects”. en. In: *Journal of Plasma Physics* vol. 80, no. 6 (Dec. 2014). Publisher: Cambridge University Press, pp. 795–801.

-
- [29] Miloch, W. J., Trulsen, J., and Pécseli, H. L. “Numerical studies of ion focusing behind macroscopic obstacles in a supersonic plasma flow”. eng. In: *Physical Review. E, Statistical, Nonlinear, and Soft Matter Physics* vol. 77, no. 5 Pt 2 (May 2008), p. 056408.
- [30] Miyake, Y. and Usui, H. “New electromagnetic particle simulation code for the analysis of spacecraft-plasma interactions”. In: *Physics of Plasmas* vol. 16, no. 6 (June 2009). Publisher: American Institute of Physics, p. 062904.
- [31] Mott-Smith, H. M. and Langmuir, I. “The Theory of Collectors in Gaseous Discharges”. In: *Physical Review* vol. 28, no. 4 (Oct. 1926). Publisher: American Physical Society, pp. 727–763.
- [32] Nielsen, T. E. “Photoemissive charging of the Mercury Magnetospheric Orbiter studied by means of 3D Particle-In-Cell simulations”. MA thesis. University of Oslo, 2020.
- [33] Nishitani, N. et al. “Review of the accomplishments of mid-latitude Super Dual Auroral Radar Network (SuperDARN) HF radars”. In: *Progress in Earth and Planetary Science* vol. 6, no. 1 (Mar. 2019), p. 27.
- [34] Oppenheim, M. M., Dimant, Y., and Dyrud, L. P. “Large-scale simulations of 2-D fully kinetic Farley-Buneman turbulence”. In: *Ann. Geophys.* vol. 26, no. 3 (Mar. 2008), pp. 543–553.
- [35] Oppenheim M. M. and Dimant Y. S. “Kinetic simulations of 3-D Farley-Buneman turbulence and anomalous electron heating”. In: *Journal of Geophysical Research: Space Physics* vol. 118, no. 3 (Feb. 2013), pp. 1306–1318.
- [36] Pécseli, H. “Waves and Oscillations in Plasmas”. In: *Waves and Oscillations in Plasmas. Series: Series in Plasma Physics, ISBN: 978-1-4398-7848-4. Taylor & Francis, Edited by Hans Pécseli* (Sept. 2012).
- [37] Qin, H. et al. “Why is Boris algorithm so good?” In: *Physics of Plasmas* vol. 20, no. 8 (Aug. 2013), p. 084503.
- [38] Rebut, P.-H. “ITER: the first experimental fusion reactor”. In: *Fusion Engineering and Design* vol. 30, no. 1 (1995), pp. 85–118.
- [39] Sampl, M. et al. “Juno Waves High Frequency Antenna Properties”. en. In: *Radio Science* vol. 56, no. 9 (2021), e2020RS007184.
- [40] Trivellato, F. and Raciti Castelli, M. “On the Courant–Friedrichs–Lewy criterion of rotating grids in 2D vertical-axis wind turbine analysis”. In: *Renewable Energy* vol. 62, no. C (2014), pp. 53–62.
- [41] Trottenberg, U., Oosterlee, C. W., and Schuller, A. *Multigrid*. en. Academic Press, Nov. 2000.
- [42] Vahedi, V. and Surendra, M. “A Monte Carlo collision model for the particle-in-cell method: applications to argon and oxygen discharges”. In: *Computer Physics Communications. Particle Simulation Methods* vol. 87, no. 1 (May 1995), pp. 179–198.

- [43] Verboncoeur, J. P. “Particle simulation of plasmas: review and advances”. In: *Plasma Physics and Controlled Fusion* vol. 47, no. 5A (May 2005), A231–A260.
- [44] Vlasov, A. A. “THE VIBRATIONAL PROPERTIES OF AN ELECTRON GAS”. en. In: *Soviet Physics Uspekhi* vol. 10, no. 6 (June 1968). Publisher: IOP Publishing, p. 721.
- [45] Wahlström, M. K. et al. “Improved Langmuir probe surface coatings for the Cassini satellite”. In: *Thin Solid Films* vol. 220, no. 1 (Nov. 1992), pp. 315–320.
- [46] Wannberg, G. et al. “The EISCAT Svalbard radar: A case study in modern incoherent scatter radar system design”. en. In: *Radio Science* vol. 32, no. 6 (1997), pp. 2283–2307.
- [47] Whipple, E. C. “Potentials of surfaces in space”. en. In: *Reports on Progress in Physics* vol. 44, no. 11 (Nov. 1981), pp. 1197–1250.
- [48] Zakrzewski, Z. and Kopiczynski, T. “Effect of collisions on positive ion collection by a cylindrical Langmuir probe”. en. In: *Plasma Physics* vol. 16, no. 12 (Dec. 1974). Publisher: IOP Publishing, pp. 1195–1198.

Papers

Paper I




Electron–neutral collisions effects on Langmuir probe in the lower E-region ionosphere

S. M. Brask, S. Marholm, F. Di Mare, S. Adhikari, A. Spicher, T. Takahashi, W. J. Miloch

Published in *Physics of Plasmas*, March 2022, volume 29, issue 3, DOI: 10.1063/5.0079761.

RESEARCH ARTICLE | MARCH 21 2022

Electron–neutral collisions effects on Langmuir probe in the lower E-region ionosphere

S. M. Brask ; S. Marholm; F. Di Mare ; S. Adhikari; A. Spicher; T. Takahashi; W. J. Miloch 

 Check for updates

Phys. Plasmas 29, 033511 (2022)
<https://doi.org/10.1063/5.0079761>



CrossMark

Articles You May Be Interested In

Modeling of current characteristics of segmented Langmuir probe on DEMETER

Phys. Plasmas (May 2013)

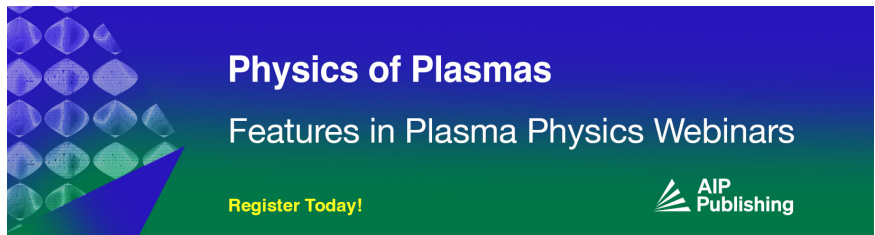
Spacecraft charging analysis with the implicit particle-in-cell code iPic3D

Phys. Plasmas (October 2013)

Sheath-induced distortions in particle distributions near enhanced polar outflow probe particle sensors


Phys. Plasmas (July 2014)

15 September 2023 09:46:55



Physics of Plasmas
Features in Plasma Physics Webinars

Register Today!



Electron–neutral collisions effects on Langmuir probe in the lower E-region ionosphere

Cite as: Phys. Plasmas **29**, 033511 (2022); doi: 10.1063/5.0079761

Submitted: 24 November 2021 · Accepted: 2 March 2022 ·

Published Online: 21 March 2022



S. M. Brask,^{1,a)} S. Marholm,¹ F. Di Mare,¹ S. Adhikari,¹ A. Spicher,² T. Takahashi,³ and W. J. Miloch^{1,b)}

AFFILIATIONS

¹Department of Physics, University of Oslo, P.O. Box 1048, Blindern, 0316 Oslo, Norway

²Department of Physics and Technology, University of Tromsø, P.O. Box 6050, Langnes, 9037 Tromsø, Norway

³National Institute of Maritime, Port, and Aviation Technology, 6-38-1, Shinkawa, Mitaka-shi, Tokyo 181-0004, Japan

^{a)} Author to whom correspondence should be addressed: s.m.brask@fys.uio.no

^{b)} Electronic mail: w.j.miloch@fys.uio.no

ABSTRACT

We present the first set of particle-in-cell simulations including Monte Carlo collisions between charged and neutral particles used to simulate a cylindrical Langmuir probe in the electron saturation regime with a collisional electron sheath. We use a setup focused on the E-region ionosphere; however, the results of these simulations are analyzed in a general sense using dimensionless values. We find that the electron currents get enhanced as the collision frequency for electrons increases and the values of $\lambda_e/\lambda_D \rightarrow 1$, where λ_e is the electron mean free path and λ_D is the electron Debye length. In addition, we apply the simulation results to a sounding rocket experiment and show how we can correct the currents for the Investigation of Cusp Irregularities-4 sounding rocket due to collisions while it flies through the E-region.

© 2022 Author(s). All article content, except where otherwise noted, is licensed under a Creative Commons Attribution (CC BY) license (<http://creativecommons.org/licenses/by/4.0/>). <https://doi.org/10.1063/5.0079761>

I. INTRODUCTION

Langmuir probes have a long history and widespread usage in space measurements. The probes are usually designed with either spherical or cylindrical geometries, and they may have different setups for single- or multi-probe measurements. For example, the Rosetta spacecraft¹ had a two-probe setup designed for low-density measurements. This concept was inherited from earlier missions, like the Freja F4² and Cluster³ missions, targeting relatively high density plasma in the ionosphere and magnetosphere. Another modern Langmuir probe system is the multi-needle Langmuir probe (m-NLP) used on the Investigation of Cusp Irregularities (ICI) rockets,^{4–6} and NorSat-1.⁷ The different setups require different theoretical equations to extract plasma parameters like temperature, density, and electric potential from the surrounding plasma. Usually, these theories are based on orbital limited (OML) theory,⁸ which, in the electron saturation region, predicts that the current I_p to a probe p is given by

$$I_p = I_{th}K \left(1 + \frac{q(V_p + V_f)}{k_B T_e} \right)^\beta, \quad (1)$$

where k_B is the Boltzmann constant, q the elementary charge, and T_e the electron temperature. K and β are dependent on the probe shape.

In particular, $K = 2/\sqrt{\pi}$ and $\beta = 0.5$ for ideal infinite length cylindrical probes and $K = \beta = 1$ for spherical probes. V_p and V_f are the probe potential and spacecraft body floating potential, respectively.

$I_{th} = n_e q S \sqrt{\frac{k_B T_e}{2\pi m_e}}$ is the thermal electron current, where n_e and m_e are the electron density and mass with S being the surface area of the probe.

For the m-NLP system, ideally, we can eliminate some of the free parameters in Eq. (1) by taking the difference of the square of two m-NLP probes⁴ to obtain an expression for the electron current that does not depend on the electron temperature. We could also take the current ratio to eliminate some parameters, and get an equation that is independent of the electron density. In any case, the direct measurement is an electric current to the probe, where for analysis ideal conditions are assumed, and one of these conditions is that the plasma is collisionless.

Most, if not all, scientific missions in space where Langmuir probes are used for measurements assume collisionless plasma conditions.^{1,9} For the most part, this assumption is likely valid. However, in the lower E-region of the ionosphere—at ~ 90 – 150 km—the collision frequencies between charged and neutral species are too high to call plasma in this region collisionless.^{10,11} Several missions, like the

SPIDER missions⁹ or the proposed orbital low flyer Daedalus,¹² have their focus on regimes with higher collision frequencies, where collisions are likely to impact the measurements in some way. In these cases, collisionless theories for the current collection of Langmuir probes must still be used since there is no collisional theory available. It is therefore assumed that the impact of collisions is small. However, this assumption is not trivial; there does not exist, to the best of our knowledge, any good source that would justify it, or would give a quantifiable method of correcting the currents collected by the Langmuir probes in collisional plasma. Interest in the complex and turbulent nature of the lower E-region is growing, due to radio echoes, signal degradation, and GPS scintillation.¹³ In addition, there are several unanswered fundamental questions of plasma and atmospheric physics that are linked to this region.^{14–16}

There have been some previous works on collisional effects on the currents collected by Langmuir probes.^{17,18} While these articles focus on the ion collection (the negative probe potential) regime, discussions of the physical processes are applicable also for electron–neutral collisions. In Ref. 17, the authors report an increased ion current in the low-pressure (low-collision frequency) limit; this is attributed to the destruction of ion orbits around the probe. In addition, in the highly collisional case the ion currents are lower, limited by diffusion and drift to the probe. This is similar to the empirical results in Ref. 18 where they also report a peak in the ion current in the OML range when $\lambda_i \sim$ the sheath thickness. In their results, the value of λ_D/λ_i where this peak occurs ranges from ~ 0.2 to 0.5 , meaning, there is a peak when λ_i is slightly longer than λ_D . However, some fundamental differences between electrons and ions means there will likely be significant differences between the charge–neutral collision effects on an ion or electron Langmuir probe current. One major difference is that for ion–neutral collisions, electrons usually act as a neutralizing/restoring background; this will not necessarily be the case for electron neutral-collisions.

Here, we will, for the first time, focus on the effects of electron–neutral collisions in the positive probe potential regime. The effects of ion collisions are in a sense more relevant than that of electron collisions because the mean free path is usually shorter for ions, giving it a wider range of applicability. However, experiments can easily be designed to circumvent the ion collisional effect by using probes that collect electron currents in the electron current regime where ion collisions can be neglected. This is where the need for an analysis of the electron collision effects arises. One possible reason explaining why this has not been done before is that simulating electron collisions is computationally more expensive, since we cannot treat the electrons as a fluid, as it is done in the studies of ion–neutral collision effects. We will here present the first fully 3D, kinetic simulations, of both electrons and ions, of a cylindrical Langmuir probe in the electron saturation regime, with a collisional electron sheath.

In this article, we will address both of the aforementioned issues using particle-in-cell (PIC) simulations. It is our intention that this article can be used as a reference to emphasize where the collisionless assumption holds. In addition, we will apply a method for building a function to correct collisional effects on the collected currents to a cylindrical Langmuir probe. We apply this method to the ICI-4 sounding rocket data to show an example of the effects of electron–neutral collisions through the whole E-region.

II. THE PIC SIMULATOR

This section reviews some important aspects of the new fully parallel 3D particle-in-cell (PIC) code PINC used in this study. There are three main classes of simulators employed for simulating plasma: PIC, fluid, and hybrid. A PIC simulator is well suited for studying kinetic effects and uses less assumptions as opposed to fluid or hybrid simulators. In particular, a fluid simulator solves the magnetohydrodynamic (MHD) equations, which assumes a Maxwellian form on the particle distribution. In hybrid simulators, a fluid treatment is usually performed on the electrons, and a PIC treatment is used for the ions. In a PIC simulator, we effectively solve the Vlasov equation using the method of characteristics, making no assumption on the particle distribution.¹⁹ In collisional plasma, we have no a priori knowledge of the particle distributions; thus, a fluid or hybrid simulator is not well suited for this task. In addition, a fourth kind of simulator has emerged in recent years called Vlasov simulators.²⁰ Vlasov simulators solve the Vlasov equation directly and thus include kinetic effects. However, the collisionless assumption is usually included in the design of the simulator and would need further development to include charge–neutral particle collisions. The need for a new code lies in the fact that most codes that see widespread usage make some assumption—like treating electrons as a fluid—or are only capable to 2D simulations. There do exist some modern codes that do most of what we need, with the exception of for example charge–neutral collisions, which we could have modified for our use. However, by developing our own code we gain a larger degree of control in the implementation.

A. Applied algorithms

PINC uses the standard PIC main cycle^{19,21,22} with the addition of object–plasma calculations using the conductive surface capacitance–matrix method^{22,23} and charge–neutral collisions using the null-collision Monte Carlo collision (MCC) scheme.^{21,24} Since particles exist in the space between grid nodes, on which the fields are defined, we need to translate between the particle positions and grid nodes. The interpolation between particles and field quantities on the grid is done with a first order weighting function, often referred to as Cloud-In-Cell (CIC). For each particle, its charge is weighted to the nearest grid nodes that define the cell in which that particle resides. This is done with a weighting function,²⁵ which weighs the particle by one minus its normalized distance to each of the nodes. Similarly, later the field quantities are superimposed at the particle position from each of the nodes by the same weighting function. We also use the so-called superparticles, meaning that each particle is to be considered a part of phase-space with a size in space equal to the grid cell volume, but a point in velocity. This gives the superparticles the ability to be rescaled to include several real particles and still allow for solving the same Vlasov equation.¹⁹

In PINC, we are interested in the electrostatic solution, neglecting any change in the magnetic field. However, a static magnetic field can still be included using the Boris algorithm.²⁶

On the edge of the total simulated domain, we have chosen to use Dirichlet-type boundaries. We set the electric potential to be zero on the outermost nodes of the simulated domain and inject particles with a Maxwellian distribution.

The collision module is implemented using the null-collision MCC method described in Ref. 24, with the exception of a linear approximation to the collision frequencies, a method similar to the

one in Ref. 11. In order to maintain the correct collision frequency in the bulk plasma, in addition to adding the feature that slower moving particles collide less often than faster moving ones, we calculate the constant value of the cross sections that maintain this collision frequency. To do this, we begin with the probability for particle p to collide within a time step^{24,25}

$$P_p = 1 - e^{-n_i(x)\sigma_T(\varepsilon)V_p(\varepsilon)}, \quad (2)$$

where n_i is the neutral density and V_p is the relative particle speed between the incident and target particle, with ε the particle energy. σ_T is the total collision cross section, which can be written as a sum of cross sections for each collision type i present. From this, we define an instantaneous collision frequency as follows:

$$\nu_{i,p} = n_i(x)\sigma_i(\varepsilon_p)V(\varepsilon_p), \quad (3)$$

where ν is the instantaneous collision frequency, at position x . In Eq. (3), the collision frequency $\nu_{i,p}$ can be considered as the instantaneous collision frequency of one particle, used to calculate that particle's probability to collide within a time step, using the neutral density at the particle and the particle's speed. If we average over the particle distribution using Eq. (3), and solve for the cross section, we get

$$\sigma_i = \frac{\bar{\nu}_i}{\bar{n}_i \bar{V}}, \quad (4)$$

where \bar{n}_i is the constant average neutral density and \bar{V} is the average speed of the particles, averaging over the particle distribution. We used here $\bar{\nu}_i$ to indicate that this is for the whole distribution, meaning that this is the actual collision frequency of the species. Although the cross sections σ_i are generally dependent on a single particle's energy, using the averages in this way now gives us a constant value at the average energy (temperature). Feeding this value back into Eq. (3) will also give an individual instantaneous collision frequency per particle but maintain the correct collision frequency when averaging over many particles. This gives us a model with a linear collision frequency in speed, i.e., $\nu \propto V$.

The collisional cross sections are complicated functions of energy in reality;²⁴ however, simplifications can be made by approximating the collision frequencies with a linear or squared function of the particle's speed.^{11,27} We generally assume that the linear approximation is well justified for relatively low-energy plasmas such as those found in the vicinity of the Earth. Assumptions on the form of the collision frequencies are a topic of ongoing discussion, see Ref. 11, Sec. IV.

Usually, elastic electron-neutral collisions lead to a loss in energy for the electron due to the large difference in mass between the electron and neutral atom.²⁴ However, in some of the highly collisional cases presented in this article, this loss in energy, or lowering of temperature, could possibly increase the Debye length so much that the simulation becomes susceptible to the finite grid instability.^{22,28} This is especially likely for the higher collisional cases (e.g., at least 6 and 7) because in cases 6 and 7 the particles will collide several hundreds of times before reaching the probe if they take the shortest path from the boundary. If this happened, it would be difficult to differentiate what part of the results were due to nonphysical numerical issues and what are actual physical results. We therefore use an energy conserving scheme, where we ensure that the energy before and after a collision is the same. This is done by storing the speed $|\vec{v}_p|$ of the electron p

undergoing a collision before the scattering is performed. In previous works, calculation of the scattered velocity \vec{v}_{scat} [see Ref. 24, Eq. (11)] is a unit vector, thus multiplying the particle speed before a collision with the scattered unit vector, i.e., $|\vec{v}_p| \cdot \vec{v}_{scat}$, will maintain the speed of the particle throughout the collision. Note that the collision frequency, i.e., probability to collide for a given particle is still energy (speed) dependent, so is the scattering angle.²⁴

One important thing to note is that the MCC method includes an error in the number of particles to collide. In order for a particle to have a small probability of having two or more collisions, e.g., $r < 0.01$ in a single time step, the probability P_p of a collision in one time step should be $P_p < 0.095$.²⁴ This adds a constraint on the time step dt used for simulations, which will dominate for high collision frequencies.

B. Verification of simulation setup

During the development of PINC, many verification tests have been run; most of these are elaborate and outside the scope of this article, and we will here present some selected tests that are designed to cover the bigger picture. A detailed discussion of these tests can be found in the master's thesis of Killie,²⁹ Brask,³⁰ Holta,³¹ and Nielsen.³²

In order to verify the correctness and accuracy of PINC, we ran a set of verification tests. They can generally be split into two groups. The first set is for object-plasma interactions. The second set is for charge-neutral collisions. For object-plasma interactions, we first run a special case to compare to the OML theory. The case is essentially the same as in Ref. 23, and we use the same representation of a sphere with a radius of two cells. The actual geometry used is shown in Fig. 1. In addition to the floating potential, we compare the current collected by a biased Langmuir probe with the theoretical value. The current I_p in the electron saturation region is given by Eq. (1), where we have $V_f = 0$ since we are simulating a probe without the spacecraft.

In the test case, we used a mass ratio of $m_i/m_e = 100$, a density of $n_e = n_i = 1 \times 10^9 \text{ m}^{-3}$, and a temperature of $T_e = T_i = 1000 \text{ K}$. For the floating potential test, we use a radius of $0.06\lambda_D$ in order to directly compare with Ref. 23. After running the simulation until it reaches a steady state, we get a floating potential of -0.1260 V , or $-1.46k_B T/e$, which is 3% of the theoretical value. When running the simulation again but with a bias of 2 V and again using a radius of $0.06\lambda_D$, we get a current of $4.310 \times 10^{-8} \text{ A}$ to the probe compared with the theoretical value given by Eq. (1), which is $4.102 \times 10^{-8} \text{ A}$. This gives a percentage difference of 5%. The differences in values we obtain

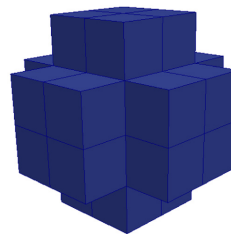


FIG. 1. Discretized geometry of a sphere used in the spherical OML test case.

from the simulator and theory might be explained by the ambiguity in the radius of the sphere. The sphere is approximated by numerical cells, which are in fact cubes.

An additional test was performed to verify the current collection. In this test, we use a slightly more complicated geometry for the probe, a cylinder which is longer than the Debye length and has a radius that is shorter than the Debye length. We then compare the collected current to an independent PIC code, PTetra.^{33,34} PTetra differs from PINC in one major way in that it uses nonuniform grid spacing. For verification, we used the collisionless case detailed in Sec. III and ran the simulation with the exact same probe geometry in PTetra and PINC. We ran the simulation both with a probe bias of 4.5 and 7.5 V. The steady state currents from PINC and from PTetra are shown in Table I. In this comparison between PINC and PTetra, we did not expect an exact agreement due to significant implementation differences between PINC and PTetra. Still, we obtain a difference of ~8%–9% in both cases, which we deem to be adequate for this case.

The most important test for verifying the correctness of the collisional module is that the number of colliding particles is consistent with the collision frequency. This is obtained from the probability for a particle to undergo a collision within a time step,^{24,25} given by

$$P_p = 1 - e^{-\nu_p \Delta t}, \tag{5}$$

where P_p is the probability for particle p to collide in time Δt , with collision frequency ν_p from Eq. (3). The number of colliding particles in a simulation per time step will then on average be

$$N_c = N_T \bar{P}, \tag{6}$$

where \bar{P} is the average probability, using the average collision frequency from Eq. (5). N_T is the total number of particles in the simulation. Note that with this definition, using probability, the number of colliding particles will change as the weighting of the superparticles changes, as it should. To verify that we collide the correct number of particles, we ran a simulation on an $8 \times 8 \times 8$ grid with 420 particles per cell. With a time step of $0.1\omega_{pe} = 1.77 \times 10^{-8}$ s and $\nu = 4 \times 10^5$ s⁻¹, we get $N_c = 758$ colliding particles per time step. The result was an average 769.7 collisions for electrons and 766.2 for ions. This test was run for a relatively short time, and we expect the numbers to get closer to N_c if we run the test longer; however, the largest error here is 1.5%, which is lower than other sources of error.

In addition to the collision frequency change, we checked that the change in energies and scattering angles due to a collision was consistent with the equations given in Ref. 24. In addition, to check that there was no systematic error in the scattering angles, we checked that the average of these was zero, i.e., angle has no preferred direction but is random.

TABLE I. Summary of parameters for the current collection test where we compare PINC to PTetra.

	PINC	PTetra
4.5 V	-4.59×10^{-6} A	-5.05×10^{-6} A
7.5 V	-6.95×10^{-6} A	-7.55×10^{-6} A

III. SIMULATION SETUP

In this section, we will go through the simulation setup used. The set consists of twelve simulations: six of them are run with a probe bias of 4.5 V and the other six are run with a probe bias of 7.5 V. We maintain the plasma parameters fixed with the exception of collision frequency, such that we isolate the effects of collisions on the two different biased probes. The parameters are based on EISCAT Svalbard Radar (ESR) data collected at 120 km altitude on 19 February 2015, at 22:00, at the launch of the ICI-4 sounding rocket, and are listed in the first panel in Table II. The values provided correspond to the mean quantities obtained from ESR UHF between 22:05:59 and 22:15:59 UT using 120 s integration time.

ICI-4 was launched from Andøya, Norway, in the nightside aurora and was in total darkness during the entire flight. The collision frequencies for both ions and electrons vary in power from 0 to 7. ICI-4 had four Langmuir probes biased at 3, 4.5, 6, and 7.5 V. Ideally, we would want to simulate all four probes; however, since we are somewhat limited by available computational resources we pick the 4.5 and 7.5 V probes. We are mostly interested in the electron collision frequencies as the collected currents are in the electron saturation region, and electron dynamics will be the dominating effect. In the E-region ionosphere, the dominant ion species are NO⁺ and O²⁺; however, in the simulations we use He⁴⁺. It is a common trick in PIC simulations, however, to reduce the ion mass. This is because otherwise, the ion dynamics gets so slow that they incur a high computational cost—and by increasing the time steps needed—and, therefore, the computational time needed to reach steady state. Reducing the ion mass will in turn increase the ion current. However, in the electron saturation region, the ion current is nonetheless negligible compared to the electron

TABLE II. Input parameters to the PIC simulator. The simulation parameters are based on observational data from ESR and NRLMSISE-00 Model 2001. The plasma parameters come from ESR and neutral densities and temperatures used for calculating collision frequencies come from NRLMSISE. The simulation ID is assigned from the power of the electron collision frequency ν_e .

Parameters	Value
dx, dy, dz (m)	0.002
dt (s)	5×10^{-10}
Time steps	100 000
Density (e, i) (m ⁻³)	9.597×10^{10}
T_e (K)	441
T_i (K)	475
m_e (kg)	9.109×10^{-31}
m_i (kg)	6.646×10^{-27}

Simulation ID	ν_i	ν_e
0	0	0
2	8.737×10^2	2.911×10^2
3	8.737×10^3	2.911×10^3
4	8.737×10^4	2.911×10^4
5	8.737×10^5	2.911×10^5
6	8.737×10^6	2.911×10^6
7	8.737×10^7	2.911×10^7

current. In addition, there is no collisional coupling between electrons and ions. The reduced mass therefore should not affect our results.

For comparison, we chose a probe geometry that mimics the probes from ICI-4. The exact geometry can make a difference, and we are simulating a probe with length $\sim 5\lambda_D$ such that the probe current likely is impacted by the finite length effect³⁵ and the fact that the probe is actually mounted on a guard, not included in the simulations. In the following analysis, we assume that such effects do not depend on the collision frequency such that when we take the ratio of two currents, effects like the finite length effect will disappear. Due to the uniform grid employed in PINC, our simulated “cylindrical” probe is actually a rectangular box with size $1 \times 1 \times 12$ cells, that is $0.002 \times 0.002 \times 0.024 \text{ m}^3$. We also use a simulated domain of $128 \times 128 \times 128$ cells, which is $0.256 \times 0.256 \times 0.256 \text{ m}^3$. That gives each side of the domain a length of 54.8 Debye lengths.

In Table III, we have listed some derived parameters for the simulations, in particular the dimensionless parameter mean free path (λ_e)/Debye length (λ_D). To calculate λ_e , we use the definition

$$\lambda_e \equiv \frac{\text{particle speed}}{e - n \text{ collision frequency}} = \frac{v_{th,e}}{\nu_e}. \quad (7)$$

Here, $v_{th,e}$ is the electron thermal speed and ν_e is the electron-neutral collision frequency. In the remainder of this article, it is therefore understood that when we talk about the mean free path it is the electron mean free path λ_e .

The usual assumption on collisionless conditions is stated as $\omega_{pe}/\nu_e \gg 1$, where ω_{pe} is the electron plasma frequency. This inequality leads to the equation

$$\frac{\lambda_e}{\lambda_D} = \frac{v_{th,e}/\nu_e}{v_{th,e}/\omega_{pe}} = \frac{\omega_{pe}}{\nu_e} \gg 1. \quad (8)$$

So, both the dimensionless parameters, λ_e/λ_D and ω_{pe}/ν_e , can be used interchangeably; but we will use the parameter λ_e/λ_D as a measure of the collisionality in plasma.

In order to calculate the collision frequencies between the plasma particles and neutral particles, we used the equations given in Ref. 36 and the data for neutral temperatures and densities from NRLMSISE-00 Model 2001.^{37,38} The NRLMSISE model is an empirical model based on several sources of data, used to calculate the neutral density and temperature in Earth’s atmosphere. NRL stands for the US Naval Research Laboratory. MSIS stands for mass spectrometer and

TABLE III. Derived parameters for Table II.

Parameters	Value
ω_{pe} (rad/s)	1.75×10^7
λ_{de} (m)	0.004 678
λ_{e0}/λ_D	∞
λ_{e2}/λ_D	60 038
λ_{e3}/λ_D	6003.8
λ_{e4}/λ_D	600.38
λ_{e5}/λ_D	60.038
λ_{e6}/λ_D	6.0038
λ_{e7}/λ_D	0.6004

incoherent scatter radar, which was the source of data in the original form of the model. Later versions also include satellite drag data. The last E stands for exosphere, indicating that the model extends through the whole exosphere of the Earth.

IV. RESULTS

The results of the simulations are divided into three subsections. First, we provide general results of the current collected at two different bias values of the Langmuir probe, where the only varied parameter is λ_e/λ_D . Second, we carry out an additional test to study the dependence of the current on the plasma parameters at a fixed value of λ_e/λ_D . Third, we quantify the simulation results with a least squares regression to a well-behaved function.

A. Simulation results

In this section, we present results from the simulations described in Sec. III.

Figure 2 shows plots of the electron densities perpendicular to the probe and through the short side in the center of the probe. The vertical black dotted line represents the probe surface. In the figure, we added one plot from each simulation from the 4.5 V bias cases, such that each plot represents a collision frequency, or equivalently a value of λ_e/λ_D . We chose to omit including a figure for the 7.5 V case as it shows similar density profiles, only with the exception of higher peak density values.

As expected, when the collision frequencies increase, the peak electron density in the probe sheath gets lowered. However, there is one exception, from simulation 2 we see a small increase in the peak density. Noting that this increase is small enough to be within simulation error, it might indicate a higher trapping rate for the electrons, similar to the processes described in Refs. 17 and 18, but for electrons instead of ions. For relatively low collision frequencies, the electron-neutral collisions transfer radial momentum to angular momentum, trapping the electrons in orbit. This happens at a higher rate than the

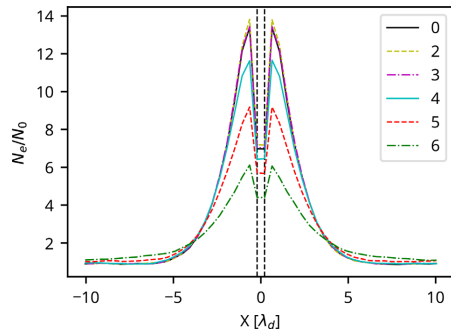


FIG. 2. Lineplots across the middle of the probe traversing the short side. The plot shows the electron densities. Density values are normalized by N_0 , the ambient background density of the electrons, and length is given in Debye lengths. Densities are averaged over the last 1000 time steps. The plot shows only the contribution from particles, omitting the contribution from surface charges on the probe.

opposite effect, where the colliding electron orbits are destroyed and the electrons fall toward the probe. For the rest of the simulations, the latter effect seems to be dominating, the high rate of electrons getting pushed out of orbit is effectively lowering the density close to the probe. The presheath, at $\sim \pm 5-10\lambda_D$ has the opposite behavior, with lower values for lower collision frequencies, and higher densities as the collision frequencies rise.

The development of the currents to the simulated probe in time is presented in Fig. 3. Comparing the 4.5 V (a) cases to the 7.5 V (b) cases, we see that the overall behavior between these is the same. For the cases up to case 6, that is, for all cases where $\lambda_e/\lambda_D > 1$, the currents stabilize at higher values as the collision frequencies rise and λ_e gets lower. The development of the transient in the current slows down and stabilizes at an enhanced value, compared to the collisionless case. The reason

for higher current values is the same as that for the lower densities seen in Fig. 2—as the collision frequency rises, more particles are knocked out of orbit and get collected by the probe.

The impact of varying the electron-neutral collision frequency on the collected current can be seen in Fig. 4. In Fig. 4(a), the currents are normalized, with I_0 being the zero collision frequency (collisionless) current obtained from simulations. The black dotted line indicates a 10% change with respect to the collisionless case. The current ratio, see Fig. 4(b), is the ratio of the currents at a bias value of 7.5 V to the 4.5 V simulations at different values of λ_e/λ_D .

The importance of current ratios is to visualize the difference in the impact of collisions for the two different probes. If the variation in collision frequency impacts probes at different potentials equally, the

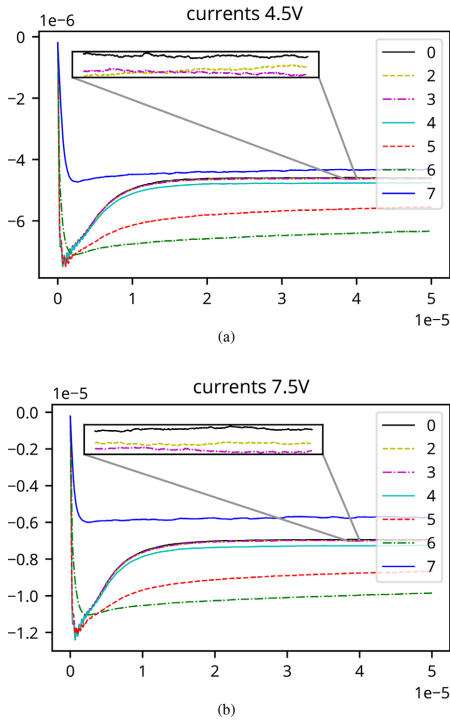


FIG. 3. Development of the currents to the simulated probe at 4.5 V cases (a) and 7.5 V cases (b). The numbers 7, 6, 5, 4, 3, 2, and 0 refer to the order of magnitude of the electron collision frequency. Values are given in SI units. Both plots include a $10\times$ zoomed-in area to show the differences in cases 0, 2, and 3. In order to remove noise, an exponential moving average filter using a relaxation time of ten time steps was applied. (Associated dataset available at <https://doi.org/10.5281/zenodo.5906749>) (Ref. 39).

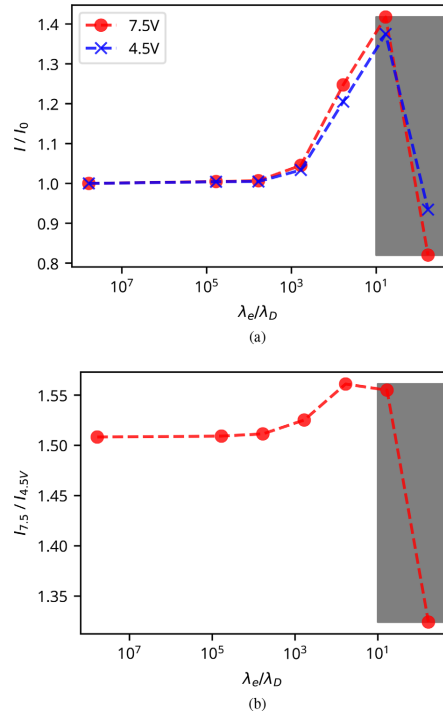


FIG. 4. Comparison of single currents (a) and current ratios (b) for case with fixed plasma parameters, but with varying collision frequency. Currents are collected at two different positive bias values: 4.5 and 7.5 V. All values are averaged over the last 500 time steps. The gray area shows where the mean free path has the same order of magnitude as the Debye length. The zero collision, infinitely long mean free path case 0 is represented by the number 6×10^1 . (Associated dataset available at <https://doi.org/10.5281/zenodo.5906749>) (Ref. 39).

15 September 2023 09:45:55

plotted line in Fig. 4(b) should be straight. Taking the ratio of two probes *a* and *b* using Eq. (1), we get

$$I_a/I_b = \frac{\left(1 + \frac{q(V_a + V_f)}{k_B T_e}\right)^\beta}{\left(1 + \frac{q(V_b + V_f)}{k_B T_e}\right)^\beta}, \tag{9}$$

which is independent of density and constant for constant values of floating potential V_f , electron temperature T_e , and probe geometry β . In these simulations, we control V_f and T_e , and maintain them as constants, so the changes must be explained either with β which is possible since the probe has a finite length³⁵ or as a purely collisional effect.

In both plots in Fig. 4, the x axis is log scaled using a base 10 logarithm. From the normalized currents, we see that the currents increase with increasing collision frequency (lower λ_e) for cases where $\lambda_e/\lambda_D > 1$. In addition, the curve seems to follow an exponential increase, at least for the first five points. This exponential increase suggests that the change in currents linearly depends on λ_e/λ_D due to the log scaled x axis. We will test this dependency in Secs. IV B and IV C. For the current ratios, we observe a similar increase—suggesting that the collisions impact the two different bias values differently. However, the percentage change is small and might therefore be negligible for the present setup. We do not know if this change will be larger for other setups. It might also impact some analysis methods to a larger degree, if one takes for example the difference of the squared currents. In any case, we will include most of these differences in the correction later.

For the case 7 current value, it is likely true that it will be lower than at least the case 6 currents, based on the observations from Fig. 3. Currently, we do not know if this value can be trusted, as it is likely that when $\lambda_e/\lambda_D < 1$ the plasma dynamics are no longer dominated by electromagnetic forces. Although this in itself should not invalidate the simulations, this point should be analyzed with care. In addition, we highlighted the area where the mean free path has the same order of magnitude as the Debye length in gray as an area of concern, which needs additional analysis and verification in the future. However, the trend makes physical sense as electrical resistance will dominate at these higher collision frequencies. It is also consistent with a similar process for ions.¹⁸ The point is added for consistency with the previous plots, and future reference.

B. Dependence on plasma parameters with fixed λ_e/λ_D

As we saw in Fig. 4, there is a dependence of the collected current on the parameter λ_e/λ_D . However, it might seem unclear if there are additional dependencies on plasma parameters. In order to answer this question, we set up an additional test. We modify two additional simulated parameters, starting with the setup in Table II; for the first additional case, we increase the temperature by an order of magnitude, and for the second we increase the temperature by a factor of 10 and the density by a factor of 5. In each case, we maintain the parameter $\lambda_e/\lambda_D = 60$ by varying the electron collision frequency. In addition, we rescale the simulation grid to maintain the probe size with respect to λ_D . The idea is that if we change the plasma parameters, but maintain all the dimensionless parameters at constant values, if there is no dependence on other parameters, we should get the same value in each case for I/I_0 , the ratio of collisionless current to the collisional

current. To this end, we also need to rescale the probe bias. To do this, we use the dimensionless potential

$$\eta = \frac{qV_p}{k_B T_e}. \tag{10}$$

In this case, we get a value of $\eta \approx 118$; for both of the new cases to maintain a constant η , we need to increase the bias by an order of magnitude since the temperature increases by an order.

From Table IV, we see that the value of I/I_0 can be considered constant as the differences are small enough to be associated with the simulation errors, such as the finite grid, finite time step, and limited simulation box. For these values, the mean is 1.2216 with a small standard deviation of 0.0095; this small standard deviation supports the fact that normalized currents are dependent only on the dimensionless parameter λ_e/λ_D at a constant η . It is important to note that since η is temperature dependent, realistically, in a rocket mission as temperature and floating potential of the spacecraft changes, η will also change.

C. Quantifying the changes in currents

As mentioned previously, the currents in Fig. 3 seem to follow an exponential curve. We will in this subsection show how we can use these results from the simulations to fit a suitable exponential function to the data points. This function will then give a quantifiable method for correcting the collected currents, which could be used in post-processed/corrected L2 data products for sounding rocket missions or low flying orbiters.

There are several candidate functions we can fit to. We chose one that will be suited for the low to medium collisional range, as this will be usable for most cases in space plasmas. If we were to include higher collision frequencies, this function would need a more complex form. To this end, we use only the five lowest collision frequency points. The function we chose is of the form

$$I/I_0 = 1 + \gamma_{corr} = 1 + 10^{A+Bx}, \tag{11}$$

where I is the collected current and I_0 is the zero collision current. I_0 can be any successful theoretical or measured collisionless current; for example, we may use the OML value of the current for I_0 , then I is the collisionally corrected OML current. γ_{corr} is a correctional term, in this case an exponential $\gamma_{corr} = 10^{A+Bx}$. The variable x is the (\log_{10}) value of λ_e/λ_D . γ_{corr} could have been the natural exponential, this would just change the coefficients A and B . We chose to use base 10 for consistency with the simulations and plots.

We perform a least squares regression where we minimize the residual sum of squares defined as $RSS = \sum_i (y_i - \bar{y}_i)^2$. Here, y_i are the values from the simulations and \bar{y}_i are the values we get from Eq. (11) at the same values of $x = \log_{10} \lambda_e/\lambda_D$.

In order to evaluate the quality of the fit, we use the coefficient of determination called “R square” value, defined as $R^2 = 1 - RSS/TSS$,

TABLE IV. Normalized current values for three cases with different plasma parameters, but fixed λ_e/λ_D .

	Original	Added case 1	Added case 2
I/I_0	1.212	1.222	1.231

15 September 2023 09:45:55

TABLE V. Table of coefficients, and their residual sum of squares from the fit of Eq. (11) to the simulation data.

	<i>A</i>	<i>B</i>	<i>R</i> ²
4.5 V	0.76	−0.81	0.999 81
7.5 V	0.72	−0.74	0.999 76

where $TSS = \sum_i (y_i - \bar{y})^2$ and is the total sum of squares. Generally, a higher value of *R* squared indicates that the fit is better, and if $R^2 = 1$ the model perfectly describes the data. As we see from the values of R^2 in Table V, the fit we obtain is good. Since the parameters are found using a setup applicable to the launch of the ICI-4 sounding rocket, using these in Eq. (11), this gives us a correction due to collisions that we can apply to the ICI-4 data for the 4.5 and 7.5 V probes. As mentioned above, the values obtained for the coefficients *A* and *B* are based on simulations using an energy-conserving scheme for the electron–neutral collisions. It should be noted that this assumption might be nontrivial, and the inclusion of energy-loss during the electron–neutral collisions will likely further enhance the collected current, which would change these coefficients to some degree.

Finally, we can apply this fitted function to the ICI-4 Langmuir probe data. In addition, we need λ_D and λ_e . The plasma temperature and density are again obtained using ESR data with a resolution of 5 km in the vertical direction and the neutrals’ (N_2 , O, and O_2) temperature and density are obtained with NRLMISE-00 Model 2001,^{37,38} and λ_e is calculated using collision frequencies from Ref. 36. From this, we get a value of λ_e/λ_D at each 5 km, values are interpolated between the 5 km resolution in Fig. 5(b). Note also that this calculated λ_D is not accurate within these 5 km; however, this should not make a large impact since it is the order of magnitude that is important.

The result of the collisional correction is shown in Fig. 5(a). Both the original uncorrected current *I* and the corrected *I*₀ probe current are plotted. A bandpass filtering was performed on the uncorrected current to remove the spin from the payload and the first three harmonics. The bandpass filtering is then effectively also applied to the

corrected current through the uncorrected current. In Fig. 5(b), the ratio of these is plotted in a similar manner as in Fig. 4. From the *I*/*I*₀ ratio, we see that the corrections are small above 120 km and negligible above 160 km. For ICI-4, if high accuracy in the currents is required, then it will be important to use collisional corrections on data up to ~160 km, and under 120 km collisional corrections should always be used. It is reasonable to assume that similar heights will be of importance for other missions.

V. CONCLUSIONS AND FUTURE PERSPECTIVES

The results of the simulations indicate that the effect of electron–neutral collisions on an electric current collected by a cylindrical Langmuir probe, biased in the electron saturation regime, generally leads to an enhancement in the collected current when $\lambda_e/\lambda_D \rightarrow 1$. With the simulation results, we could fit a function to the simulation results for the probes biased at 4.5 and 7.5 V for plasma parameters relevant for ionospheric conditions. These two functions were consistent with the simulations at ionospheric altitudes down to 100 km, at which point additional simulations and a non-linear function for the exponent of γ_{corr} would be needed. This method of using simulation results for correcting experimental data is general, and it can be deployed on a per-mission basis. We expect that the values we obtained and used in Eq. (11) should hold for ionospheric conditions similar to the ICI-4 sounding rocket mission presented here. However, at present we feel that additional simulations should be run in other missions to verify or obtain new parameters. In addition, since the model presented here for ICI-4 is not verified outside of simulations, experimental verification should be done in the future.

It may be possible to extract plasma parameters omitting the collisional effects by taking, e.g., the ratio of two probes. If the collisions impact the probes at the same rate, the collisional effect should disappear. However, we see some evidence that this is not the case for higher collision frequencies in Fig. 4(b). More precisely, as long as the dependence on the dimensionless collision parameter λ_e/λ_D does not change with varying η , i.e., the term γ_{corr} in Eq. (11) appears to depend weakly on η . In the present study, the η dependence will be included in Eq. (11) as long as the linear assumption holds, which in this case is

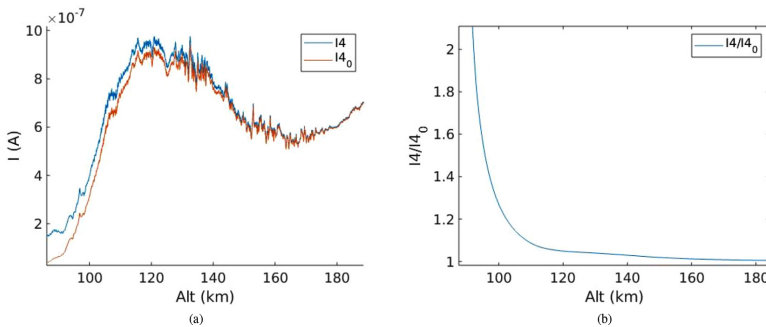


FIG. 5. (a) Real filtered current (*I*) for ICI-4 sounding rocket, and its collisionally corrected (*I*₀) current for the 4.5V biased probe. Figure (b) shows the ratio of real (*I*) to corrected (*I*₀) currents. Plots show only the relevant range of the upleg flight in the range 85–185 km. (Associated dataset available at <https://doi.org/10.5281/zenodo.5647637>) (Ref. 40).

15 September 2023 09:45:55

down to ~ 100 km from comparing Figs. 5(b) and 4(a). However, when a linear equation [exponent of γ_{corr} in Eq. (11)] does not hold, a nonlinear dependence on the collisional parameter λ_e/λ_D and possibly dimensionless probe voltage η seems to be present. A focused study on these effects is therefore important to perform in the future.

In addition, a function that includes the very highly collisional currents, where $\lambda_e/\lambda_D \lesssim 1$, is favorable. This area is of less practical interest, but it would nevertheless be instructive to include it in a generalized function. We would also like to do a study on the kinetic effects, i.e., how the electron distribution close to the probe changes in phase-space in the medium-to-high collisional range with respect to the collisionless case. We expect that there will be some differences, and that these will help to explain the mechanism of the enhanced collisional currents.

The results presented here should be relevant for any data analysis done on Langmuir probe currents from a collisional plasma in the electron saturation region. It is especially important to track the parameter λ_e/λ_D and know the limits of when collisionless theory is valid. This applies to both previous and future missions in the E-region, in addition to special cases like complex plasmas in a cometary tail or outgassing from a planet or moon, where neutral densities can be relatively high. It is our hope that this article will highlight the importance of a special treatment needed for such cases.

ACKNOWLEDGMENTS

This work received funding from the European Research Council (ERC) under the European Union's Horizon 2020 research and innovation program (Grant Agreement No. 866357, POLAR-4DSpace). This research is a part of the 4DSpace Strategic Research Initiative at the University of Oslo. This study is supported in part by the Research Council of Norway Grant No. 275653. T. Takahashi was supported by JSPS Overseas Research Fellowships and KAKENHI Grant No. JP20K14544.

We gratefully acknowledge Gullik Killie, Vigdis Holta, Trym Erik Nielsen, and Jan Decca, who took part in the development of PINC, along with Steffen Brask and Sigvald Marholm. We also wish to thank Richard Marchand, who provided PTetra for Sigvald Marholm to use.

We thank the staff of EISCAT for operating the facility and supplying the data. EISCAT is an international association supported by research organisations in China (CRIRP), Finland (SA), Japan (NIPR and ISEE), Norway (NFR), Sweden (VR), and the United Kingdom (UKRI). In this work, we used NRLMISE-00, which was developed by Picone *et al.*³⁷ and is available at <https://cmc.gsfc.nasa.gov/modelweb/models/nrlmisse00.php>.

AUTHOR DECLARATIONS

Conflict of Interest

The authors have no conflicts to disclose.

DATA AVAILABILITY

The data that support the findings of this study are openly available in Zenodo at <http://doi.org/10.5281/zenodo.5906749>, Ref. 39. The ICI-4 data are available in Zenodo at <https://doi.org/10.5281/zenodo.5647637>, Ref. 40. All simulations can be reproduced using PINC 0.2.0 available at <https://github.com/pincproject>.

REFERENCES

- 1A. I. Eriksson, R. Boström, R. Gill, L. Åhlén, S.-E. Jansson, J.-E. Wahlund, M. André, A. Mälkki, J. A. Hollet, B. Lybekk, A. Pedersen, L. G. Blomberg, and LAP Team, "RPC-LAP: The Rosetta Langmuir probe instrument," *Space Sci. Rev.* **128**, 729–744 (2007).
- 2B. Holback, S. E. Jansson, L. Åhlén, G. Lundgren, L. Lyngdal, S. Powell, and A. Meyer, "The Freja wave and plasma density experiment," *Space Sci. Rev.* **70**, 577–592 (1994).
- 3G. Gustafsson, R. Boström, B. Holback, G. Holmgren, A. Lundgren, K. Stasiewicz, L. Åhlén, F. S. Mozer, D. Pankow, P. Harvey, P. Berg, R. Ulrich, A. Pedersen, R. Schmidt, A. Butler, A. W. C. Fransen, D. Klinge, M. Thomsen, C.-G. Fälthammar, P.-A. Lindqvist, S. Christensen, J. Hollet, B. Lybekk, T. A. Sten, P. Tanskanen, K. Lappalainen, and J. Wygant, "The electric field and wave experiment for the cluster mission," *Space Sci. Rev.* **79**, 137–156 (1997).
- 4K. S. Jacobsen, A. Pedersen, J. I. Moen, and T. A. Bekkeng, "A new Langmuir probe concept for rapid sampling of space plasma electron density," *Meas. Sci. Technol.* **21**, 085902 (2010).
- 5T. A. Bekkeng, K. S. Jacobsen, J. K. Bekkeng, A. Pedersen, T. Lindem, J.-P. Lebreton, and J. I. Moen, "Design of a multi-needle Langmuir probe system," *Meas. Sci. Technol.* **21**, 085903 (2010).
- 6H. Hoang, K. Roed, T. A. Bekkeng, J. I. Moen, A. Spicher, L. B. N. Clausen, W. J. Miloch, E. Trondsen, and A. Pedersen, "A study of data analysis techniques for the multi-needle Langmuir probe," *Meas. Sci. Technol.* **29**, 065906 (2018).
- 7H. Hoang, L. B. N. Clausen, K. Roed, T. A. Bekkeng, E. Trondsen, B. Lybekk, H. Strøm, D. M. Bang-Hauge, A. Pedersen, A. Spicher, and J. I. Moen, "The multi-needle Langmuir probe system on board NorSat-1," *Space Sci. Rev.* **214**, 75 (2018).
- 8H. M. Mott-Smith and I. Langmuir, "The theory of collectors in gaseous discharges," *Phys. Rev.* **28**, 727–763 (1926).
- 9G. Giono, N. Ivchenko, T. Sergienko, and U. Brändström, "Multi-point measurements of the plasma properties inside an Aurora from the SPIDER sounding rocket," *J. Geophys. Res.* **126**, e2021JA029204, <https://doi.org/10.1029/2021JA029204> (2021).
- 10D. T. Farley, "The equatorial E-region and its plasma instabilities: A tutorial," *Ann. Geophys.* **27**, 1509–1520 (2009).
- 11M. M. Oppenheim and Y. S. Dimant, "Kinetic simulations of 3-D Farley-Buneman turbulence and anomalous electron heating," *J. Geophys. Res.* **118**, 1306–1318, <https://doi.org/10.1002/jgra.50196> (2013).
- 12T. E. Sarris, E. R. Talaat, M. Palmroth, I. Dandouras, E. Armandillo, G. Kervalishvili, S. Buchert, S. Tourgaidis, D. M. Malaspina, A. N. Jaynes, N. Paschalidis, J. Sample, J. Halekas, E. Doornbos, V. Lappas, T. Moretto Jørgensen, C. Stolle, M. Clilverd, Q. Wu, I. Sandberg, P. Pirnaris, and A. Aikio, "Daedalus: A low-flying spacecraft for in situ exploration of the lower thermosphere-ionosphere," *Geosci. Instrum. Methods Data Syst.* **9**, 153–191 (2020).
- 13P. M. Kintner, B. M. Ledvina, and E. R. de Paula, "GPS and ionospheric scintillations," *Space Weather* **5**, 000260, <https://doi.org/10.1029/2006SW000260> (2007).
- 14A. Gurevich, *Nonlinear Phenomena in the Ionosphere, Physics and Chemistry in Space* (Springer-Verlag, Berlin Heidelberg, 1978).
- 15Y. S. Dimant and M. M. Oppenheim, "Ion thermal effects on E-region instabilities: Linear theory," *J. Atmos. Sol.-Terr. Phys.* **66**, 1639–1654 (2004).
- 16M. Palmroth, M. Grandin, T. Sarris, E. Doornbos, S. Tourgaidis, A. Aikio, S. Buchert, M. A. Clilverd, I. Dandouras, R. Heelis, A. Hoffmann, N. Ivchenko, G. Kervalishvili, D. J. Knudsen, A. Kotova, H.-L. Liu, D. M. Malaspina, G. March, A. Marchaudon, O. Marghitu, T. Matsuo, W. J. Miloch, T. Moretto-Jørgensen, D. Mpaloukidis, N. Olsen, K. Papadakis, R. Pfaff, P. Pirnaris, C. Siemes, C. Stolle, J. Suni, J. van den IJssel, P. T. Verroenen, P. Visser, and M. Yamauchi, "Lower-thermosphere-ionosphere (LTI) quantities: Current status of measuring techniques and models," *Ann. Geophys.* **39**, 189–237 (2021).
- 17F. Taccogna, S. Longo, and M. Capitelli, "Ion-neutral collision effects in Langmuir probe theory," *Contrib. Plasma Phys.* **48**, 509–514 (2008).
- 18Z. Zakrzewski and T. Kopiczynski, "Effect of collisions on positive ion collection by a cylindrical Langmuir probe," *Plasma Phys.* **16**, 1195–1198 (1974).
- 19G. Lapenta, "Particle simulations of space weather," *J. Comput. Phys.* **231**, 795–821 (2012).

- ²⁰C. Cui and J. Wang, "Grid-based Vlasov simulation of collisionless plasma expansion," *Phys. Plasmas* **28**, 093510 (2021).
- ²¹C. Birdsall, "Particle-in-cell charged-particle simulations, plus Monte Carlo collisions with neutral atoms, PIC-MCC," *IEEE Trans. Plasma Science* **19**, 65–85 (1991).
- ²²R. W. Hockney and J. W. Eastwood, *Computer Simulation Using Particles* (CRC Press, 1988).
- ²³Y. Miyake and H. Usui, "New electromagnetic particle simulation code for the analysis of spacecraft-plasma interactions," *Phys. Plasmas* **16**, 062904 (2009).
- ²⁴V. Vahedi and M. Surendra, "A Monte Carlo collision model for the particle-in-cell method: Applications to argon and oxygen discharges," *Comput. Phys. Commun. Part. Simul. Methods* **87**, 179–198 (1995).
- ²⁵J. P. Verboncoeur, "Particle simulation of plasmas: Review and advances," *Plasma Phys. Controlled Fusion* **47**, A231–A260 (2005).
- ²⁶H. Qin, S. Zhang, J. Xiao, J. Liu, Y. Sun, and W. M. Tang, "Why is Boris algorithm so good?," *Phys. Plasmas* **20**, 084503 (2013).
- ²⁷M. M. Oppenheim and Y. S. Dimant, "Ion thermal effects on E-region instabilities: 2D kinetic simulations," *J. Atmos. Sol.-Terr. Phys.* **66**, 1655–1668 (2004).
- ²⁸C. K. Birdsall and A. B. Langdon, *Plasma Physics via Computer Simulation* (McGraw-Hill, 1985).
- ²⁹G. V. Kilic, "A parallel multigrid Poisson solver for PINC, a new particle-in-cell model," Ph.D. thesis (University of Oslo, 2016).
- ³⁰S. M. Brask, "Instabilities in collisional plasmas studied by means of 3D kinetic particle-in-cell simulations," Ph.D. thesis (University of Oslo, 2018).
- ³¹V. Holta, "Dynamics of a plasma blob studied with particle-in-cell simulations," Ph.D. thesis (University of Oslo, 2018).
- ³²T. E. Nielsen, "Photoemissive charging of the mercury magnetospheric orbiter studied by means of 3D particle-in-cell simulations," Ph.D. thesis (University of Oslo, 2020).
- ³³R. Marchand, "PTetra, a tool to simulate low orbit satellite-plasma interaction," *IEEE Trans. Plasma Sci.* **40**, 217–229 (2012).
- ³⁴R. Marchand and P. A. Resendiz Lira, "Kinetic simulation of spacecraft-environment interaction," *IEEE Trans. Plasma Sci.* **45**, 535–554 (2017).
- ³⁵S. Marholm and R. Marchand, "Finite-length effects on cylindrical Langmuir probes," *Phys. Rev. Res.* **2**, 023016 (2020).
- ³⁶A. Brekke and J. Moen, "Observations of high latitude ionospheric conductances," *J. Atmos. Terr.* **55**, 1493–1512 (1993).
- ³⁷J. M. Picone, A. E. Hedin, D. P. Drob, and A. C. Aikin, "NRLMSISE-00 empirical model of the atmosphere: Statistical comparisons and scientific issues," *J. Geophys. Res.* **107**, SIA 15-1–SIA 15-16, <https://doi.org/10.1029/2002JA009430> (2002).
- ³⁸D. Bilitza, "International reference ionosphere 2000," *Radio Sci.* **36**, 261–275, <https://doi.org/10.1029/2000RS002432> (2001).
- ³⁹S. M. Brask and S. Marholm (2021). "Ici-4 e-n collisional current simulations," *Zenodo*, V. 2.1, Dataset <https://doi.org/10.5281/zenodo.5906749>.
- ⁴⁰A. Spicher, S. M. Brask, and W. J. Miloch (2021). "Multi-needle langmuir probe (mNLP) data on the investigation of Cusp irregularities (ICI) 4 sounding rocket," *Zenodo*, V. 2.1, Dataset <https://doi.org/10.5281/zenodo.5647637>.

Paper II

Effects of Guard and Boom on Needle Langmuir Probes Studied with Particle in Cell Simulations

S. M. Brask, S. Marholm, W.J. Miloch, R. Marchand

Accepted for publication in *Journal of Plasma Physics*



Effects of Guard and Boom on Needle Langmuir Probes Studied with Particle in Cell Simulations

S. M. Brask^{1†}, S. Marholm^{1,2}, W.J. Miloch^{1‡}, and R. Marchand^{3¶}

¹Department of Physics, University of Oslo, Oslo, Norway

²Department of Computational Materials Processing, Institute for Energy Technology, Kjeller, Norway

³Department of Physics, University of Alberta, Edmonton, AB, Canada

(Received xx; revised xx; accepted xx)

We investigate the effects of different guard geometries on the currents to the needle type Langmuir probes. The results are based on Particle-in-Cell numerical simulations. We show that if the guard length is less than 6–8 Debye lengths there can be a significant impact on the currents to the probe. A guard radius should not be larger than the Debye length, otherwise it can also significantly impact the currents. However, since guard radii are often close to the probe radius, the second condition is usually satisfied.

1. Introduction

Current-voltage (I-V) characteristics of electrically conducting surfaces in isotropic plasmas were first discussed by Irvin Langmuir Mott-Smith & Langmuir (1926) with the so-called orbital motion limited theory (OML). Derivations for ideal planar, spherical, and cylindrical electric probes in plasma were done, and such probes are nowadays collectively referred to as Langmuir probes. The Langmuir probe theory was later refined by Laframboise (1966) with such additions as for example a finite radius of the probe. In space and ionospheric plasma experiments, both spherical and cylindrical probes are commonly used. Langmuir probes have seen a widespread usage both outside the ionosphere, with e.g., the Rosetta mission, and inside the ionosphere with orbital missions such as Freya, Swarm, Cluster, and Norsat-1 (Eriksson *et al.* 2007; Holback *et al.* 1994; Buchert *et al.* 2014; Gustafsson *et al.* 1997; Hoang *et al.* 2018). In addition, Langmuir probes have been deployed in many sub-orbital sounding rocket missions, such as the ICI 1,2,4 rockets or the ECOMA campaign (Jacobsen *et al.* 2010; Bekkeng *et al.* 2010, 2013). The Debye length in the ionosphere ranges from a fraction of a millimeter to centimeters, and it is difficult to manufacture such a small spherical probe that will fulfill the OML assumptions and will collect currents with acceptable signal to noise levels. Thus, cylindrical probes with very small radii are often used. Such small cylindrical probes are often called needle type probes (Hoang *et al.* 2018).

When a Langmuir probe has a high enough bias voltage, it will collect only charges of a single (opposite) sign. This regime of the probe bias is called saturation. In the ionosphere and space plasma, for a sufficiently high positive bias voltage, only electrons will be collected. Note that if there are different ion species, including negative ions, they will also contribute to the currents in the electron saturation regime. However, in the

† Email address for correspondence: s.m.brask@fys.uio.no

‡ Email address for correspondence: w.j.miloch@fys.uio.no

¶ Email address for correspondence: rmarchan@ualberta.ca

following we consider probes at a high positive bias, and consider only electrons to be collected in this regime, which is the usual condition in the ionosphere.

For a cylindrical Langmuir probe p in the saturation regime at a voltage V with respect to the background, the collected current due to species α is approximately given by Laframboise (1966)

$$I_{p,\alpha} = I_{th,\alpha} K \left(1 + \frac{q_\alpha V}{k_B T_\alpha} \right)^\beta, \quad (1.1)$$

where k_B, q_α, T_α are the Boltzmann constant and the charge and temperature of the species, respectively. K is a constant depending on the probe shape with $K = 2/\sqrt{\pi}$ for a cylindrical probe. $I_{th,\alpha} = n_\alpha q S \sqrt{\frac{k_B T_\alpha}{2\pi m_\alpha}}$ is the thermal current due to random particle motion through a surface S if the surface and plasma are at the same electric potential. n_α, m_α are the species' number density and mass.

Several assumptions are made in the OML theory for the derivation of equation (1.1), such as the probe being very long, and the probe radius being very small with respect to the Debye length. Since the β parameter of equation (1.1) is 1 for a spherical probe, and 0.5 for an infinitely long cylindrical probe, it is assumed that the real effects of both of these assumptions can be captured in the β parameter, with a value approaching 1 as the probe gets shorter (Laframboise 1966; Marholm & Marchand 2020). This was also recently shown to hold true empirically using kinetic numerical simulations by Marholm & Marchand (2020).

Several high quality corrections have been made to the OML theory recently that are regression based, using nonlinear functions like Radial Basis Functions (RBF), or feed forward neural networks (Olowookere & Marchand 2021; Liu *et al.* 2023). These methods can be used to infer plasma parameters, like temperature or density from simulations using the regression model as a "black box". A high degree of complexity can be included, although a complete understanding of the physics is not available. This is possible for specific use cases, for example, by limiting the model to a specific probe geometry, which adds a powerful tool to a specific space mission (Liu *et al.* 2023). In some cases it is also possible to use such methods to construct a more general function, which is more widely applicable (Marholm & Marchand 2020). However, as of now for such general functions, some assumptions need to be made. It is not clear how much these assumptions impact probe measurements. Therefore, in this work we investigate the impact of the two geometrical assumptions commonly made on the guard length, and guard radius.

It is quite common in the design of needle Langmuir probes to accept guard lengths as short as 1–2 Debye lengths (Hoang *et al.* 2018). Recent results have shown that the end-effects can reach much longer than one or two shielding lengths, giving some motivation for testing the common 1–2 Debye lengths assumption (Marholm & Marchand 2020). In addition, seldom is the guard radius of particular interest in needle Langmuir probe design, although it is quite reasonable to assume there are some changes in the probe current when a larger current collector is right next to it. To our best knowledge, these assumptions have never been properly tested. In this article we address this issue, so that previous and upcoming probe designs can get substantive information to base their designs upon.

It is useful for the discussion to understand how the model function is derived for the Finite-Length (FL) theory (see Marholm & Marchand 2020). The Marholm-Marchand model (FL) includes the finite-length end-effects of a cylindrical probe, removing the infinite length probe assumption that was made in the OML theory (Marholm & Marchand 2020). We therefore briefly review it here.

The main idea is that the problem can be completely described by a function that includes all physical parameters that can have an impact. Introducing independent dimensionless variables we can write a relationship between the parameters. The problem can then be reduced by Buckingham's π theorem to yield a function of the form (Buckingham 1914)

$$\mathcal{G}\left(\frac{i}{i_{th}}, \frac{-qV}{k_B T}, \frac{z}{\lambda_D}, \frac{l}{\lambda_D}, \frac{r}{\lambda_D}, n\lambda_D^3\right) = 0. \quad (1.2)$$

Where $\frac{i}{i_{th}}, \frac{-qV}{k_B T}$ are the normalized current and the probe bias potential. $\frac{z}{\lambda_D}$ is the position on the probe $\frac{l}{\lambda_D}, \frac{r}{\lambda_D}$ are respectively the probe length and radius, and $n\lambda_D^3$ is the plasma parameter. We use the Debye length λ_D to normalize the parameters in length. We omit any subscript for the radius r initially since we consider a single free floating cylinder. At this point some assumptions are made that reduce the dimensionality of the problem further.

First, it is assumed that the probe is thin $\frac{r}{\lambda_D} \rightarrow 0$, this is a usual assumption for the Langmuir probes, and it is often stated as $\frac{r}{\lambda_D} < 1$ (see Laframboise 1966). Second, it is assumed that plasma is weakly coupled i.e., $n\lambda_D^3 \rightarrow \infty$, which is also a common assumption. The last two arguments of equation 1.2 can therefore be disregarded, and the equation can be inverted with respect to the first argument to yield

$$i(z) = i_{th} g\left(\frac{z}{\lambda_D}; \frac{l}{\lambda_D}, \frac{-qV}{k_B T}\right). \quad (1.3)$$

Equation 1.3 is for the collected current density at position z on the probe, and the total probe current is then the integral of $i(z)$ over the whole surface of the probe. The parameter space, which the simulations need to span is the length of the probe and the probe potential. A python library using local polynomial regression to make a non-linear fit of the profile function g was made available by Marholm (2019), and the resulting profile functions and corrected currents are available in the Langmuir library (Marholm & Darian 2021). The g functions in the library were constructed from the simulation made by Marholm & Marchand (2019) as a part of the work by Marholm & Marchand (2020).

Figure 1 (a) is adopted from Marholm & Marchand (2020), and together with Figure 1 (b), it shows the assumed probe and guard geometry used in this work. In figure 1 (a) we use the same geometry as Marholm & Marchand (2020), with the addition of a bootstrapped section, also called a spacecraft bus, carrier or boom, on the left side. In this geometry the probe radius and guard radius are the same. In fact, the simulations run in the Marholm-Marchand paper are of a free floating cylinder, and the guard is imposed by removing a section of the profile function g . It is therefore implicitly assumed that the guard radius has no impact on the probe current. In reality the boom-guard-probe geometry is more complex, and while the removed section of the profile function currently removes one of the end points which typically see an increase in the current, a boom will likely lower the current to the same section. In addition, practically the boom-guard-probe system usually needs a guard with a larger radius (Bekkeng *et al.* 2010), which is illustrated in Figure 1 (b), and which likely also impacts the currents to the probe. If we were to include one of these additional parameters, for example the guard radius (and even the normalized guard length L_g/λ_D), equation 1.3 must be extended

$$i(z) = i_{OML} g\left(\frac{z}{\lambda_D}; \frac{R_g}{\lambda_D}, \frac{l}{\lambda_D}, \frac{-qV}{k_B T}\right), \quad (1.4)$$

where $\frac{R_g}{\lambda_D}$ is the normalized guard radius.

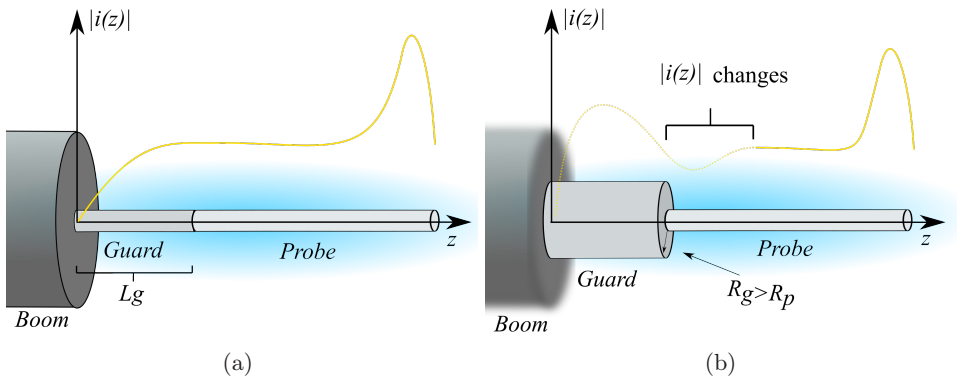


Figure 1: The assumed geometry of the needle Langmuir probe and guard in the FL library Marholm & Darian (2021) (a) including a carrier (boom), compared to a more realistic geometry (b) including a guard with a larger radius R_g . The current $|i(z)|$ curve represents the collected current density on the probe surface as a function of distance z . The dotted part of the $|i(z)|$ curve in (b) represents the region where the current density inferred from the FL library is uncertain due to the presence of a guard and boom. In addition we marked the guard length L_g .

It is roughly enough to use 10 data points per dimension to sufficiently describe equation 1.3 in the range of typical values used in space plasma according to Marholm & Marchand (2020). Therefore, the number of simulations needed to span the two dimensions in equation 1.3 is $10 \times 10 = 100$. If we were to add one parameter, for example the radius of the guard, and this parameter also needed 10 data points, the total number of simulations needed would increase to $10 \times 10 \times 10 = 1000$. While this is a large number of simulations, it is not impossible, but for this to be worth the effort, the added parameter should have a significant impact on the probe current.

2. Particle-In-Cell Simulations

2.1. Numerical Approach

For all simulations in the present work we use PTetra which is a parallelized 3D particle-in-cell (PIC) simulator (Marchand 2012; Marchand & Resendiz Lira 2017). PTetra is a good choice of simulator to use due to the unstructured grid, giving us a high spatial resolution close to the simulated objects like probe and guard. In addition PTetra tracks the current through each surface cell, such that we can get localized currents at discrete points along a simulated surface, and not only the total current to that surface, giving us more information about the current distribution.

2.2. Simulation Setup

We have designed numerical experiments so that each simulation has the same inner resolution of $0.056\lambda_D$ and initially use $50 \cdot 10^6$ simulation particles, or so-called super-particles. In every simulation the plasma parameters are $T_e = 0.1\text{eV}$, and $n_e = n_i = 1 \cdot 10^{11}\text{m}^{-3}$. This gives the Debye length of 7.4mm . We also set the shortest length from the simulation outer boundary to any other simulated surface to be $15\lambda_D$. To speed up the simulations a usual technique is to use a modified ion mass, and we use $m_i = 114m_e$.

We set a sufficiently high positive bias on the probe and guard, so that the attracted species are the electrons. We also set the probe bias voltage equal to the guard voltage. The currents to the probe do not depend on the ion mass with negligible contributions from the repelled ions, as long as we are in the electron saturation regime, i.e., the probe bias is sufficiently large (Marholm & Marchand 2020). This is the case for all probe bias voltages considered in this study. The simulations are then run for $1 \cdot 10^{-5}$ s, or 2.7 ion plasma periods, which is sufficiently long to reach a steady state. To understand the effects of different parts of the Langmuir probe, we split up the geometry and run one set of simulations where we isolate the effects of a charged boom, with varying the guard length L_g . Then we run a second set of simulations where we omit the boom and simulate only the probe and guard, with varying guard radius R_g .

A summary of the parameters for the main set of experiments is listed in table 1. For the first experiment we let L_g vary, and we run the simulations for two probe voltages. In this experiment we use the geometry as in figure 1 (a) where $R_p = R_g$. In reality, the probe and guard will be attached to some surface. This is typically a boom, which has the same floating potential as the main spacecraft body. Spacecraft charge can be calculated by considering the current contributions of different species (Garrett 1981; Whipple 1981). To calculate some typical values of spacecraft potentials ψ_{sc} in the Low Earth Orbit (LEO) we can use the equation given by Anderson (2012)

$$\psi_{sc} = -\frac{k_B T_e}{q} \ln \frac{A_e}{A_i} \left[\frac{k_B T_e}{2\pi m_e v_{sc}^2} \right]^{\frac{1}{2}} \quad (2.1)$$

where the fraction of surface accessible to the electrons with respect to ions is given by $\frac{A_e}{A_i}$, and the spacecraft speed relative to the background plasma is given by v_{sc} . Using typical plasma values, the most realistic values of the spacecraft voltages range from ~ -0.3 V to -0.6 V. It is also noted that spacecraft in LEO rarely experience potentials of more than a few volts negative, which is also supported by observational data (Anderson 2012; Anderson *et al.* 1994). However there are a few examples of high charging events where potentials can exceed 100V negative (Gussenhoven *et al.* 1985; Eriksson & Wahlund 2006; Anderson 2012). This is valid for low background plasma density and high flux of precipitating electrons inside the auroral arc. In these cases the electron distributions are likely to be a two-component Maxwellian (Yeh & Gussenhoven 1987). We do not complicate the simulations with adding high energy precipitating particles at this stage. We therefore use two voltages for the spacecraft/boom in the simulations: we first consider a realistic boom voltage of -0.5 V, and then, a slightly more negative value at -2 V, which are both representative of boom (or spacecraft) voltages in the ionosphere. Due to limited amount of computational resources, we select the most important parameters to vary. Thus, the guard length L_g is varied while the probe length is maintained at $L_p = 10\lambda_D$. We assume that the boom radius is large and set it to $10\lambda_D$. Thus, in this experiment the changes we observe will be attributed to the guard length. We repeat the same process for two different probe radii of $0.1\lambda_D$ and $0.5\lambda_D$, and later refer to these as "small probe" and "large probe", and run each configuration for the probe bias voltage of 1V and 5V. This gives us 56 simulations in the first numerical experiment.

For the second numerical experiment, we use the geometry as in figure 1 (b), where the boom is blurred to show that it is removed from the simulations. We remove the boom to isolate the effects of having a guard radius that is different from that of the probe. We therefore vary R_g while keeping R_p fixed. We reuse the small and large probe with radius of $0.1\lambda_D$ and $0.5\lambda_D$, with probe and guard length of $L_p = L_g = 10\lambda_D$. In Buckingham's π theorem we can choose a dimensionless parameter for R_g , however one may find a

ID	Vp	Rg/Rp	Lg	Vb
1a : $R_p = 0.1\lambda_D$	[1,5] V	1	[1,2,3,4,5,7,10] λ_D	[1,5] V
1b : $R_p = 0.5\lambda_D$	[1,5] V	1	[1,2,3,4,5,7,10] λ_D	[1,5] V
2a : $R_p = 0.1\lambda_D$	[1,5,10] V	[2,3,4,5,8,16]	10 λ_D	N/A
2b : $R_p = 0.5\lambda_D$	[1,5,10] V	[2,3,4,5,8,16]	10 λ_D	N/A

Table 1: Summary of parameters for two main numerical experiments.

better choice, where the two candidates are R_g/R_p , and R_g/λ_D . To investigate this we set $R_g/R_p = 2, 3, 4, 5, 8, 16$ for both the large and small probe. If R_g/R_p is a better parameter to consider, the curves should be quite similar. Although we cannot eliminate the parameter altogether, if the curves are similar then the behaviour of the parameter in the function derived using Buckingham's π theorem gets simpler. In regression tasks in the future this simplicity will likely mean that we can reduce the number of data points needed in the dimension of R_g/R_p or R_g/λ_D . We also run all configurations for three probe bias voltages of 1V, 5V and 10V. The total number of simulations is 36 for this setup, bringing the overall number of simulations for the whole project up to 92.

In the next section we will compare the currents from the present simulations with the Marholm-Marchand model (Marholm & Marchand 2020). To do this we first want to validate, and get an estimate of the error, for the currents in the present setup with respect to the Marholm-Marchand model. The Langmuir library developed for the Marholm-Marchand model was constructed using a single cylinder (Marholm & Darian 2021). For that cylinder, the total current I is an integral of the profile function $i(z)$ which is the current as a function of length along the whole length of the probe. However, since the probe current $i(z)$ is a function of length for that cylindrical probe, defining the probe to be the part of the cylinder, for example, from 0 to $Z/2$ for a cylinder of length Z , the current I is readily available integrating over only the part of the probe from 0 to $Z/2$. This is effectively the same as splitting the cylinder into two separate simulated surfaces at $Z/2$, a probe and a guard in the simulator, and considering only the probe, defined as the surface starting at 0. These two will therefore give the same total current I . In order to verify that this is correct and to get an estimate of the errors for the large and small probe, we ran simulations with $R_g = R_p$, and $L_p = L_g = 10\lambda_D$. That means that in the simulations we define two cylinders of the same radius, and then compare to the Langmuir library, which is based on simulations of a single cylinder, where we set the probe length, and guard length equal to $10\lambda_D$ such that the library does an integration over only the $10\lambda_D$ that correspond to the probe. For the small probe $R_p = 0.1\lambda_D$ the relative errors in percent with respect to FL, at the three chosen voltages are $[-3.52, -1.64, -0.08]$, and for the large probe $R_p = 0.5\lambda_D$ the relative errors in percent are $[6.64, 7.86, 9.45]$. We see that the large probe has the largest error, and it is generally a positive change, meaning that we collect a larger current to the probe than predicted with the Langmuir model. We should keep these errors in mind when evaluating the results later on.

3. Results

3.1. Guard length

The probe currents obtained in the first numerical experiment with setup ID 1 from table 1 are shown in figure 2, with panel (a) including currents for the small probe (ID

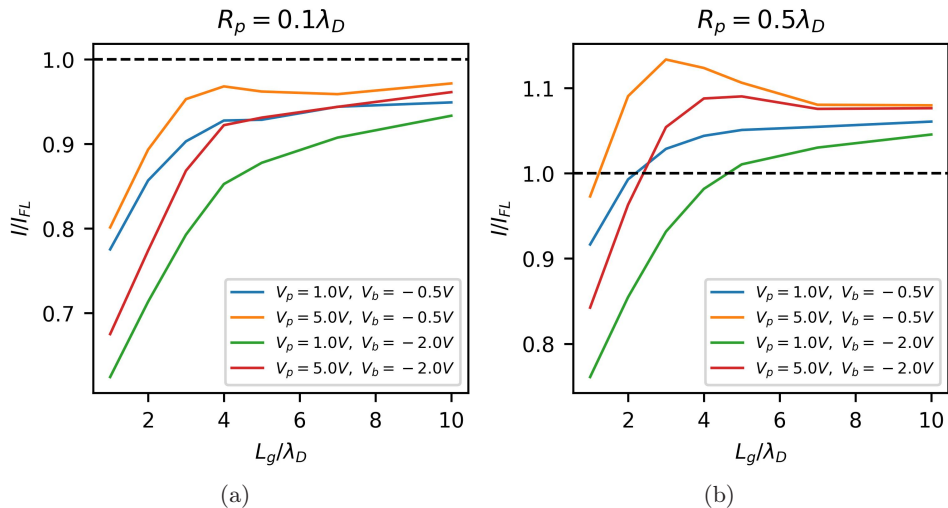


Figure 2: Normalized currents collected by the probe as a function of the guard length. The plots include one data point for each of the simulations listed in table 1 with the simulation ID 1. The guard length L_g is treated as a variable, and the four lines per panel correspond to the four possible configurations of the remaining parameters. The plot shows the ratio I/I_{FL} , where I is computed from the simulations, and I_{FL} is the current obtained from the FL model. Panel (a) contains data for the small probe with probe radius $R_p = 0.1\lambda_D$, and panel (b) contains data for the large probe with $R_p = 0.5\lambda_D$.

1a), and panel (b) including currents for the large probe (ID 1b). The panels include both thermally charged boom (blue, yellow), and higher charged boom (green, red). The only parameter being varied here is L_g . It is reasonable to assume the current values to converge towards the current given by the FL theory. Convergence does not seem to have been exactly reached within the considered parameter space, although, it is in quantitative agreement and within 10%. Similar to the FL theory, the probe needs to be $\gtrsim 10\lambda_D$ before the current $i(z)$ is close to the OML current at the probe center, but the probe needs to be $\gg 10\lambda_D$ before OML is a good approximation for the total current (Marholm & Marchand 2020). It does look like the currents will continue to converge towards the FL theory at some guard length longer than the $10\lambda_D$ chosen here, at least for the case of a small probe. The larger radius for the large probe might be large enough that it contributes to a small deviation from FL theory. The curves gather and flatten out in both cases around $6 - 8\lambda_D$, we therefore deem this to be the length needed for a reasonable degree of convergence, and the length needed for the probes to have a small impact from the boom. For the boom to have zero impact on the probe, the guard needs to be longer than at least $10\lambda_D$, since the curves have not flattened out completely even at $10\lambda_D$. We also see that for the common usage of a guard of $2 - 3\lambda_D$, the error from the charged boom will likely be significant. In addition we can generally state that when the guard is short, the currents are significantly lowered due to the density depletion in the vicinity of the boom. This is therefore in agreement with previous assumptions that a long enough guard leads to minimal impact on currents. However, what is not in agreement is the scale length of the impact.

Another notable effect is that the currents are larger in some cases, with a visible peak

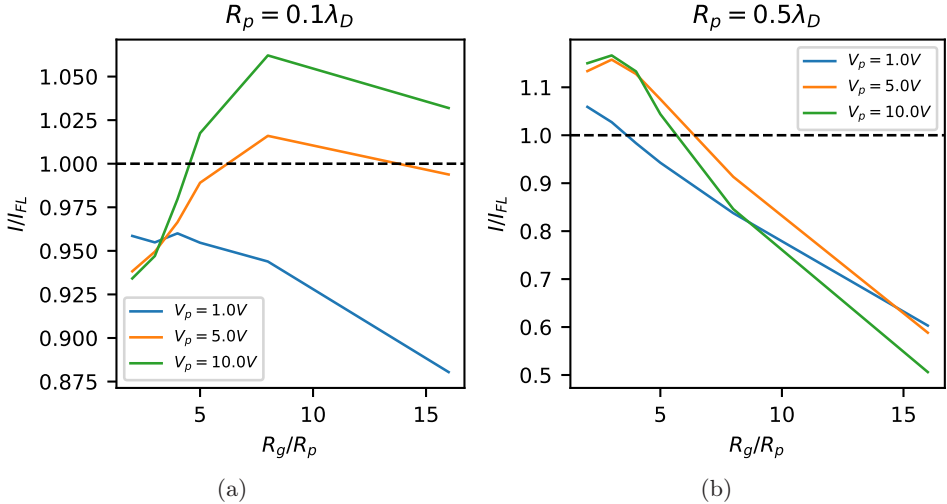


Figure 3: Normalized total currents as a function of the guard length for the second numerical experiment with the simulation ID 2 and parameters listed in table 1. The parameter R_g/R_p is treated as a variable, and the three lines in each panel correspond to the three probe biases simulated. The probe current is normalized I/I_{FL} , where I_{FL} is the current obtained from the FL theory. Panel (a) shows results for the small probe with probe radius $R_p = 0.1\lambda_D$, and panel (b) shows results for the large probe with $R_p = 0.5\lambda_D$.

at $L_g/\lambda_D = 3$ for the large probe with a thermal charging of the boom. A smaller local peak is seen at $L_g/\lambda_D = 4$ for the small probe. This shift in position suggests that this effect is at least dependent on R_p in addition to L_g . This is counter-intuitive, as one would expect the boom to only reduce the currents to a certain degree as it has opposite polarity. This might be different for ion collection since then both boom and probe are normally negatively charged.

For the second experiment we have gathered all simulated currents in figure 3. While we compare results with the FL theory here, we should not expect the currents to coincide with the FL currents since the FL theory is applicable for the "ideal" theory, where it is assumed that $R_g = R_p$. In this experiment the boom is removed from the simulations, and the only varying parameter is R_g . The simulation parameters are summarized in table 1 with setup ID 2. In figure 3, panel (a) is again for the small probe, while panel (b) is for the large probe. The two panels do not follow the same trend, indicating that R_g/R_p is not the best choice of parameter for the dimensionless set of variables. However, we observe a peak for the currents in both panels. In dimensions of λ_D this is at $R_g = 0.8\lambda_D$ for the small probe, and $R_g = 1.5\lambda_D$ for the large probe. This is quite close considering the resolution of $0.5\lambda_D$ for the large probe. This, instead, suggests that R_g/λ_D is a better choice for dimensionless parameter to use. By using R_g/λ_D we also avoid issues in the mathematical model when assuming that $R_p \rightarrow 0$.

It is clear from figure 3, that the currents behave quite differently at high and low probe voltages. For a small probe, in panel (a) for the 1V curve we observe a clear negative trend as the guard radius gets larger. This makes sense as a larger object collecting particles in the vicinity of the probe leaves fewer particles for the probe to collect. However, for both

Loc. quad. regression $R_p = 0.1\lambda_D, V_p$: Loc. quad. regression $R_p = 0.5\lambda_D, V_p$:

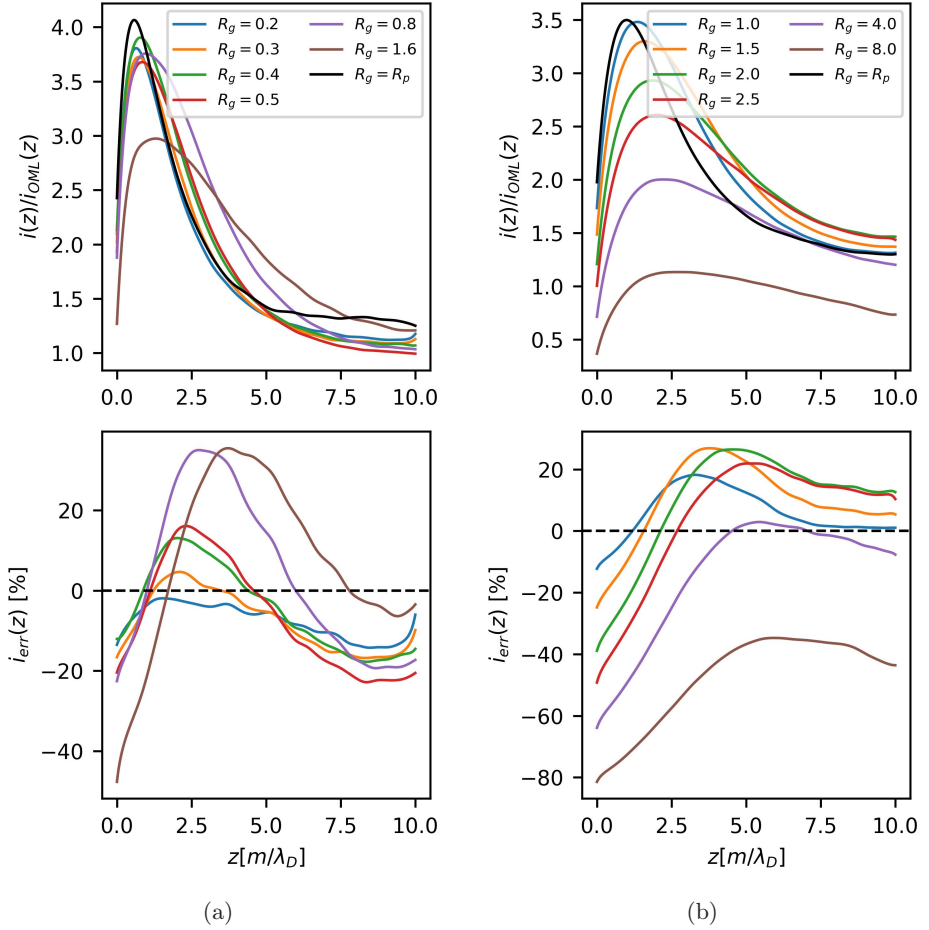


Figure 4: Normalized currents per unit length $i(z)$ as a function of position z along the probe for the second numerical experiment (upper panels). There is one current curve shown for each simulated value of R_g . Values for the small probe $R_p = 0.1\lambda_D$ are to the left (a), and values for the large probe $R_p = 0.5$ are to the right (b). All legends in the upper panes are given in units of λ_D . The lower panels show the percentage change i_{err} with respect to the $R_g = R_p$ curve (i.e., the FL current).

the 5V, and 10V curves we see a peak in the curves, indicating that the guard increases the current to the probe at certain guard radii. This also seems to be true for the large probe, although it is less clear as there is only one simulated sample point before the peak. For the large probe the impact is quite significant when varying the ratio R_g/R_p . However, significant values for change in current to the probe of greater than ten percent occur for $R_g \gtrsim 4\lambda_D$.

3.2. Guard radius

The peaks in the currents seen in figure 3 can be further analyzed by considering the currents as a function of position on the probe (i.e., $i = i(z)$), similarly to what has been done by Marholm & Marchand (2020). Similar to what we did in section 3.1, it would be ideal to compare the regression curves for $i(z)$ from the present simulations to the $i(z)$ curves obtained from the global regression in the FL theory, which are readily available in the Langmuir library (Marholm & Marchand 2020; Marholm & Darian 2021). However, since the changes in current observed in the present simulations are in some cases quite small, it might be misleading to make this comparison as it would be difficult to discern the source of the observed changes when the changes are smaller than the error with respect to the verification simulations. Therefore, we use the verification simulations as a comparison, and use the same local regression technique as in the FL library on the verification simulations and the simulations with ID 2 presented in table 1. The regression on the verification simulations are performed with the same method as the local regressions in the FL library, however, comparing regressions from verification simulations to R_G/R_P simulations will not include the small errors due to the global regression, assumptions on geometry, etc.

For this analysis, we selected 10V-current curves from figure 3 and present the corresponding $i(z)$ regression curves in figure 4. The probe tip is set at $z = 0$, and the probe is attached to the guard at $z = 10\lambda_D$. The small probe $i(z)$ results are shown in the left panels (a), and the results for the large probe are shown in the right panels (b). The upper panels show the normalized current with respect to the OML current, $i(z)/i_{OML}(z)$. To differentiate between the effect of changing the guard radius and the finite length effects we also show in the lower panels the percentage error between $R_g = R_p$ curves and the $R_g \neq R_p$ curves as a function of z . Generally, on the guard side the currents are lowered. This is followed by a relative current error increase towards the tip of the probe, although not at the tip, but at $2 - 4\lambda_D$ from the probe tip, and finally another drop in relative current error at the probe tip. The drop is with respect to the FL current, and is thus an increase with respect to the OML current, according to the FL library. Integrating over the $i(z)$ curves in figure 4 gives the total probe currents we see in figure 3. For small R_g , or lower values in figure 4 (a) $R_g = [0.2 - 0.3]R_p$, the peak in relative current is still lower than the comparison current $R_g = R_p$, in addition to the generally lower currents close to the guard. This means that an integral over this current will lead to a lowered current with respect to the FL current. For large $R_g = [0.8 - 1.6]R_p$ this peak is large and wide, such that an integral over this curve will give a slightly larger current with respect to the FL current. For the intermediate values of R_g we see that there are indeed changes in the currents. However, the maxima and minima in the currents roughly cancel each other after integrating, leading to an overall negligible change in the total current to the probe. For large values of R_g , the larger values in 4 (b), there is a more significant lowering of the current. However, this impact is along the whole probe, and it is most significant at the opposite end of the guard.

The aforementioned area of positive error in the $R_g = 1.5\lambda_D$ (yellow) curve in figure 4 (b) is indeed interesting. In contrast to this area of the probe, the area closest to the guard, between the lower values of R_g in figure 4 (b) to the larger values of R_g in figure 4 (a) suggest that the guards impact on the probe is opposite for the small and large guard in this range of parameters. The idea that the larger guard will serve as a sink of particles, leading to an overall lowering of the probe currents in its vicinity, is in opposition to this result. Therefore other sheath effects must play an important role in this case.

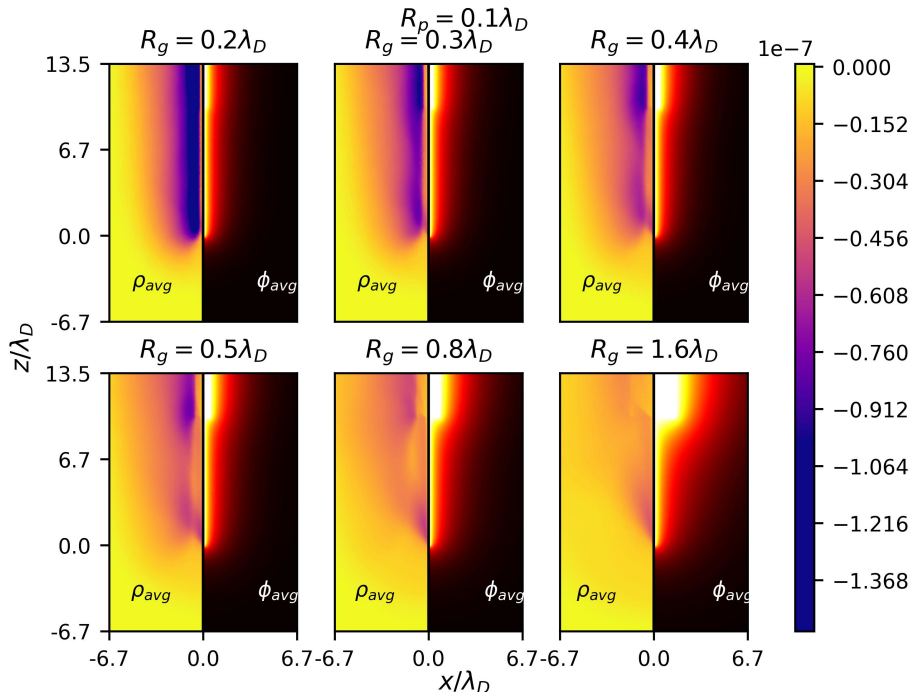


Figure 5: Panels showing slices in the normalized $x - z$ directions of the average charge density ρ_{avg} , and average electric potential ϕ_{avg} in the vicinity of the probe and guard. The simulations selected are from the small probe $R_g = 0.1\lambda_D$ case. The color bar refers to ρ_{avg} in units of C/m^3

3.3. Guard radius effects on the the sheath density

To look closer at the effects of the guard on the probe currents, in figure 5 we plot slices of charge density and potential around the probe and guard from the same simulations as in 4 a), i.e., for the small probe biased at 10V and for varying guard radius. The guard radius increases in each panel from $0.2\lambda_D$ (upper left panel) to $1.6\lambda_D$ (lower right panel), and each panel is split in two along the center of the probe in the z direction running the length of the probe. The left half shows the averaged charge density, and the right half shows the averaged electric potential. The time-averaging follows the averaging scheme given by Marchand (2012) with the relaxation time of $1\mu s$. The added color bar shows the color map for the charge density. We omit the color bar for the electric potential as this goes from 0 to 10V since the probe is biased at 10V.

Figure 5 shows the changes in the density sheath and electric potential as the guard radius is varied. For the charge density, an area of density depletion gets wider close to the probe with the width of the depletion area roughly equal to the guard radius. At transition, which in the present case is close to $R_g = 0.8\lambda_D$, the depletion area is overtaken by a density cone-shape stemming from the tip of the probe. It is not clear currently if this cone-shape is at the tip because the tip happened to be at $10\lambda_D$, or if it will always be at the tip of the probe. It does however seem like the peak in currents observed in figure 4 at $2 - 4\lambda_D$ can be explained by the formation of this cone, as the peaks are located right on the inner edge of the cone structure. A possible explanation

as to how the cone forms can be seen from taking into account the electric potential. In the fourth panel, for $R_g = 0.5\lambda_D$, it seems that particles travel from the edge of the guard towards the probe. Most of these particles are trapped in the potential well of the guard, and will follow the equipotential lines that are pointing slightly in the direction of the probe (radially inwards) in the area between $5 - 10\lambda_D$ in this case. This gives a small amount of particles the additional radial energy needed to overcome the trapping potential.

In figure 4 a) the smallest guard radius $R_g = 0.2\lambda_D$ has a slightly lower current along the whole probe, which might be explained by the density depletion gap close to the probe seen for the smaller values of R_g in figure 5. For these small values, the depletion leads to the lowering of the currents, and the funneling effect discussed over is not large enough to contribute to the current increase at any point.

4. Discussion

The currents in the upper panels of figure 4 include the FL end-effect resulting in an increased current, which is seen as a peak in the current towards the tip of the probe. The FL current peak is in this case 4 times larger (300%) than the OML current. In present simulations, the largest change seen as a result of changing the guard radius is 40% as long as $R_g < \lambda_D$, so the FL end-effect dominates in all the cases considered. However, since we only simulate probes with a probe length $L_p = 10\lambda_D$, and we see that there are changes in the current along the whole probe it is possible that there exists some configuration where the FL end-effect and the effect of varying R_g can contribute to the error on an equal scale. In addition it seems likely that the cone shape observed stems from the probe tip appeared at the tip because it happens to be at $10\lambda_D$. The present setup, where we assumed the probe length to have a minimal impact as long as the probe is sufficiently long for the change in the end-effects (including varying R_g) to be negligible, leaves room for further investigations, and a follow up study that includes a varying probe length in addition to the varying guard radius.

As mentioned earlier, it seems that R_g/λ_D is the best parameter to use for a model using the Buckingham's π theorem. However, the differences between the small probe and large probe do not seem to be negligible, and therefore R_p may also need to be included in the dimensionless set of variables when doing a regression. The initial assumption that R_p is small with respect to λ_D may no longer be valid for the $R_p = 0.5\lambda_D$ probe. This is supported by results in figure 3 where we see that (for relatively small guard radii) the currents for the small probe are all within a five to seven percent band, which is likely within the simulation error, while the errors for the large probe are $> 10\%$. It is likely that $R_p = 0.5\lambda_D$ is the limit of this assumption, and for $R_p < 0.5\lambda_D$, R_p can be neglected, however, for $R_p \geq 0.5\lambda_D$ R_p should be included. In addition, evaluating the changes for a large R_g , if we take for example $R_g = 1.6\lambda_D$ (brown) curve from 4 a), and $R_g = 1.5\lambda_D$ (yellow) curve from 4 b), these two curves should be nearly equal if there were no dependence on R_p . For these curves we see a 20% difference in the current errors at the tip of the probe. There is also an area of negative error for the small probe closer to the guard, while the large probe is positive in the same area. In addition, as seen in figure 3 when integrating over the two curves the difference is 10% ($R_g/R_p = 16$ from panel (a) vs. $R_g/R_p = 3$ from panel (b)). Therefore the differences also seem to appear for higher values of R_g .

As a final example we could evaluate the applicability of these results to a real world scenario. We could for example consider the m-NLP system, which uses a probe with $R_p = 0.25\text{mm}$ (diameter of 0.5mm), and $L_p = 25\text{mm}$. For the guard the radius $R_g = 1\text{mm}$

(diameter of 2mm), and guard length is $L_g = 15\text{mm}$. We include also a quote on the m-NLP design by Hoang *et al.* (2018): "The probes were designed to be much smaller than the Debye length of a few to tens of millimeter for common ionospheric plasma conditions". With the Debye length of tens of millimeters the guard will be close to one Debye length or shorter. In the present numerical setup the m-NLP probes will have a probe length of $3.6\lambda_D$, a guard length of $2.2\lambda_D$, and a guard radius of $\sim 0.1\lambda_D$. With these numbers we can see that the guard length will likely lead to significant errors. In addition, the design being for a few to tens of millimeter, and the usual assumption of $L_g = 1 - 2\lambda_D$ should not be considered sufficient. However, based on the limited present results, the small R_g and small difference in R_g/R_p likely do not contribute to a significant source of error.

5. Conclusions

For the first numerical experiment, where we considered a varying guard length and included a boom, we can summarize the results as follows: In order for the boom to have a small impact on the probe current, the guard needs to be $6 - 8\lambda_D$ long. For a zero impact the guard needs to be longer (or much longer) than $10\lambda_D$. As mentioned earlier, to include the parameter L_g/λ_D in an empirical model we will need up to 1000 simulations. This is not impossible, but expensive computationally considering that the problem can be mostly avoided by enforcing the requirement on the guard length of $6 - 8\lambda_D$ long. However, it may be important in a study where new data is compared with older data if this data was taken with a probe design where only a guard length of $2\lambda_D$ was used as the requirement for the shortest λ_D in its operating range.

For the second numerical experiment, a zero impact on the total current to the probe is only possible for $R_p = R_g$, and this is often practically impossible. However, the impact is small enough that it should not be the major source of error. Again, including R_g as a parameter in an empirical model is possible, but computationally expensive. We therefore need justification for this to be necessary. However, this justification may not be strong as R_g usually has a small effect on the total probe current. However, this is only true as long as the guard radius is not too large with respect to the Debye length. This is usually the case for most of the needle Langmuir probes, however, it is a good practice to explicitly check this condition when using data from a particular probe system.

Data availability

All simulations presented can be reproduced using PTetra v50h. Copies of PTetra can be obtained upon request from Richard Marchand.

The simulation data that support the findings of this study are openly available in Zenodo at <http://doi.org/10.5281/zenodo.8182838>

Funding

This work received funding from the European Research Council (ERC) under the European Union's Horizon 2020 research and innovation programme (Grant Agreement No. 866357, POLAR-4DSpace).

This study was also supported in part by the Research Council of Norway Grant 275653.

Acknowledgments

This research is a part of the 4DSpace Strategic Research Initiative at the University of Oslo.

R.M. thanks the Natural Sciences and Engineering Research Council of Canada for its financial support.

S.M. is grateful towards IFE and Øyvind Jensen for permission to participate in this project.

Declaration of interests

The authors report no conflict of interest.

REFERENCES

- ANDERSON, PHILLIP C. 2012 Characteristics of spacecraft charging in low Earth orbit. *Journal of Geophysical Research: Space Physics* **117** (A7).
- ANDERSON, P. C., HANSON, W. B., COLEY, W. R. & HOEGY, W. R. 1994 Spacecraft potential effects on the Dynamics Explorer 2 satellite. *Journal of Geophysical Research: Space Physics* **99** (A3), 3985–3997.
- BEKKENG, T., BARJATYA, AROH, HOPPE, U.-P., PEDERSEN, A., MOEN, J., FRIEDRICH, M. & RAPP, MARKUS 2013 Payload charging events in the mesosphere and their impact on Langmuir type electric probes. *Annales Geophysicae* **31**, 187–196.
- BEKKENG, T. A., JACOBSEN, K. S., BEKKENG, J. K., PEDERSEN, A., LINDEM, T., LEBRETON, J.-P. & MOEN, J. I. 2010 Design of a multi-needle Langmuir probe system. *Measurement Science and Technology* **21** (8), 085903, publisher: IOP Publishing.
- BUCHERT, STEPHAN C., ERIKSSON, ANDERS, GILL, REINE, NILSSON, THOMAS, ÅHLEN, LENNART, WAHLUND, JAN-ERIK, KNUDSEN, DAVID, BURCHILL, JOHNATHAN, ARCHER, WILLIAM, KOUZNETSOV, ALEXEI, STRICKER, NICO, BOURIDAH, ABDERRAZAK, BOCK, RALPH, HÄGGSTRÖM, INGEMAR, RIETVELD, MICHAEL, GONZALEZ, SIXTO & APONTE, NESTOR 2014 First results from the Langmuir Probes on the Swarm satellites. In *2014 XXXIth URSI General Assembly and Scientific Symposium (URSI GASS)*, pp. 1–1.
- BUCKINGHAM, E. 1914 On Physically Similar Systems; Illustrations of the Use of Dimensional Equations. *Physical Review* **4** (4), 345–376.
- ERIKSSON, A.I. & WAHLUND, J.-E. 2006 Charging of the Freja Satellite in the Auroral Zone. *IEEE Transactions on Plasma Science* **34** (5), 2038–2045.
- ERIKSSON, A. I., BOSTRÖM, R., GILL, R., ÅHLÉN, L., JANSSON, S.-E., WAHLUND, J.-E., ANDRÉ, M., MÄLKKI, A., HOLTET, J. A., LYBEKK, B., PEDERSEN, A., BLOMBERG, L. G. & THE LAP TEAM 2007 RPC-LAP: The Rosetta Langmuir Probe Instrument. *Space Science Reviews* **128** (1), 729–744.
- GARRETT, HENRY BERRY 1981 The charging of spacecraft surfaces. *Reviews of Geophysics* **19** (4), 577–616.
- GUSSENHOVEN, M. S., HARDY, D. A., RICH, F., BURKE, W. J. & YEH, H.-C. 1985 High-level spacecraft charging in the low-altitude polar auroral environment. *Journal of Geophysical Research: Space Physics* **90** (A11), 11009–11023.
- GUSTAFSSON, G., BOSTRÖM, R., HOLBACK, B., HOLMGREN, G., LUNDGREN, A., STASIEWICZ, K., ÅHLÉN, L., MOZER, F. S., PANKOW, D., HARVEY, P., BERG, P., ULRICH, R., PEDERSEN, A., SCHMIDT, R., BUTLER, A., FRANSEN, A. W. C., KLINGE, D., THOMSEN, M., FÄLTHAMMAR, C.-G., LINDQVIST, P.-A., CHRISTENSON, S., HOLTET, J., LYBEKK, B., STEN, T. A., TANSKANEN, P., LAPPALAINEN, K. & WYGANT, J. 1997 THE ELECTRIC FIELD AND WAVE EXPERIMENT FOR THE CLUSTER MISSION. *Space Science Reviews* **79** (1), 137–156.
- HOANG, H., CLAUSEN, L. B. N., RØED, K., BEKKENG, T. A., TRONDSSEN, E., LYBEKK, B., STRØM, H., BANG-HAUGE, D. M., PEDERSEN, A., SPICHER, A. & MOEN, J. I. 2018 The Multi-Needle Langmuir Probe System on Board NorSat-1. *Space Science Reviews* **214** (4), 75.

- HOLBACK, B., JANSSON, S. E., ÅHLÉN, L., LUNDGREN, G., LYNGDAL, L., POWELL, S. & MEYER, A. 1994 The Freja wave and plasma density experiment. *Space Science Reviews* **70** (3), 577–592.
- JACOBSEN, K. S., PEDERSEN, A., MOEN, J. I. & BEKKENG, T. A. 2010 A new Langmuir probe concept for rapid sampling of space plasma electron density. *Measurement Science and Technology* **21** (8), 085902.
- LAFRAMBOISE, J. G. 1966 Theory of spherical and cylindrical langmuir probes in a collisionless, maxwellian plasma at rest. PhD thesis, University of Toronto.
- LIU, GUANGDONG, MARHOLM, SIGVALD, EKLUND, ANDERS J., CLAUSEN, LASSE & MARCHAND, RICHARD 2023 m-NLP Inference Models Using Simulation and Regression Techniques. *Journal of Geophysical Research: Space Physics* **128** (2), e2022JA030835.
- MARCHAND, RICHARD 2012 PTetra, a Tool to Simulate Low Orbit Satellite–Plasma Interaction. *IEEE Transactions on Plasma Science* **40** (2), 217–229.
- MARCHAND, RICHARD & RESENDIZ LIRA, PEDRO ALBERTO 2017 Kinetic Simulation of Spacecraft–Environment Interaction. *IEEE Transactions on Plasma Science* **45** (4), 535–554, conference Name: IEEE Transactions on Plasma Science.
- MARHOLM, SIGVALD 2019 localreg: Local Polynomial Regression. <https://github.com/sigvaldm/localreg.git>, type: python library.
- MARHOLM, SIGVALD & DARIAN, DIAKO 2021 langmuirproject/langmuir:. <https://zenodo.org/record/5469073>, type: python library.
- MARHOLM, SIGVALD & MARCHAND, RICHARD 2019 99 Probes. <https://zenodo.org/record/3269686>, type: dataset.
- MARHOLM, SIGVALD & MARCHAND, RICHARD 2020 Finite-length effects on cylindrical Langmuir probes. *Physical Review Research* **2** (2), 023016, publisher: American Physical Society.
- MOTT-SMITH, H. M. & LANGMUIR, IRVING 1926 The Theory of Collectors in Gaseous Discharges. *Physical Review* **28** (4), 727–763, publisher: American Physical Society.
- OLWOOKERE, AKINOLA & MARCHAND, RICHARD 2021 Fixed Bias Probe Measurement of a Satellite Floating Potential. *IEEE Transactions on Plasma Science* **PP**, 1–9.
- WHIPPLE, E C 1981 Potentials of surfaces in space. *Reports on Progress in Physics* **44** (11), 1197–1250.
- YEH, H. C. & GUSSENHOVEN, M. S. 1987 The statistical electron environment for Defense Meteorological Satellite Program eclipse charging. *Journal of Geophysical Research: Space Physics* **92** (A7), 7705–7715.

Paper III

Spherical Langmuir probes in magnetized plasma. A model based on Particle-in-Cell simulations

S. M. Brask, R. Mishra, G. Holen, Y. Miyake, H. Usui, W.J. Miloch

Accepted for publication in *Physics of Plasmas*.



Spherical Langmuir probes in magnetized plasma. A model based on Particle-in-Cell simulations

S. M. Brask,¹ R. Mishra,¹ G. Holen,¹ Y. Miyake,² H. Usui,² and W. Miloch¹

¹⁾Department of Physics, University of Oslo, P.O.Box 1048 Blindern, 0316 Oslo, Norway

²⁾Graduate School of System Informatics, Kobe University, 1-1 Rokkodai-cho, Nada-ku, Kobe 657-8501, Japan

(*Electronic mail: s.m.brask@fys.uio.no)

(Dated: 14 January 2024)

We present a new model for current collected by a spherical Langmuir probe in magnetized plasmas. Data is obtained using state-of-the-art fully 3D kinetic particle-in-cell simulations. We perform a dimensional analysis and use it to determine the appropriate model function. The model is then empirically derived based on the simulation data for a range of probe potentials and magnetic field values with respect to the Debye length. The final model function is applicable to most space plasmas and can easily be generalized.

I. INTRODUCTION

Langmuir probes have been widely utilized in laboratory and space physics¹⁻⁴. The well-established Orbital Motion Limited (OML)^{5,6} theory is usually used to deduce plasma parameters, such as density and temperature, from the currents that are collected by such probes. The OML theory has proven to be a highly accurate theory under ideal conditions⁷ and robust in some non-ideal conditions⁸. However, the OML theory has been developed for collisionless, unmagnetized plasmas, thus it may be incomplete and erroneous for several use cases in space. For example, measurements by missions close to Earth can be impacted by both collisional effects^{9,10} and magnetic field effects due to Earth's relatively strong magnetic field at $\sim 20 - 50 \mu\text{T}$ ¹¹. Langmuir probes used in missions close to other celestial objects that are embedded in a magnetic field can also be impacted by magnetic effects, such as the BepiColombo mission to Mercury¹², the Cassini-Huygens mission to Saturn and Titan¹³, the JUNO mission to Jupiter¹⁴, or the Jupiter icy moons explorer mission JUICE¹⁵.

Several studies on magnetic effects on charge collectors in plasma have been done in the past¹⁶⁻²⁰. In addition, recently, effects of magnetic fields on objects immersed in plasma have been studied for high-pressure plasmas that are applicable to tokamaks²¹. For low-pressure plasmas, there has been interest in magnetic field effects on the charging of dust grains in flowing plasmas, and a lower charge on dust was demonstrated for stronger magnetic fields^{22,23}. They also show that magnetized plasma flow leads to enhanced and complex wakes that can extend far from the object. These works considered the floating potential of the object, and they are thus not directly applicable to the current collectors in the saturation regime of the current-voltage characteristics. However, these works show that studying magnetic field effects in the context of object charging is of broad interest, and it is likely that similar effects will be present in other cases, such as for biased Langmuir probes.

Development of theory fully describing the complicated dynamics of a current collector in a magnetized plasma has proven to be a very difficult task. This is true even for simple geometries like a sphere or cylinder. These difficulties are

summarized by Laframboise¹⁶ along with an overview of best attempts for theories. In short, the theories seem incomplete due to a large difference between making different assumptions in the derivations, leading to an upper bound (canonical) current, and a lower bound (adiabatic) current that rapidly diverges as the probe potential increases. In addition, numerical integration of the equations of motion for particles in the long Debye length limit shows that the actual current lies likely somewhere in between^{16,17}.

The first attempts towards theories explaining spherical Langmuir Probes in magnetized plasmas were done by Parker and Murphy¹⁸. Additions to this theory were later made by Rubinstein and Laframboise^{19,20}. The normalized current collected by a spherical probe in a magnetized collisionless plasma under steady-state conditions, for an attracted species given by Laframboise¹⁶ is

$$\frac{I}{I_{th}} = \frac{1}{2} + \frac{2}{\sqrt{\pi}} \frac{\sqrt{\eta_p}}{\beta} + \frac{2}{\pi\beta^2}, \quad (1)$$

where $\eta_p = -q\phi_p/kT \gg 1$ is the dimensionless probe potential, and $\beta = r_p/r_g$ is the ratio of probe radius to attracted species mean gyro radius, with $r_g = m\bar{v}_\perp/|q||B|$. The species average speed perpendicular to the magnetic field \bar{v}_\perp is given by the species thermal speed $v_{th} = \sqrt{kT/m}$, and $|B|$ is the absolute magnetic field strength. The currents are normalized by the random thermal current $I_{th} = Sq n_0 \sqrt{kT/2\pi m}$, and $S = 4\pi r_p^2$ is the probe surface area. T, m, q and n_0 are the species temperature, mass, charge, and density. The probe electric potential is given by ϕ_p . The physical constants ϵ_0 , and k are the permittivity of free space and Boltzmann constant, respectively.

In equation 1 the first two terms on the right-hand side coincide with the theory of Parker and Murphy¹⁸, and the last term is the addition given by Rubinstein and Laframboise^{19,20}. Equation 1 is valid for $\eta_p \gg 1$; however the difference between using the full equations (eq. 8-10 in ref.¹⁶) and equation 1 is small even for $\eta_p > 1$ as long as β is also > 1 . Equation 1 is called an upper-bound current¹⁶ since it is built on the assumption that all particle orbits that can intersect the probe surface will be collected. It is therefore a question of

how much this equation overestimates the real currents. This question is partially answered by the significant disagreement between this equation and the single-particle simulation results given by Sonmor¹⁷. However, the latter result is still inaccurate since it uses single particle orbit simulations which neglect space charge effects.

Given the difficulties in deriving an accurate theory, we will here use a different approach. Using Buckingham's π theorem²⁴ we will perform a dimensional analysis of the parameters involved. We will then map the relevant parameter space using fully kinetic three-dimensional Particle-in-Cell (PIC) simulations and will use these results to build an empirical model. Spherical, cylindrical, and plate geometries used for Langmuir probes are of interest; however, as the first step we will in the present work focus only on spherical probes, since, as we will see later, their relatively simple geometry allows us to build an accurate model by sampling the whole relevant parameter space.

A successful model, in addition to capturing the intricate real-world dynamics of magnetized plasmas, should focus on ease of implementation to use it. We therefore will seek a model based on an algebraic expression. An algebraic-based model will be straightforward to deploy in future projects, giving ease of implementation, in addition to offering high accuracy.

II. PIC SIMULATIONS

In all simulations presented in this work, we use the PIC simulator PINC. PINC uses the usual PIC main cycle described in literature²⁵⁻²⁸. The particles are moved using the Boris method^{29,30}, to account for the effects of a static external magnetic field on the plasma dynamics. The electric field is solved electrostatically using the iterative multigrid method with a Gauss-Seidel red-black ordering described in³¹, with a detailed explanation in Killie³². Additional formulations on PINC are given by Marholm³³. The main strength of PINC is in the design of the simulated domain, where both the field quantities and particles are distributed into simulation subdomains such that we can assign one CPU per subdomain, making PINC highly parallelized and able to utilize a large number of CPU's in parallel. PINC has also options for periodic (closed) and open boundaries, with or without plasma flow, and including external magnetic fields. The open boundary employs a Dirichlet boundary condition, where the electric potential is set to zero in the particle frame of reference, and the outermost cell is connected with a Maxwellian plasma outside of the simulation domain. The object (probe) calculations for charge and thus electric potential, use the standard capacitance matrix method^{34,35}, redistributing charge within one timestep, effectively making the object a perfect conductor.

One important aspect of the PIC simulators is that they are collisionless by their design²⁷. Particles within one cell do not "see" any other particles, they only "feel" the collective effects of all particles given from the electric field. Thus effects of collisions, both charged-charged and charged-neutral

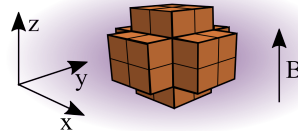


FIG. 1: True simulated geometry surface, as defined by the simulation cells. Geometry represents a sphere with a radius of two grid cell lengths.

are neglected in the standard PIC approach. However, turbulent effects are still included. Thus, the collisionless assumption is included by design, and it makes standard PIC valid for simulating primarily low-pressure, long mean-free-path plasma conditions. Collisions can however be included through statistical Monte-Carlo methods³⁴, such as the null-collision method³⁶. In PINC there is an option to include charged-neutral collisional effects. These methods usually include a statistical consideration of energy transport between charged-neutral species. Since this is a statistical approach and neutral species are not explicitly simulated, it breaks self-consistency¹⁰. We will therefore use in the simulation an option to conserve energy, where the collisional scattering happens without any energy exchange between the particles.

A. Simulation Setup

We will simulate a spherical probe, using a discretization with two cells per radius of the sphere. This choice allows us to have a probe as small as possible, while still having a step length large enough to capture as much of the magnetic bottles extending from the probe along the magnetic field as possible. The magnetic bottles are the area of particle depletion due to collection at the probe that extends along the magnetic field. The density inside and outside the bottle is different since particles are inhibited by the magnetic field, and often have a relatively sharp density gradient at the edge. An in-depth explanation is given by Laframboise¹⁶. Due to the probe surfaces being defined on the uniform cell mesh in PINC, the simulated geometry is as shown in figure 1. The probe is placed in the center of the simulated domain, such that the magnetic bottles along the magnetic field lines extend the same length on both sides of the probe. The simulated plasma is a stationary, nonflowing plasma, such that the magnetic bottles extend in a straight line parallel to the magnetic field in the z direction.

In every simulation, we use a base set of parameters, which are listed in table I. We then vary the magnetic field and probe bias.

Parameter	Value
Δ_t (timestep)	1.5×10^{-9} s
N_t (number of time steps)	55000
$\Delta_x, \Delta_y, \Delta_z$ (spatial step)	0.007m
(N_x, N_y, N_z) (number of cells)	64, 64, 1024
$T_e = T_i$	1000K
m_e	9.11×10^{-31} kg
$m_i = 500m_e$	4.554692×10^{-28} kg
$n_e = n_i$	5.9×10^9 m $^{-3}$
B_x, B_y, B_z	0, 0, 5×10^{-3} T
V_p (Probe bias)	4.5 V
Initial particles per cell	8ppc $\sim 68 \times 10^6$ tot

TABLE I: Simulation input parameters for the base case. Simulations use typical values for temperature T , and density n . The magnetic field B is only non-zero in the z direction. The simulation cells are uniform and have the same length in each direction ($\Delta_x, \Delta_y, \Delta_z$), with the total simulated domain being $(N_x \Delta_x, N_y \Delta_y, N_z \Delta_z)$.

For the plasma density and temperature, we choose typical values representative of the ionosphere. However, the actual values in the SI units are not of primary importance for our modeling since we will be working with dimensionless variables. The collected species is chosen to be electrons, and we set the mass ratio to be $m_i/m_e = 500$, which is quite common to do in PIC simulations to speed up the ion dynamics³⁷. For all probe bias voltages used in this work, the current is in the electron saturation regime. Therefore the ion mass (i.e., repelled species mass) does not enter the equation for the collected current, and the lowered mass ratio should not impact this current significantly. We vary the magnetic field in the range $\|B\| \in [0 - 7] \times 10^{-5}$ T, and the probe bias in the range $V_p \in [1.5, 8.5]$ V. The spacing is chosen such that the probe radius is small with respect to the Debye length, but still as large as possible to capture enough of the magnetic bottle. The number of cells is therefore chosen to be 64 in the perpendicular to the magnetic field direction, and 1024 in the parallel to the magnetic field direction. Theoretically, neglecting kinetic effects, the length of the magnetic bottles tends to infinity along the magnetic field direction. This is not possible to simulate, and we therefore must select an appropriate length of the system to simulate. This length of 1024 cells was chosen by running a set of test simulations with a magnetic field of 5×10^{-5} T and varying the system length up to 4096 cells, where negligible change in current was observed for systems longer than 512 cells length.

Derived parameters highlighting the resolution of the simulation setup are given in table II.

Parameter	Value
λ_D	0.0284m
L_x, L_y, L_z (sim length)	[0.448, 0.448, 7.168]m
L_x, L_y, L_z (sim length)	[15.77, 15.77, 252.39] λ_D
$v_{th,e}$	12311m/s
$v_{th,i}$	5505m/s
ω_{pe} (electron plasma frequency)	4.3×10^6 rad/s
ω_{pi} (ion plasma frequency)	1.94×10^3 rad/s
r_{ge} given $ B = 5 \times 10^{-3}$ T	0.014m
r_{gi} given $ B = 5 \times 10^{-3}$ T	0.313m
ω_{ce} (electron gyro frequency)	8.79×10^6 rad/s
ω_{ci} (ion gyro frequency)	1.76×10^4 rad/s
electron plasma periods	56.88
ion plasma periods	2.54
electron cyclotron periods	115.46
ion cyclotron periods	0.23

TABLE II: Simulation derived parameters highlighting the simulation resolution. All parameters are well resolved, and typical scales are covered. The exception is the ion cyclotron period, which likely does not greatly impact electron current collection, due to weak magnetization of ions.

Although the simulated probe geometry is a low-resolution discrete representation of a sphere, it has proven to work well in earlier work^{10,35}. In addition, we can verify the current setup by comparing the unmagnetized simulations with the OML current⁶. For this test, we pick two values of probe bias 4.5V and 2.5V. For the 4.5V simulation we get an error of -1.5% , and for the 2.5V simulation it is 1.6% , which is adequate when considering PIC simulations.

B. Simulation Results

We start with presenting general results. Figure 2 shows how the shape of the sheath in density around the spherical probe changes from the standard spherical sheath to a donut-shaped sheath as the magnetic field increases. The panels in figure 2 show only half of the probe with the center of the simulated domain set to $z = 0$, and for clarity of the figure, we include only a part of the magnetic bottles along z . Another interesting observation is that not only does the shape of the sheath change but also the peak density inside the sheath is lower for the cases with a high magnetic field. The donut-shaped sheath has also been reported in laboratory experiments^{16,38}.

The spherical sheath used to derive the Orbital-Motion-Limited OML current^{5,6} which in spherical coordinates is symmetric in two dimensions. Mathematically the spherical symmetry is much simpler to work with than the donut shape which is symmetrical only about one axis. This sheath asymmetry is one of the main reasons why a complete theory for the magnetic case is so hard to derive.

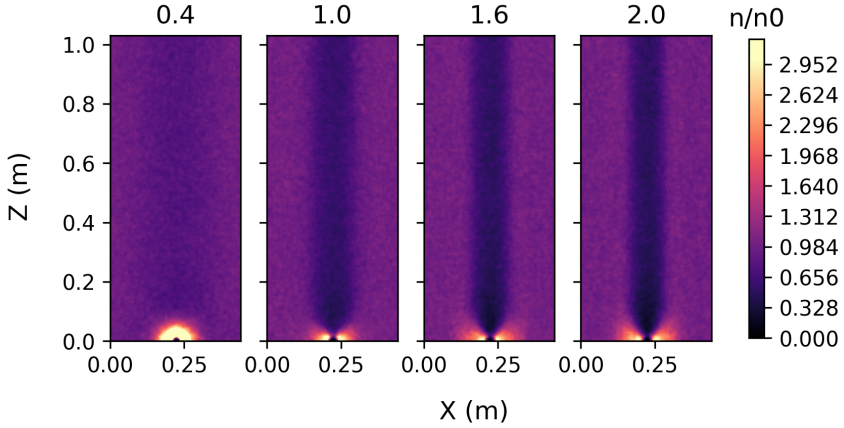


FIG. 2: The electron density distribution around a spherical probe biased at 4.5V for four values of the magnetic field strength: $B_z = [1, 2.5, 4, 5] \times 10^{-5} \text{T}$, and $\beta = [0.4, 1.0, 1.6, 2.0]$. [Associated dataset available at <http://dx.doi.org/10.5281/zenodo.8370038> (Ref.³⁹)]

C. Dimensional analysis

The reasoning in this section closely follows the similar reasoning of Marholm³⁷. We wish to determine the attracted-species current I for a spherical probe. First, we can assume that the current can be fully described by a relation between all relevant parameters. For a free-floating conductive sphere in a plasma, in addition to the current I , the relevant parameters will be the potential V and probe radius r_p , as well as the attracted species properties, mass m , charge q , density n , and species energy kT . In addition, it is reasonable to assume that the vacuum permittivity enters the equation. Lastly, we wish to include magnetization by adding the magnetic field strength $|B|$. The relation can then be written as:

$$\mathcal{F}(I, V, r_p, q, m, n, kT, \epsilon_0, |B|) = 0. \quad (2)$$

We can now use Buckingham's π theorem^{24,37} to reduce the dimensionality. The dimensions of all of the parameters involved can be described by the four SI units: meters, kilogram, seconds, and Ampère, therefore this forms a 9×4 dimensional matrix with rank 4, and the relation can be written using $9 - 4 = 5$ parameters²⁴. The parameters can be chosen freely as long as they are independent. First, we include normalized current and potential

$$\frac{I}{I_{th}}, \frac{-qV}{kT} \quad (3)$$

We normalize the lengths by the Debye length, $\lambda_D = \sqrt{\frac{\epsilon_0 kT}{nq^2}}$

$$\frac{r_p}{\lambda_D}, \frac{r_g}{\lambda_D}, \quad (4)$$

where we included the magnetization through the species average gyroradius $r_g = \frac{m\bar{v}_\perp}{|q||B|}$. Last, we include the plasma parameter such that the reduced equation we choose can be written as

$$\mathcal{G}\left(\frac{I}{I_{th}}, \frac{-qV}{kT}, \frac{r_p}{\lambda_D}, \frac{r_g}{\lambda_D}, n\lambda_D^3\right) = 0. \quad (5)$$

The hitherto unknown function \mathcal{G} can be inverted with respect to the first argument. If, in addition we make additional assumptions that $r_p \ll \lambda_D$, and $n\lambda_D^3 \rightarrow \infty$ we get

$$\frac{I}{I_{OML}} = g\left(\frac{-qV}{kT}, \frac{r_g}{\lambda_D}\right). \quad (6)$$

Where we also pulled out a factor from \mathcal{G} such that the normalization factor for I is I_{OML} . We can call g the correction function. Note also that we have used $\frac{r_g}{\lambda_D}$, instead of the common $\frac{r_p}{r_g}$. This is done to make the dimensionless potential and magnetization independent variables and to avoid any problems with the assumption of $r_p \ll \lambda_D$. For the sake of building a model, we will initially make the nontrivial assumption that I is only weakly dependent on the potential such that we can write equation 6 as

$$\frac{I}{I_{OML}} = g\left(\frac{r_g}{\lambda_D}\right). \quad (7)$$

We will discuss this assumption further later and will expand the parameter space by including potential. However, we make this assumption initially to build a model as simple as possible, and we will increase complexity in subsequent

sections. We will also use the magnetization as the inverse of $\frac{r_g}{\lambda_D}$, such that $\beta = \frac{\lambda_D}{r_g} \propto |B|$, this makes no difference for the dimensional analysis; however the latter is easier to discuss and interpret. In addition, we will use the definition $\eta = \frac{-qV}{kT}$ for the dimensionless potential.

III. A MODEL FUNCTION

In principle, any suitable function that can be fit to the data from simulations can be used. One approach would be to use nonlinear regression techniques like a neural network⁴⁰, or radial basis functions³⁷, that can be fit to any set of data. However, these techniques require a large set of coefficients and parameters to use. Therefore there is a larger technical barrier to implementing them in subsequent work. In addition, the complexity of these functions makes analyzing them difficult, e.g., by taking the derivative. Our approach therefore seeks an algebraic expression. We chose here to start with a physical argument for the form of the function, although we wish to stress that this is still an empirical approach.

The argument goes as follows: first, we recognize that particle movement is inhibited in a plasma when an external magnetic field is applied. The inhibition is perpendicular to the magnetic field, and along the field, the particles are free to move as if there is no magnetic field. This means that effectively, the application of a magnetic field makes a part of the probe surface unavailable to the particles in the direction perpendicular to the field. At some point for a strong magnetic field, particles must strictly follow the magnetic field lines reducing the effective surface area available to a disc instead of a sphere of the same radius. From this point, increasing the field intensity will not make a difference. However lowering it will increase the current until the magnetic field is zero, where unmagnetized theory is valid again. We therefore model the current as an effective surface area:

$$\frac{I}{I_{OML}} = \mathcal{S}^* = \frac{\mathcal{S}_{eff}}{\mathcal{S}_0}, \quad (8)$$

where \mathcal{S}_{eff} is the effective surface area available to the magnetized particles and \mathcal{S}_0 is the actual unmagnetized surface area. Where we chose a function for \mathcal{S}^* that fits the above description. We can define these criteria rigorously as

$$\lim_{\beta \rightarrow \infty} f(\beta) = C, \quad C \neq 0, \quad (9)$$

$$\lim_{\beta \rightarrow 0} f(\beta) = 1. \quad (10)$$

Where $f(\beta) = \mathcal{S}^*$ and C is a constant that is unknown at this point. We also see that \mathcal{S}^* is the correction function from equation 6 or 7. A successful function needs to converge towards a lower value as β increases. Based on the results in figure 3 it is reasonable to use an inverse exponential function and choose one on the form

$$\mathcal{S}^* = e^{-A\beta - C} + C, \quad (11)$$

or we can use an algebraic equation in the form

$$\mathcal{S}^* = \frac{1 - C}{\sqrt{1 + A\beta^2}} + C. \quad (12)$$

We will test both equation 11 and equation 12 as possible candidate models in the following. We can take note that equation 11 does not strictly follow the criteria in 9; however, it is close as long as C is small.

It might be tempting to interpret the last part of equation 11 and equation 12 as the surface area of the disc in a highly magnetized plasma; however \mathcal{S}^* is a dimensionless empirical function, and so C should be considered as a placeholder that does not have any meaning unless multiplied by for example \mathcal{S}_0 , which when combined, they would be the effective disc surface \mathcal{S}_{eff} , when, for example $\frac{1 - C}{\sqrt{1 + A\beta^2}} = 0$.

A. Fit of model to single bias data

We now fit \mathcal{S}^* to data using a least squares regression to determine the coefficient A and constant C . We chose here to use only the 4.5V data since we know that the assumption that potential does not impact the correction function is likely not valid. This fit is therefore only highly accurate for $\eta \sim 50$.

model	A	C	R^2	RMSE	MAE
model1	1.438	0.125	0.9987	0.011	0.010
model2	10.068	0.0317	0.9998	0.004	0.003

TABLE III: Table listing coefficients and 'goodness of fit' R^2 parameter. [Associated dataset available at <http://dx.doi.org/10.5281/zenodo.8370038> (Ref.³⁹)]

In table III we list the model coefficients obtained from the regression. In addition, we list three relevant evaluation metrics. First, we include the 'goodness of fit' R^2 parameter which is a measure of how much of the observed variance in the data is explained by the model. $R^2 = 1$ would mean that everything is explained and the data and model agree perfectly. Thus, the values we obtain are quite good. However, at this point, we included a small number of data points in the regression which may affect this result. In addition, we present the root-mean-squared error which is the quadratic mean of the error between the data and the model points, and mean absolute error, which is the mean sum of absolute errors. Both can be considered a measure of how far apart the data points and model points are on average. Both have small values indicating a good fit.

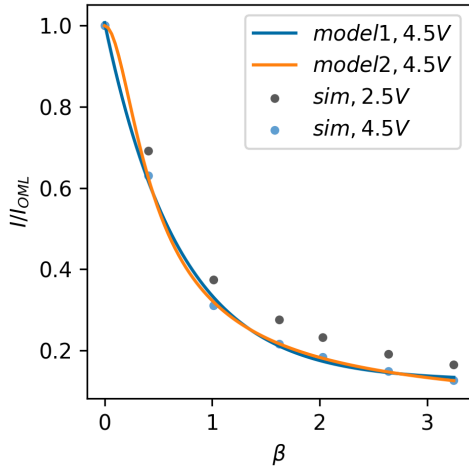


FIG. 3: Normalized currents (dots) for simulations for five values of the magnetic field $B_z = [0, 1, 2.5, 4, 5, 6, 7] \times 10^{-5} \text{T}$ ($\beta = [0.4, 1.0, 1.6, 2.0, 2.6, 3.3]$), and 2 values of probe bias $V_p = [4.5, 2.5] \text{V}$. Compared to the two candidate models in equation 11, and 12 (solid lines), constructed using the 4.5V data. [Associated dataset available at <http://dx.doi.org/10.5281/zenodo.8370038> (Ref.³⁹)]

In figure 3 we plotted some selected data points along with the two model functions using their respective coefficients. The selected data is for the base case voltage 4.5V, and we added data for a probe bias of 2.5V for comparison. We call the fit to equation 11 model1, and the fit to equation 12 model2. As we see in figure 3, the difference between the 2.5V data and the 4.5V data is much smaller than the difference from including even a moderate magnetic field. Therefore, being as simple as possible function both models seem to yield more accurate results than using unmagnetized theory alone.

From table III we can also see that model2 has the best metrics, and it also follows criteria in 9, and 10 better. We therefore choose to continue using model2 from equation 12 in the remaining of this study.

B. Determining C from physical argument

We can calculate the value of C based on the physical argument outlined above. To do this we first calculate the extrema values of \mathcal{S}^*

$$\mathcal{S}^* \Big|_0 = \frac{1-C}{\sqrt{1+A\beta|_0^2}} + C = 1 - C + C = 1, \quad (13)$$

$$\mathcal{S}^* \Big|_\infty = \frac{1-C}{\sqrt{1+A\beta|_\infty^2}} + C = \frac{C}{1} = C. \quad (14)$$

By assuming that the effective surface area for an unmagnetized probe is a sphere and that the effective surface area for an infinitely magnetized probe is a two-sided disc we get

$$\frac{\mathcal{S}^* \Big|_\infty}{\mathcal{S}^* \Big|_0} = \frac{2\pi r^2}{4\pi r^2} \quad (15)$$

Combining this result with equation 13 and equation 14 we get

$$C = \frac{1}{2}. \quad (16)$$

Comparing this value to the values of C in table III we see that C in equation 16 is larger than both. It seems that since the C parameter becomes smaller with a higher probe potential, the $C = 0.5$ value is a boundary value, i.e., a maximum value of C , for the ideal case where the probe potential is zero, $\eta = 0$. As such, it represents the minimal impact possible due to magnetization and it can therefore be considered safe to use in all cases as long as it is understood that it underestimates to a certain degree. Note also that this function will not be accurate for $\eta = 0$. As stated in the introduction, all simulations are done in the electron saturation regime, meaning that the results are only valid in saturation. This is clearly not the case if $\eta = 0$. The $C = 0.5$ value is however consistent with the earlier best attempts given in equation 1, when $\beta \rightarrow \infty$. Thus, model1 converges towards the "canonical upper" theory given by Laframboise¹⁶ at the limit of infinite magnetization, and for small probe potentials η .

It is well known that the area of collection for a probe in the unmagnetized case extends well beyond the probe surface, and through the probe sheath. This will not be the case for a probe in an infinitely magnetized plasma. In this case, the gyro radius tends to zero, and the particles strictly follow the magnetic field lines. Therefore, a more realistic calculation can use instead the probe sheath as the collection area for the unmagnetized probe $\mathcal{S}^* \Big|_0$. The sheath thickness is given by the potential expanded sheath⁵

$$S_s = S_p(1 + \eta), \quad (17)$$

where S_p is the probe surface. Using the sheath expanded surface S_s as the collection surface for $\mathcal{S}^* \Big|_0$, and using a two-sided disc as the probe surface for the magnetized probe $\mathcal{S}^* \Big|_\infty$, we get the value $C = 0.0094$. This value is quite close to the value for C given in table III. This gives further weight to model1, and it also indicates that this method can be used to calculate C values for a given η . The $C = 0.0094$ value is valid for $\eta = 52$.

C. A model including η as a variable

We have seen that there is a weak dependence on η in the simulations. We wish to build a model that can account for this dependency. We therefore start with model2, equation 12, and include the V_p , or η dependence in the parameter C by changing the parameter to be a function that depends only on the dimensionless probe potential $C := C(\eta)$.

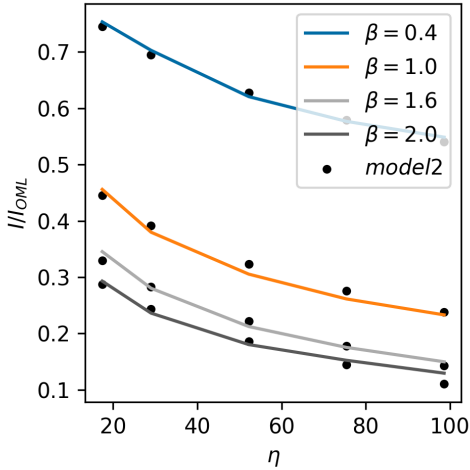


FIG. 4: Plot of the full model and simulation data, showing the shape of the curves in current-potential space. Selected values of magnetic field that are not zero are included. The plot also shows good agreement between the simulation and the full model. [Associated dataset available at <http://dx.doi.org/10.5281/zenodo.8370038> (Ref.³⁹)]

To decide a suitable function we first plot the currents obtained in the simulations as a function of η in figure 4. The simulation curves, for different magnetization, along η do not follow a linear trend. However, the trend seems to be consistent for different magnetization values, which is promising.

We tested different candidate functions that generally followed a simple rule: they should converge towards a constant, and be as simple as possible. We ended up using the function $C(\eta) = B\sqrt{\eta} + C'$, where B is a new coefficient, and we marked C' to differentiate it from the previous C although it is similar to the old C . C' is also therefore a new coefficient. The full model expression can then be written as

$$\mathcal{I}^* = \frac{1 - (B\sqrt{\eta} + C)}{\sqrt{1 + A\beta^2\sqrt{\eta}}} + (B\sqrt{\eta} + C). \quad (18)$$

We, therefore, have three fitting coefficients, and 28 data points to fit in the range of $\eta \in [15 - 98]$, and $\beta \in [0 - 3.2]$. Note that we added a cross-parameter effect in the denominator of the first part of the model expression by multiplying

the two parameters: $\beta^2\sqrt{\eta}$. This gave slightly better model performance metrics. After a multivariate least squares regression we obtain the performance metrics for the model in equation 18 listed in table IV

	A	B	C	R^2	RMSE	MAE
full model	1.390	-0.022	0.197	0.997	0.010	0.009

TABLE IV: Table listing coefficients and 'goodness of fit' R^2 parameter. [Associated dataset available at <http://dx.doi.org/10.5281/zenodo.8370038> (Ref.³⁹)]

We included the same metrics for the full model as we did for model1 and model2 in table III. Compared to the previous model2 metrics this full model has slightly worse performance. However, these results with many more data points and the numbers in table IV are still very good. We have plotted lines for all the simulated probe bias voltages used for the model against the simulated data points in figure 5 showing the good agreement between the model curves and simulation data. In addition, there are no outliers and all simulation-model errors are within simulation-reality acceptable errors.

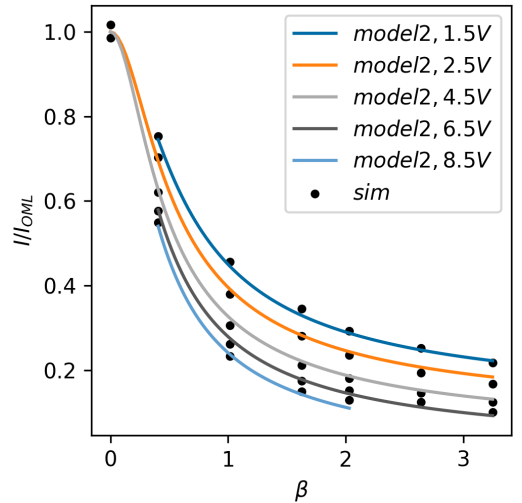


FIG. 5: Normalized currents from simulations for seven values of $B_z = [0, 1, 2.5, 4, 5, 6, 7] \times 10^{-5} \text{T}$ ($\beta = [0.4, 1.0, 1.6, 2.0, 2.6, 3.3]$), and five values of probe bias $V_p = [1.5, 2.5, 4.5, 6.5, 8.5] \text{V}$ (shown as dots). The simulation results are plotted against the full model given by equation 18. [Associated dataset available at <http://dx.doi.org/10.5281/zenodo.8370038> (Ref.³⁹)]

Omitting the $\beta^2\eta$ cross dependence, we can also calculate the infinite magnetization, zero probe bias value, which represents an "ideal" case where only magnetization effects are evaluated. In this limit, $\mathcal{I}^* = C$, which is consistent with the earlier results.

IV. VERIFICATION OF THE MODEL

As a limited verification of the model, we ran a small set of verification simulations. The simulations use modified plasma parameters in SI units; however, the dimensionless parameters are maintained fixed. We then ran four simulations with different magnetic fields, where each value also corresponds to one of the dimensionless β values used in the base case. In table V we have listed the SI parameters used.

Parameter:	V	T	n	$ B $	λ_D	r_p/λ_D
Base	2.5	1000	5.8977e9	5.0×10^{-5}	0.0284	0.4927
Verif	5.0	2000	5.8977e8	1.58×10^{-5}	0.1271	0.5036

TABLE V: Table listing the different parameters used in SI units for the base case, and the verification set. These parameters give the same values in dimensionless units of η , β , and length, e.g. dimensionless probe radius r_p/λ_D , for both cases.

The parameters used give the same values in dimensionless units, where $\eta = 29$, and $\beta = [0.0, 0.4, 1.0, 1.7, 2.1]$. The $|B|$ given in table V is the largest value used for this test.

To evaluate the correctness we calculate the same metrics that were used in the regressions above. In this case, we do not do a regression, but instead use the coefficients from table IV.

Metric:	R^2	RMSE	MAE
Verif	0.998	0.014	0.013

TABLE VI: Metrics for the validation simulations. There was no regression performed to obtain these.

As we can see in table VI the verification simulations fit the model as well as the base simulations. For the verification simulations, the R^2 parameter is slightly better. On the other hand, RMSE and MAE are slightly worse. The differences are small enough that they can be neglected. This shows that the model works on a different data set. Due to computational constraints, the test set was small. We therefore feel there are a few additional arguments for the model's accuracy to point out. First, the assumption on probe radius is the same as in OML theory. In OML theory it is assumed that $r_p/\lambda_D \ll 1$; however it is shown that OML is accurate for $r_p/\lambda_D \leq 0.5$ for spherical probes, and even $r_p/\lambda_D \leq 1$ for cylindrical probes⁶. Mathematically, if the assumption $r_p/\lambda_D \ll 1$ is satisfied, the model we build is accurate and independent of the size of r_p . What is not entirely clear is if the currently used r_p is small enough. However, since we make the same assumption as in OML here it is reasonable to expect the same inequalities to hold in the magnetized case. We will not do a more in-depth verification at this point. However, to remove any doubt on the model's limitations this should be done in the future. As for η , since we do expand the parameter in the model, and we use dimensionless parameters, it should be correct within the range used. For η , it would be good to further expand the dimension to map out the actual limitations of this parameter for the model.

V. DISCUSSION

A. Charged-neutral collisional effects

One major question for the lower ionosphere where the plasma temperature drops and the magnetization ratio increases is what role charged-neutral collisions play. In this region, charged-neutral collision frequencies also increase as plasma temperature drops. We include in this section an example, without doing any modeling, of what happens in a magnetized case when collision frequencies increase. We use the same plasma parameters as in the base case, with a magnetic field strength of 5×10^{-5} T which is a typical value used for the earth's magnetic field in the lower ionosphere. We run six simulations with electron collision frequencies in the range $\nu_e \in [0 - 1 \times 10^7]$ s⁻¹. We also include ion collisions where the ratio of electron-neutral to ion-neutral collisions are calculated using the equations of Brekke⁴¹, although the ion collisions should not impact the result meaningfully since we study the probe in the electron saturation regime.

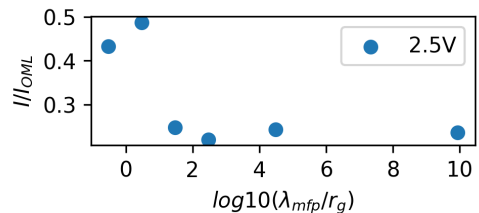


FIG. 6: Plot of the dimensionless current I/I_{OML} against the logarithm in base 10 of dimensionless Mean-Free-Path as $\log_{10}(\lambda_{mfp}/r_g)$. The Mean-Free-Path is given as the electron-neutral collisional Mean-Free-Path.

In figure 6 we have plotted the currents against the Mean-Free-Path in dimensionless values. The Mean-Free-Path is given as the electron-neutral collisional Mean-Free-Path, $\lambda_{mfp} = V_{th,e}/\nu_e$, and the normalization parameter used to make the Mean-Free-Path dimensionless is the electron gyro radius r_g . We chose to use the gyro radius instead of the Debye length since in this case, it is a question of what effect is dominating either magnetization or the collisional effects. As we see in figure 6, there is a small increase in current for short Mean-Free-Path, when $\log_{10}(\lambda_{mfp}/r_g) < 2$. The effect of current increase for weakly collisional plasma is reported in several works^{9,10}, and this effect has been discussed by Laframboise¹⁶. This result would be similar if we used Debye length as the normalization parameter since in this case, Debye length and electron gyro radius are in the same order of magnitude.

One important observation is that the currents are always much lower than the unmagnetized collision-free OML current. However, the problem of including collisions is likely even more complicated in the lower magnetized cases, where

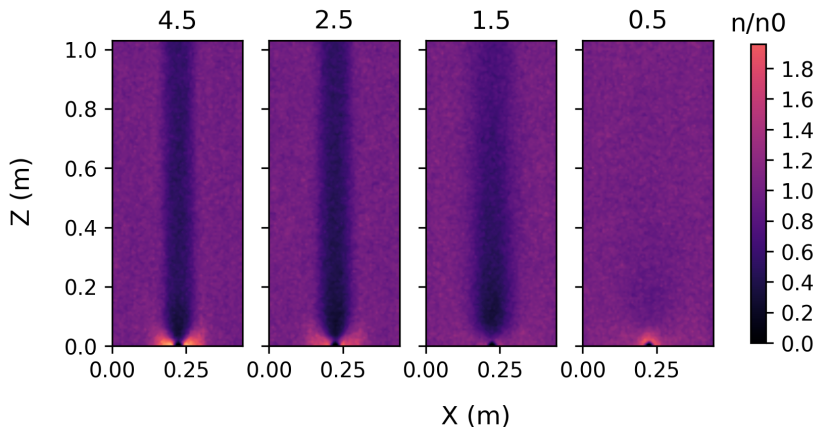


FIG. 7: Electron density for four cases of increasing collision frequency $\nu_e = 2.91 \times [10^2, 10^4, 10^5, 10^6]$. The parameter at the top is the collisional parameter $\log_{10}(\lambda_{mfp}/r_g)$.

increases in current such as discussed in Laframboise¹⁶ might occur.

If the collisional effects were to be included in an empirical function, like the one given in equation 18, we would need to run many more simulations. Including an additional parameter in equation 2, without doing any additional assumptions, will lead to a correction function g with an additional parameter. That means that instead of spanning a two-dimensional parameter space with simulations we will need to span a three-dimensional space, where $n_{sp} \propto n^d$. The number of simulated data points needed n_{sp} scales proportional to the power of the dimensionality d of the parameter space.

In figure 7 we have plotted the electron density for four simulations with increasing collision frequency (decreasing λ_{mfp}). In figure 7 we plotted the same selection of the domain as in figure 2, where only half the probe is shown, and centered at $z = 0$. The last plot on the right-hand side corresponds to the highest current in figure 6. What we see here is the effect commonly referred to as "breakdown of magnetic insulation"¹⁶. The interesting observation is that as collisional effects start to dominate, when $\lambda_{mfp} \sim r_g$, we get the "breakdown of magnetic insulation". This leads to the sheath reverting to the unmagnetized spherical shape, instead of the donut shape that we can observe on the left panel in figure 7. However, this does not lead to a complete reversion of the currents back to the OML current. Instead, there seems to be some resistance inhibiting the flow of electrons to the probe, either from magnetic or collisional resistance.

An expanded model to include charged-neutral collisions is beneficial in some cases. However, we would need to span an additional parameter space (three instead of two already spanned). If we need ca. 5 simulated points per parameter, for two parameters we would need $5^2 = 25$ simulations. If we include collisions we need $5^3 = 125$. While it is possible, we would need many more simulations, and this task is therefore

left for future work.

As discussed in the previous works¹⁶, collisional effects, including collisional ionization, may increase the collected currents. This is supported by laboratory experiments⁹, and unmagnetized simulation results¹⁰. However, we observe that magnetization leads to a lowering of the collected currents w.r.t OML for all values of collision frequency, see again figure 6. In addition, collisions have an effect when the mean-free-path is on the order of the gyro-radius. As long as the mean-free-path is orders of magnitude longer there should be a negligible impact from collisions. This is usually the case for space plasmas. Even when collisional effects are large, the currents never reach the OML values. Therefore, there does not seem to be any collision frequency where it is safe to say that the magnetic effects can be neglected, due to collisional effects, as long as magnetic effects are large enough to also be important. Another interesting observation, including the general collisional effect of increasing the currents in the intermediate collisional range,^{10,16} is that in the range where mean-free-path, gyro radius, and Debye length are close to each other in size, there likely are significant effects, including cross-effects between all of these parameters, making it highly unpredictable, and complex. This can happen in the lower E-region of the ionosphere. In this case, a model including all three parameters would be beneficial.

B. General Discussion

In the derivation of the models we initially made the assumption that $r_p \ll \lambda_D$. This was done so that r_p did not need to be included in the dimensionless set of parameters included in equation 5. This is a common assumption to make^{6,37}. For the dimensionless analysis, this works out mathematically; however, in the case of including a magnetic field this as-

sumption may be less trivial, and the question of how small r_p should be is more oblique. Secondly, questions about the use of r_g/λ_D v.s. r_p/r_g might be raised. For incident particles, following the magnetic field lines, is it the gyro radius w.r.t. the probe radius, or w.r.t. the Debye length that is most important? In both of these questions, it seems that consistently using λ_D as the normalization factor is best, and the size r_p should follow similar assumptions and rules as in the OML theory. This is because the sheath length, i.e. the collection area, in the magnetic case does not depend in large on the magnetization, and it has a similar length in the direction perpendicular to \vec{B} in every case, for the same bias, as seen in figure 2. In addition, for the second question, using r_g/λ_D is better suited for Buckingham's π theorem. If we were to try and use r_p/r_g it would interfere with the assumption that $r_p \ll \lambda_D$, since this assumption then also leads to $r_p/r_g \rightarrow 0$. As such the parameters r_p/r_g , and r_p/λ_D are in addition not independent, which is a requirement in Buckingham's π theorem. The mathematical framework we have used is therefore robust. However, a more in-depth verification is still needed, and some focus on how small r_p should be added in such a verification study.

The model is applicable to rocket data if it uses a spherical probe. However, a verification based on rocket data may not be possible. For Langmuir probes the currents are calculated using the OML theory, which assumes unmagnetized conditions. This data will contain errors we can not control in the cases of interest. A successful verification therefore needs to use probes based on other theories than OML, where magnetic effects do not make an impact, still being as accurate as OML-based probes.

In the lower E-region, where Debye lengths are short, it is common to use needle-type Langmuir probes that follow cylindrical OML theory. Therefore a model including the cylindrical case is sought after. In the case of a cylindrical probe, there is an additional parameter: probe length. In this case, the angle of the magnetic field is also important, and the number of simulated data points explodes to a non-feasible amount. To build a model for a cylindrical probe, we would therefore need to make some assumptions, such as; the probe potential has a weak impact and can be neglected. We could also consider infinitely long probes, and simulate "long enough" probes, such that probe length can be neglected. Any such assumption will be non-trivial. However, the model would nevertheless be closer to reality than simply assuming unmagnetized conditions.

VI. CONCLUSION

The model, equation 18 is applicable to any experimental data that falls within the dimensionless parameter range and is not dominated by collisions. A real-world verification of this model would be beneficial; however, this is a challenging task. Such an experiment would need a varying magnetic field, in addition to good control over the parameters such as the plasma temperature, density, and magnetic field strength. The main problem is the scales involved. The De-

bye length needs to be larger than the probe, which also needs to be large enough to be considered spherical. In addition, the plasma needs to reach hundreds of Debye lengths along the magnetic field, requiring the use of large and sophisticated plasma chambers. This would be a highly interesting study to perform; however, it is left as future work.

The inclusion of a magnetic field greatly modifies the current collection with respect to the unmagnetized OML currents. The modification depends not only on the inclusion of the density-depleted magnetic bottle but also on the change of the probe sheath. In the unmagnetized case, the sheath formation is due to particles getting accelerated towards the probe. These particle orbits are evenly distributed around the probe in every dimension leading to a spherically symmetric sheath. For the magnetized case, the orbits are nonsymmetric since particles need to orbit the probe and are also gyrating around the magnetic field lines. This leads to the characteristic donut-shaped sheath seen in figure 2. The asymmetric sheath is likely the reason why no theory has accurately predicted the current collection for magnetized Langmuir probes. In the absence of a sheath, the current will be determined by the amount of particles flowing along the magnetic field lines that intersect the probe surface. However, when including the donut-shaped sheath, some particles will enter the sheath, and some of them will get collected due to scattering close to the probe. The asymmetry in the problem makes it a non-trivial task to calculate the current. However, it should be noted that the impact of the magnetic field on the currents to the probe is large, and should not be neglected. Therefore empirical models should see widespread usage.

As far as we know, none of the previous theories for spherical Langmuir probes in magnetized plasma¹⁷⁻²⁰ have been verified in a satisfying manner. Thus, the fact that we do not have a complete verification for our model at present is not unique to this work. However, we believe our model will fit better to good experimental data since the difference between all of those, and our model is that we do not make any non-trivial assumptions, as long as we trust the simulations to be a good representation of reality.

ACKNOWLEDGMENTS

This work received funding from the European Research Council (ERC) under the European Union's Horizon 2020 research and innovation programme (Grant Agreement No. 866357, POLAR-4DSpace).

This research is a part of the 4DSpace Strategic Research Initiative at the University of Oslo. This study is supported in part by the Research Council of Norway Grant 275653.

The present study is supported in part by the Japan Society for the Promotion of Science: JSPS (Grant No. 20K04041), and the innovative High-Performance Computing Infrastructure: HPCI (Project No. HP210159) in Japan.

The simulations were performed on resources provided by Sigma2 - the National Infrastructure for High Performance Computing and Data Storage in Norway, project number NN9987K

DATA AVAILABILITY STATEMENT

The simulation data that support the findings of this study are openly available in Zenodo at <http://dx.doi.org/10.5281/zenodo.8370038>.

All simulations can be reproduced using PINC 0.2.0 available at <https://github.com/pincproject>.

- ¹A. I. Eriksson, R. Boström, R. Gill, L. Åhlén, S.-E. Jansson, J.-E. Wahlund, M. André, A. Mälkki, J. A. Holtet, B. Lybekk, A. Pedersen, L. G. Blomberg, and The LAP Team, en"RPC-LAP: The Rosetta Langmuir Probe Instrument," *Space Science Reviews* **128**, 729–744 (2007).
- ²S. C. Buchert, A. Eriksson, R. Gill, T. Nilsson, L. Åhlen, J.-E. Wahlund, D. Knudsen, J. Burchill, W. Archer, A. Kouznetsov, N. Stricker, A. Bouridah, R. Bock, I. Hægström, M. Rietveld, S. Gonzalez, and N. Aponte, "First results from the Langmuir Probes on the Swarm satellites," in *2014 XXXIth URSI General Assembly and Scientific Symposium (URSI GASS)* (2014) pp. 1–1.
- ³H. Hoang, L. B. N. Clausen, K. Røed, T. A. Bekkeng, E. Trondsen, B. Lybekk, H. Strøm, D. M. Bang-Hauge, A. Pedersen, A. Spicher, and J. I. Moen, en"The Multi-Needle Langmuir Probe System on Board NorSat-1," *Space Science Reviews* **214**, 75 (2018).
- ⁴W. Zhao, Y. Wang, Y. Jin, L. Zhao, H. Zhou, L. Nie, G. Zhong, C. Liu, C. Watts, and J. P. Gunn, "Preliminary Design of ITER Divertor Langmuir Probe System," *Fusion Science and Technology* **76**, 79–87 (2020), publisher: Taylor & Francis _eprint: <https://doi.org/10.1080/15361055.2019.1674123>.
- ⁵H. M. Mott-Smith and I. Langmuir, "The Theory of Collectors in Gaseous Discharges," *Physical Review* **28**, 727–763 (1926), publisher: American Physical Society.
- ⁶J. G. Laframboise, *Theory of spherical and cylindrical langmuir probes in a collisionless, maxwellian plasma at rest*, PhD thesis, University of Toronto (1966).
- ⁷M. Lampe, en"Limits of validity for orbital-motion-limited theory for a small floating collector," *Journal of Plasma Physics* **65**, 171–180 (2001), publisher: Cambridge University Press.
- ⁸F. F. Chen, en"Langmuir probes in RF plasma: surprising validity of OML theory," *Plasma Sources Science and Technology* **18**, 035012 (2009).
- ⁹Z. Zakrzewski and T. Kopiczynski, "Effect of collisions on positive ion collection by a cylindrical Langmuir probe," *Plasma Physics* **16**, 1195–1198 (1974).
- ¹⁰S. M. Brask, S. Marholm, F. Di Mare, S. Adhikari, A. Spicher, T. Takahashi, and W. J. Miloch, "Electron–neutral collisions effects on Langmuir probe in the lower E-region ionosphere," *Physics of Plasmas* **29**, 033511 (2022).
- ¹¹I. Fratter, J.-M. Léger, F. Bertrand, T. Jager, G. Hulot, L. Brocco, and P. Vigneron, "Swarm Absolute Scalar Magnetometers first in-orbit results," *Acta Astronautica* **121**, 76–87 (2016).
- ¹²L. G. Blomberg, H. Matsumoto, J. L. Bougeret, H. Kojima, S. Yagitani, J. A. Cumnock, A. I. Eriksson, G. T. Marklund, J. E. Wahlund, L. Bylander, L. Åhlén, J. A. Holtet, K. Ishisaka, E. Kallio, Y. Kasaba, A. Matsuoka, M. Moncuquet, K. Mursula, Y. Omura, and J. G. Trotignon, "MEFISTO – An electric field instrument for BepiColombo/MMO," *Advances in Space Research Mercury, Mars and Saturn*, **38**, 672–679 (2006).
- ¹³M. K. Wahlström, E. Johansson, E. Veszelei, P. Bennich, M. Olsson, and S. Hogmark, "Improved Langmuir probe surface coatings for the Cassini satellite," *Thin Solid Films* **220**, 315–320 (1992).
- ¹⁴M. Sampl, W. Macher, T. Oswald, D. Plettemeier, H. O. Rucker, and W. S. Kurth, en"Juno Waves High Frequency Antenna Properties," *Radio Science* **56**, e2020RS007184 (2021), _eprint: <https://onlinelibrary.wiley.com/doi/pdf/10.1029/2020RS007184>.
- ¹⁵M. Ossowski, M. Borys, P. Palma, L. Wisniewski, M. Tokarz, T. Kuciński, E. Ryszawa, K. Bochar, M. Duda, and J. Grygorczuk, *DEVELOPMENT OF DEPLOYABLE RWI AND LP-PWI MECHANISMS FOR JUICE MISSION - QUALITY AND PRODUCT ASSURANCE ASPECTS* (2021).
- ¹⁶J. G. Laframboise and L. J. Sonmor, en"Current collection by probes and electrodes in space magnetoplasmas: A review," *Journal of Geophysical Research: Space Physics* **98**, 337–357 (1993), _eprint: <https://agupubs.onlinelibrary.wiley.com/doi/pdf/10.1029/92JA00839>.
- ¹⁷L. Sonmor and J. Laframboise, "Exact current to a spherical electrode in a collisionless, large-Debye-length magnetoplasma," *Physics of Fluids B; (United States)* **3-9** (1991), 10.1063/1.859619.
- ¹⁸L. W. Parker and B. L. Murphy, en"Potential buildup on an electron-emitting ionospheric satellite," *Journal of Geophysical Research* (1896-1977) **72**, 1631–1636 (1967), _eprint: <https://agupubs.onlinelibrary.wiley.com/doi/pdf/10.1029/JZ072i005p01631>.
- ¹⁹J. Rubinstein and J. G. Laframboise, "Theory of a spherical probe in a collisionless magnetoplasma," *The Physics of Fluids* **25**, 1174–1182 (1982).
- ²⁰J. Rubinstein and J. G. Laframboise, "Theory of axially symmetric probes in a collisionless magnetoplasma: Aligned spheroids, finite cylinders, and disks," *The Physics of Fluids* **26**, 3624–3627 (1983).
- ²¹J.-L. Jauberteau, I. Jauberteau, O. D. Cortázar, and A. M. Megia-Macias, "Langmuir probe in magnetized plasma: Determination of the electron diffusion parameter and of the electron energy distribution function," *Contributions to Plasma Physics* **60** (2019), 10.1002/ctpp.201900067, publisher: Wiley-VCH Verlag.
- ²²A. Piel, F. Greiner, H. Jung, and W. J. Miloch, "Molecular dynamics simulations of wake structures behind a microparticle in a magnetized ion flow. I. Collisionless limit with cold ion beam," *Physics of Plasmas* **25**, 083702 (2018).
- ²³W. J. Miloch, H. Jung, D. Darian, F. Greiner, M. Mortensen, and A. Piel, en"Dynamic ion shadows behind finite-sized objects in collisionless magnetized plasma flows," *New Journal of Physics* **20**, 073027 (2018), publisher: IOP Publishing.
- ²⁴E. Buckingham, "On Physically Similar Systems; Illustrations of the Use of Dimensional Equations," *Physical Review* **4**, 345–376 (1914), publisher: American Physical Society.
- ²⁵C. K. Birdsall and A. B. Langdon, *Plasma physics via computer simulation* (McGraw-Hill, 1985).
- ²⁶R. W. Hockney and J. W. Eastwood, *Computer Simulation Using Particles* (CRC Press, 1988).
- ²⁷J. P. Verboncoeur, "Particle simulation of plasmas: review and advances," *Plasma Physics and Controlled Fusion* **47**, A231–A260 (2005).
- ²⁸G. Lapenta, "Particle simulations of space weather," *Journal of Computational Physics* **231**, 795–821 (2012).
- ²⁹J. Boris, R. Shanny, U. S. O. o. N. Research, and N. R. Laboratory, *Proceedings: Fourth Conference on Numerical Simulation of Plasmas, November 2, 3, 1970* (Naval Research Laboratory, 1972).
- ³⁰H. Qin, S. Zhang, J. Xiao, J. Liu, Y. Sun, and W. M. Tang, "Why is Boris algorithm so good?" *Physics of Plasmas* **20**, 084503 (2013).
- ³¹U. Trottenberg, C. W. Oosterlee, and A. Schuller, *Multigrid* (Academic Press, 2000).
- ³²G. V. Killie, *A Parallel Multigrid Poisson Solver for PINC, a new Particle-in-Cell Model*, Masters thesis, University of Oslo (2016).
- ³³S. Marholm, *The Unstructured Particle-In-Cell Method with Applications for Objects in Ionospheric Plasmas*, Doctoral thesis, University of Oslo (2020).
- ³⁴C. Birdsall, "Particle-in-cell charged-particle simulations, plus Monte Carlo collisions with neutral atoms, PIC-MCC," *Plasma Science, IEEE Transactions on* **19**, 65–85 (1991).
- ³⁵Y. Miyake and H. Usui, "New electromagnetic particle simulation code for the analysis of spacecraft-plasma interactions," *Physics of Plasmas* **16**, 062904 (2009).
- ³⁶V. Vahedi and M. Surendra, "A Monte Carlo collision model for the particle-in-cell method: applications to argon and oxygen discharges," *Computer Physics Communications Particle Simulation Methods*, **87**, 179–198 (1995).
- ³⁷S. Marholm and R. Marchand, "Finite-length effects on cylindrical Langmuir probes," *Physical Review Research* **2**, 023016 (2020), publisher: American Physical Society.
- ³⁸M. J. Alport, J. A. Antoniadis, D. A. Boyd, R. G. Greaves, and R. F. Ellis, en"Electrical breakdown at low pressure in the presence of a weak magnetic field," *Journal of Geophysical Research: Space Physics* **95**, 6145–6153 (1990), _eprint: <https://onlinelibrary.wiley.com/doi/pdf/10.1029/JA095iA05p06145>.
- ³⁹S. Brask and W. J. Miloch, "Simulations of magnetized Spherical Langmuir probes," <https://zenodo.org/record/8370038> (2023).
- ⁴⁰R. Jones, "Neural Network Analysis of Langmuir Probe Data from a Magnetized Plasma," *Transactions of the Kansas Academy of Science* **104**, 31–

36 (2001), publisher: Kansas Academy of Science.

⁴¹A. Brekke and J. Moen, "Observations of high latitude ionospheric conductances," *Journal of Atmospheric and Terrestrial Physics* The XX IUGG

General Assembly, **55**, 1493–1512 (1993).